

Wasserstoff in nominell wasserfreien Mineralen

vorgelegt von

Diplom-Mineralogin Sylvia-Monique Thomas

aus Freiberg

von der Fakultät VI - Planen Bauen Umwelt
der Technischen Universität Berlin

zur Erlangung des akademischen Grades

Doktorin der Naturwissenschaften

– Dr. rer. nat. –

genehmigte Dissertation

Promotionsausschuss:

Vorsitzender: Prof. Dr. G. Franz

Berichterin: Prof. Dr. M. Koch-Müller

Berichter: Prof. Dr. W. Heinrich

Berichter: Prof. Dr. E. Libowitzky

Tag der wissenschaftlichen Aussprache: 28. 03. 2008

Berlin 2008

D 83

Inhaltsverzeichnis

| | |
|--|----|
| Zusammenfassung | 1 |
| Summary | 3 |
| | |
| Einführung | 5 |
| Referenzen..... | 16 |
| | |
| Kapitel 1 | 24 |
| "Protonation in germanium equivalents of ringwoodite, anhydrous phase B and superhydrous phase B" | 24 |
| Abstract..... | 25 |
| Introduction | 26 |
| Experimental Methods..... | 27 |
| Syntheses..... | 27 |
| Electron probe microanalysis | 28 |
| Transmission electron microscopy | 29 |
| X-ray diffraction..... | 29 |
| Raman spectroscopy | 30 |
| Infrared spectroscopy | 30 |
| Results | 32 |
| EPMA and TEM analyses | 32 |
| X-ray diffraction..... | 33 |
| Raman spectroscopy | 37 |
| Infrared spectroscopy | 39 |
| OH distribution and quantification | 43 |
| Discussion..... | 44 |
| Ringwoodite | 44 |
| Ge-anhydrous phase B | 48 |
| Ge-superhydrous phase B | 52 |
| Acknowledgements | 53 |
| References | 53 |
| Appendix | 58 |
| | |
| Kapitel 2 | 66 |
| "Application of Raman spectroscopy to quantify trace water concentrations in glasses and garnets" | 67 |
| Abstract..... | 67 |
| Introduction | 68 |

| | |
|--|-----------|
| Analytical Techniques | 69 |
| Samples | 69 |
| Raman spectroscopy | 69 |
| Proton-Proton-scattering | 71 |
| IR spectroscopy | 73 |
| Results | 74 |
| Raman spectroscopy | 74 |
| Raman spectroscopy vs. Independent quantification methods | 81 |
| Discussion | 85 |
| Acknowledgements | 87 |
| References | 87 |
| Kapitel 3 | 89 |
| "IR calibrations for water determination in olivine and SiO₂ polymorphs" | 90 |
| Abstract | 90 |
| Introduction | 91 |
| Experimental and Analytical techniques | 95 |
| Syntheses and Samples | 95 |
| Transmission electron microscopy (TEM) | 96 |
| IR spectroscopy | 97 |
| Raman spectroscopy | 98 |
| Unoriented statistical measurements | 99 |
| Polarized measurements | 99 |
| Spectra treatment and quantification procedure | 100 |
| Proton-Proton-scattering | 101 |
| Secondary ion mass spectrometry | 102 |
| Results | 104 |
| Infrared spectroscopy | 105 |
| Raman spectroscopy | 110 |
| Water contents | 111 |
| Absorption coefficients | 115 |
| Discussion | 117 |
| Water contents | 117 |
| Absorption coefficients | 118 |
| Acknowledgements | 128 |
| References | 128 |
| Eidesstattliche Erklärung | 135 |
| Danksagung | 136 |

Zusammenfassung

Die vorgelegte Dissertation beschäftigt sich mit (1) der Verwendung von Germanaten als Hochdruckmodelle für den Wassereinbau in wasserhaltige und nominell wasserfreie Erdmantelminerale, (2) der Anwendbarkeit der konfokalen Ramanspektroskopie für den Nachweis von Wassergehalten im ppm-Bereich für amorphe Gläser sowie für isotrope Granate, und (3) mit der Entwicklung von mineralspezifischen Extinktionskoeffizienten für die Quantifizierung von Spurenwassergehalten in nominell wasserfreien Phasen mit Infrarot(IR)-Spektroskopie.

(1) Germanium-Äquivalente von Ringwoodit, Anhydrous Phase B und Superhydrous Phase B wurden bei 2 GPa und 950-1000°C unter Wasserüberschuss synthetisiert und mit verschiedenen spektroskopischen und analytischen Methoden charakterisiert. Die Ergebnisse verdeutlichen, dass wasserhaltige Germanate offenbar gute Hochdruckmodelle für Mantelsilikate sind, in denen der Wasserstoffeinbau von der Stöchiometrie gesteuert wird. Im Gegensatz dazu wird gezeigt, dass für nominell wasserfreie Phasen, Germanate, als Silikatäquivalente, für Studien zu Wassereinbau und zur Löslichkeit nur bedingt eingesetzt werden können. In den entsprechenden Germanatphasen unterscheidet sich der OH-Einbau qualitativ und quantitativ von dem der Hochdrucksilikate; die OH-Löslichkeit wird von anderen Faktoren, wie zum Beispiel der Wasserfugazität und intrinsischen Defekten, gelenkt.

(2) Eine Quantifizierungsroutine für die Bestimmung von Spurenwassergehalten in Festkörpern wird präsentiert, die die konfokale Ramanspektroskopie mit der sogenannten „Komparator-Technik“ verknüpft. Eine Serie von Gläsern und Granate mit unterschiedlichen chemischen Zusammensetzungen wurden ramanspektroskopisch untersucht. Die Wassergehalte der Proben wurden des Weiteren unabhängig mit Proton-Proton-Streuung und IR-Spektroskopie bestimmt. Die Anwendbarkeit der „Komparator-Technik“ für die

Quantifizierung von Wassergehalten von 40 Gew.-ppm bis zu 40 Gew.-%, sowohl in natürlichen und synthetischen Gläsern, als auch in Granatproben, konnte nachgewiesen werden. Des Weiteren wurde ein materialspezifischer Extinktionskoeffizient für Quarzglas bestimmt, $\epsilon_{\text{itot}} = 72000 \pm 12000 \text{ l mol}^{-1}_{\text{H}_2\text{O}} \text{ cm}^{-2}$, der zur Quantifizierung von Wassergehalten mit IR-Spektroskopie benutzt werden kann.

(3) Es ist bekannt, dass allgemein gültige IR-Kalibrierungen für die quantitative Bestimmung von Wassergehalten in Festkörpern nicht für nominell wasserfreie Minerale verwendbar sind und mineralspezifische Extinktionskoeffizienten benötigt werden (Rossman 2006). In dieser Arbeit wurden Olivin und SiO_2 -Polymorphe mit isoliert eingebauten OH-Punktdefekten synthetisiert, z. B. Quarz, Coesit und Stishovit mit $\text{B}^{3+} + \text{H}^+ = \text{Si}^{4+}$ und/oder $\text{Al}^{3+} + \text{H}^+ = \text{Si}^{4+}$ Substitutionen. Die Wassergehalte der Syntheseprodukte sowie natürlicher Proben wurden unter Anwendung von Proton-Proton Streuung, konfokaler Ramanspektroskopie und Sekundärionenmassenspektrometrie bestimmt und zur Berechnung neuer mineralspezifischer Extinktionskoeffizienten für die IR-Spektroskopie genutzt. Die Abhängigkeit des Extinktionskoeffizienten von spezifischen OH-Defekten wurde untersucht. Unsere Ergebnisse bestätigen, dass es unerlässlich ist, mineralspezifische Kalibrierungen für die Wasserbestimmung in nominell wasserfreien Mineralen zu benutzen. Nur so können absolute Wasserlöslichkeiten bestimmt werden, die für eine Modellierung eines inneren Erdwasserkreislaufs benötigt werden. Des Weiteren wird eine Quantifizierungsroutine präsentiert, die die Anwendbarkeit konfokaler Ramanspektroskopie für die Bestimmung von Spurenwassergehalten in anisotropen nominell wasserfreien Mineralen bestätigt.

Summary

This PhD thesis is focused on (1) the utility of germanate analogues as high-pressure models of hydrous and nominally anhydrous mantle silicates, (2) the demonstration of the feasibility of confocal Raman spectroscopy for the determination of very low (ppm-level) water concentrations in glasses and garnets, and (3) with the establishment of mineral-specific absorption coefficients for a routine quantification of trace water contents in nominally anhydrous minerals with infrared(IR) spectroscopy.

(1) Ge-analogue material of ringwoodite, anhydrous phase B and superhydrous phase B was synthesized at 2 GPa and 950-1000°C with water in excess. The run products were characterized utilizing a variety of analytical and spectroscopic techniques. Our results show, that germanates are indeed good low-pressure analogues for hydrous mantle silicates in which protonation is controlled by stoichiometry. In contrast, we demonstrate that it is not to be recommended to use germanates as high-pressure models for nominally anhydrous minerals in water-related studies. In these Ge-bearing phases, which are usually synthesized at much lower pressures, i.e. lower water fugacities, OH incorporation differs from the high-pressure silicon equivalents qualitatively and quantitatively, as hydroxyl solubility is governed by other factors like the water fugacity and intrinsic defects.

(2) We present a technique for the quantification of water in glasses down to the ppm level, combining confocal microRaman spectroscopy with the recently developed “Comparator Technique”. To test this method we used a suite of glasses and gemstone-quality garnets with varying chemical compositions. Water contents were independently determined with proton-proton (pp) scattering and IR spectroscopy. In this work we demonstrate the usefulness of Raman spectroscopy for quantifying water concentrations in natural and synthetic glasses and garnets, and verify its adaptability for concentrations from 40 wt ppm

up to 40 wt % H₂O. Furthermore, we propose an integrated molar absorption coefficient for water in quartz glass, $\epsilon_{\text{itot}} = 72000 \pm 12000 \text{ l mol}_{\text{H}_2\text{O}}^{-1} \text{ cm}^{-2}$, for quantitative IR spectroscopy.

(3) It has been observed that frequently used calibrations for quantitative water analyses in solids cannot be adopted to nominally anhydrous minerals (Rossman 2006). In this work we synthesized olivine and SiO₂ polymorphs with specific isolated hydroxyl point defects, e.g., quartz, coesite and stishovite with B³⁺ + H⁺ = Si⁴⁺ and/or Al³⁺ + H⁺ = Si⁴⁺ substitutions. We quantified sample water contents of both natural samples and our run products by applying pp-scattering, confocal microRaman spectroscopy and secondary ion mass spectrometry. Water concentrations were used to calculate new mineral-specific absorption coefficients. The dependency of the absorption coefficients obtained on specific OH point defects is discussed in this study. Our results confirm that not using mineral-specific calibrations for the water determination in nominally anhydrous minerals leads to misinterpretation of sample water concentrations, that are required for modelling the earth's deep water cycle. Moreover, we present a routine to detect OH traces in anisotropic minerals using Raman spectroscopy combined with the "Comparator Technique".

Einführung

Wasserstoff ist das häufigste Element unseres Solarsystems und bildet gebunden an Sauerstoffatome H_2O -Moleküle, OH^- -Gruppen und seltener H_3O^+ , H_3O_2^- , H_5O_2^+ oder NH_4^+ -Verbindungen (Hawthorne 1992; Prewitt & Parise 2000; Libowitzky & Beran 2006). Minerale können Wasser in verschiedenen Formen enthalten. Mehrere Gew.-% Wasser können stöchiometrisch im Kristallgitter gebunden sein, als H_2O -Moleküle, wie z. B. im Gips, $\text{CaSO}_4 \times 2 \text{H}_2\text{O}$, oder als Hydroxylgruppe (OH^-), z. B. im Malachit $\text{Cu}_2[(\text{OH})_2/\text{CO}_3]$ oder Kaolinit $\text{Al}_4[(\text{OH})_8/\text{SiO}_4\text{O}_{10}]$. Bedeutende Konzentrationen können aber auch in nichtstöchiometrischen Verhältnissen in Hohlräumen oder auf Zwischengitterplätzen einiger wirtschaftlich relevanter Phasen vorhanden sein, wie z. B. in Zeolithen. Wasser kann, neben den genannten Mechanismen, in Form von Flüssigkeitseinschlüssen, als Adsorptionswasser oder in Versetzungsstrukturen an Minerale gebunden werden, wie es z. B. für Quarz bekannt ist (Kronenberg 1994). Spurenwassergehalte können aber ebenfalls als Hydroxyl-Punktdefekt¹ in **nominell wasserfreien Mineralen** gespeichert werden, die laut ihrer Formel kein Wasser enthalten. Während die Stabilitätsbereiche der Mehrheit nominell wasserhaltiger Minerale auf die Erdkruste und den oberen Erdmantel beschränkt sind, sind nominell wasserfreie Minerale auch darüber hinaus in der Übergangszone und im unteren Erdmantel stabil. Die experimentelle Untersuchung dieser Phasen ist daher eine wichtige Grundlage für das Verständnis der Wasserspeicherkapazität des Erdmantels. Pionierstudien von Kats & Haven (1960), Brunner et al. (1961) und Kats (1962) berichteten von bedeutenden OH^- -Defektkonzentrationen in synthetischem Quarz. Heute ist bekannt, dass auch natürlicher Quarz typischerweise bis zu 40 Gew.-ppm H_2O in Form von OH^- -Defekten einbaut und bis zu 8000 Gew.-ppm H_2O in Form von Flüssigkeitseinschlüssen enthalten kann (Kronenberg & Wolf 1990). In den letzten Jahrzehnten konnten durch zahlreichen Studien signifikante Wasserstoffgehalte (von einigen Gew.-ppm bis zu mehreren Gew.-%) in nahezu allen wichtigen nominell wasserfreien Mineralen der Erdkruste (z. B. Feldspat, Granat) und des Erdmantels (z. B. Olivin, Pyroxen, Wadsleyit, Ringwoodit) nachgewiesen werden (z. B. Aines

¹ Im Bezug auf Hydroxyl-Punktdefekte in nominell wasserfreien Mineralen werden im Folgenden häufig der allgemeine Terminus „Wasser“ oder Gew.-% bzw. Gew.-ppm H_2O verwendet.

& Rossman 1984; Skogby et al. 1990; Johnson & Rossman 2004; Smyth et al. 2003; Jacobsen et al. 2005; Koch-Müller et al. 2006). So enthalten wichtigen Mantelminerale wie Olivin bis zu 400 Gew.-ppm H_2O (Beran & Libowitzky 2006), Granate können bis zu 2200 Gew.-ppm H_2O einbauen und an Pyroxenen wurden bis zu 600 Gew.-ppm H_2O nachgewiesen (Johnson 2006), um nur einige Beispiele für Studien natürlicher Proben zu nennen. In experimentellen Untersuchungen zur Löslichkeit von Wasser in Mineralen in Abhängigkeit von Druck, Temperatur und der Zusammensetzung wurden im Allgemeinen höhere Konzentrationen für den Grossteil der wichtigen Erdmantelminerale bestimmt. Es wurde z. B. nachgewiesen, dass synthetischer Olivin bis zu 0.9 Gew.-% H_2O und Wadsleyit und Ringwoodit bis zu 3.1 Gew.-% H_2O speichern können (z. B. Inoue et al. 1995; Kohlstedt et al. 1996; Smyth et al. 2006). Experimentelle Studien der Hochdruckforschung implizieren somit, dass nominell wasserfreie Minerale ein Vielfaches des Wassergehalts der Hydrosphäre speichern könnten. Es wird postuliert, dass Minerale des Erdmantels das grösste Wasserreservoir der Erde beinhalten könnten (Ringwood 1966; Martin & Donnay 1972; Smyth 1987, 2006; Bell & Rossman 1992; Beran 1999; Ohtani 2005). Im Allgemeinen geht man davon aus, dass Wasser über wasserhaltige Minerale in Subduktionszonen ins Erdinnere geführt, von nominell wasserfreien Mineralen absorbiert und transportiert wird, um schliesslich über frische ozeanische Kruste wieder freigesetzt zu werden (Ito et al. 1983; Lu & Keppler 1997; Rüpke et al. 2004; Smyth 2006). Ferner wird auch der Beitrag von advektivem Fluss im Mantelkeil zum Recycling des Wassers diskutiert (Keppler & Bolfan-Casanova 2006; Frost 2006).

Eine Diskussion über die Rolle nominell wasserfreier Minerale für die Aufrechterhaltung des Wasserkreislauf der Erde setzt die Kenntnis ihrer grundlegenden strukturellen **Hydratationsmechanismen** voraus, welche im Folgenden kurz erläutert werden sollen. In nominell wasserfreie Minerale wird Wasserstoff hauptsächlich in Form von OH-Punktdefekten eingebaut. Eine Möglichkeit des Wassereinbaus sind Leerstellen im Kristallgitter: die Vakanz der Kationenposition wird durch die zusätzliche positive Ladung des Wasserstoffatoms kompensiert. Dabei ist die verbreitetste Art die Hydrogranatsubstitution

$\text{Si}^{4+} + 4\text{O}^{2-} = {}^{(4)}[\] + 4\text{OH}^-$, bei der es sich um 4 ladungskompensierende Protonen gekoppelt an die Sauerstoffatome einer Si^{4+} -Leerstelle handelt. Diese Art der Substitution, die auch als Cluster einzelner OH-Defekte betrachtet werden kann, ist für eine Vielzahl von Mineralen bekannt, so z. B. für Granat (*Lager et al. 1989; Rossman & Aines 1991; Wright et al. 1994; Lager et al. 2005*), Coesit (*Koch-Müller et al. 2001*), Olivin (*Libowitzky & Beran 1995*), Perowskit (*Beran et al. 1996*) oder auch Ringwoodit (z. B. *Blanchard et al. 2005a, b*). Weiterhin kann der strukturelle Einbau von OH-Defekten über gekoppelte Substitutionen erfolgen, wie z. B. der Reduktion von dreiwertigem Eisen zu zweiwertigem Eisen (z. B. *Kudoh et al. 1996*), wobei der Einbau des Wasserstoffs durch die reduzierte Ladung des Eisens ausgeglichen wird. Eine andere weitverbreitete Art der Hydratation ist der Ersatz von Kationen auf Tetraeder- oder Oktaederplätzen, wie z. B. die Substitution von Si^{4+} durch Al^{3+} oder B^{3+} und der damit verbundenene Ladungsausgleich durch H^+ (z. B. *Kats 1962; Smyth et al. 1995*).

Durch den Wassereinbau werden die Mineralstrukturen modifiziert, es entstehen Defektstrukturen, die **Änderungen der Mineraleigenschaften** zur Folge haben. Schon die Anwesenheit von Spurenwassergehalten in Erdmantelmineralen führt zu Änderungen ihrer chemischen und physikalischen Eigenschaften und hat somit einen grossen Einfluss auf die Rheologie, die Seismik sowie die Phasengleichgewichte und das Schmelzverhalten. Es ist weithin anerkannt, dass die Anwesenheit von Wasser Rheologie und Schmelzverhalten von Festkörpern beeinflusst und somit magmatische Prozesse (*Hirth & Kohlstedt 1996*) kontrolliert. So ist das sogenannte „hydrolytic weakening“ erstmals in den 60iger Jahren an Quarz beobachtet worden (z. B. *Griggs 1967; Kekulawala et al. 1981; Kronenberg et al. 1986; Kronenberg & Wolf 1990*). Später wurde dieses Phänomen auch an weiteren Mineralphasen des Erdmantels nachgewiesen (z. B. *Dimanov et al. 1999, 2003; Rybacki & Dresen 2000, 2004; Hirth & Kohlstedt 2003; Hier-Majumder et al. 2005*) und wird unter anderem als Ursache für Erdbeben diskutiert (z. B. *Dobson et al. 2002*). Verschiedene Studien zeigen, dass Wasser Schmelztemperaturen reduziert und die Magmenbildung initiiert (*Hirth & Kohlstedt 1996; Asimow et al. 2004; Hirschmann 2006*). Spurengehalte von

Wasserstoff haben enorme Auswirkungen auf einige physikalische Mineraleigenschaften wie das Deformationsverhalten (*Kavner 2003; Kohlstedt 2006*), Viskosität (*Karato et al. 1986*), Wärme- sowie elektrische Leitfähigkeit (*Mackwell et al. 1985; Karato 1990; Huang et al. 2005; Wang et al. 2006*). Solch geringe Konzentrationen beeinflussen weiterhin das Diffusionsverhalten (*Kohlstedt & Mackwell 1998; Demouchy 2004; Kurka 2005; Lathe et al. 2005; Ingrin & Blanchard 2006; Peslier & Luhr 2006*) und Phasentransformationen (*Wood 1995; Kohlstedt & Mackwell 1998; Smyth and Frost 2002*) und können sowohl Strahlungsschäden als auch den metamikten Zustand einiger Minerale (*Hawthorne et al. 1991; Aines & Rossman 1986*) stabilisieren. Wasser in Mineralen verändert Kompressibilitäten (*Smyth et al. 2003; 2004*), Laufzeitgeschwindigkeiten seismischer Wellen und die elastischen Konstanten von Mineralen (z. B. *Jacobsen et al. 2005, 2006*). Jacobsen et al. (2004) zeigen beispielsweise, dass ein Wassergehalt von ca. 1 Gew.-% in Ringwoodit denselben Effekt auf die P- und S-Wellengeschwindigkeiten hat, wie eine Temperaturerhöhung um 600 bis 1000 °C, das heisst, mit einer erheblichen Reduktion der Wellengeschwindigkeiten verbunden ist. Der Wassereinbau in Minerale hat also einen grösseren Effekt auf seismische Wellengeschwindigkeiten als bisher angenommen und die Auswertung tomographischer Bilder der Übergangszone muss überdacht werden.

Weitere Studien beschäftigen sich mit der Speicherkapazität des Erdmantels (*Bolfan-Casanova et al. 2000; Huang et al. 2005; Hirschmann et al. 2005; Hirschmann 2006*) und mit dem Ursprung des Wassers auf der Erde. Diskutiert wird beispielsweise, ob die an natürlichen Mantelmineralen bestimmten Wassergehalte über geologische Zeiträume konstant waren und damit Aufschluss über anfängliche Bedingungen geben oder, ob sie durch Transport an die Erdoberfläche verändert wurden (z. B. *Thompson 1992; Ingrin & Skogby 2000; Peslier & Luhr 2006; Jacobsen & van der Lee 2006*). Auf diese Weise wird versucht, Fragen zur chemischen Evolution und zu inneren Prozessen der Erdentwicklung zu beantworten.

Für das Verständnis der Änderungen von Mineraleigenschaften und ihrer Auswirkungen auf Mantelprozesse ist es erforderlich, deren Abhängigkeiten von variierenden Wassergehalten

zu erforschen. Die zentralen Fragen dabei lauten: „Wieviel Wasser kann in solchen Mineralen gespeichert werden?“, „Welche Parameter kontrollieren die H-Konzentration?“ und „Welche Hydratations- und Dehydrationsmechanismen sind verantwortlich?“.

Als geeignete Methode zur Wasserstoffbestimmung im Spurenbereich hat sich die **IR-Spektroskopie** bewährt. Bei dieser Methode wird elektromagnetische Strahlung im IR-Bereich auf eine Probe gestrahlt und regt Molekülschwingungen an, indem ein Teil des eingestrahlten Lichts von den Probemolekülen absorbiert wird. Diese Schwingungen verursachen charakteristische Absorptionsbanden im IR-Spektrum. Die IR-Spektroskopie ermöglicht die Charakterisierung der H-Brückenbindungen, der räumlichen Orientierung der OH-Vektoren, eine Lokalisierung des Protons sowie eine Konzentrationsbestimmung. Die Konzentration der jeweiligen Spezies, kann unter Benutzung des Lambert-Beer'schen Gesetzes bestimmt werden ($A = c \times d \times \epsilon$), welches besagt, dass die gemessene Absorption (A) einer Spezies direkt proportional zur Konzentration dieser Spezies (c) und der Dicke der Probe (d) ist. Der Proportionalitätsfaktor wird Extinktionskoeffizient (ϵ) genannt. Zur Quantifizierung ist daher eine Kalibrierung erforderlich. Seit einigen Jahren werden zur Wasserbestimmung in Mineralen Kalibrierungen verwendet (*Paterson 1982; Libowitzky & Rossman 1997*), die hauptsächlich an wasserführenden Mineralen und Gläsern erstellt wurden. Studien an nominell wasserfreien Mineralen sprechen jedoch gegen eine Anwendbarkeit dieser bestehenden Kalibrierungen für derartige Minerale, die Wasser nur in Spuren enthalten. Die ermittelten Werte weichen teilweise bis zu einem Faktor von 4 von den Kalibrierkurven ab (*Koch-Müller et al. 2001; Pawley et al. 1993*). Die Ermittlung der absoluten Wassergehalte erfordert folglich für jedes nominell wasserfreie Mineral eine eigene mineralspezifische Kalibrierung, die mit Hilfe einer unabhängigen Absolutmethode erstellt werden kann. Solche mineralspezifischen Kalibrierungen wurden in den letzten Jahren für ausgewählte Mineralgruppen entwickelt. Für die IR-Spektroskopie benötigte Extinktionskoeffizienten wurden so z. B. für Quarz (z. B. *Brunner et al. 1961; Kats 1962; Chakaborty & Lehmann 1976, Paterson 1982*), Coesit (*Koch-Müller et al. 2001*), Pyroxen (*Bell et al. 1995*), Olivin (*Bell et al. 2003*), Feldspat (*Johnson and Rossman 2003*), Granat

(Maldener et al. 2001; Rossman 1988; Rossman and Aines 1991) und Stishovit (Pawley et al. 1993) bestimmt. Als Quantifizierungsmethoden zur Bestimmung unabhängiger Daten für nominell wasserfreie Minerale dienten in der Vergangenheit z. B. **Wasserstoffmanometrie** (Bell et al. 1995), **Kernreaktionsanalyse** (Bell et al. 2003, 2004; Hammer et al. 1996; Maldener et al. 2001; Rossman et al. 1988) und **¹H-Kernresonanz** (Keppler and Rauch 2000, Cho and Rossman 1993, Johnson and Rossman 2003; Kohn 1996), wobei alle genannten Techniken durch, mehr oder minder grosse, Probleme infolge spezieller Anforderungen an Probenpräparation und –quantität geprägt sind. Die **Wasserstoffmanometrie** ist eine Extraktionsmethode bei der das Probenwasser durch Erhitzen unter Vakuum ausgetrieben und zu Wasserstoff reduziert wird, welcher dann in einer Kalbrierkammer quantifiziert wird. Der Nachteil dieser Methode ist, dass bei geringen Wasserkonzentrationen im Zehner-Gew.-ppm-Bereich mehrere Gramm an homogenem Probenmaterial benötigt werden. Die **Kernreaktionsanalyse** basiert auf charakteristischen Kernreaktionen des einfallenden Ions mit den Ionen der Probe. Für die Wasserstoffanalyse wurde in der Vergangenheit die ¹⁵N-Methode am häufigsten verwendet. Bei dieser Methode wird eine Wechselwirkung von ¹⁵N Ionen und den Wasserstoffionen der Probe induziert. Es entsteht ein ¹⁶O-Kern, der durch α -Zerfall in den angeregten Endkern ¹²C zerfällt, welcher wiederum beim Übergang in den Grundzustand γ -Strahlung aussendet, die direkt proportional zur absoluten Wasserstoffkonzentration der Probe ist. Die **¹H-Kernresonanzspektrometrie** beruht auf der Wechselwirkung der magnetischen Momente der Atomkerne mit elektromagnetischer Strahlung. Die rotierende elektrische Ladung des H-Atomkerns erzeugt ein schwaches Magnetfeld. Die Kernpolarisation des positiv geladenen Atomkerns des Wasserstoffatoms wird durch die Einstrahlung eines äusseren Magnetfeldes verändert, das schwache Magnetfeld des Kerns richtet sich parallel oder senkrecht zum äusseren Magnetfeld aus. Entspricht die Energieänderung zwischen beiden Zuständen der Senderfrequenz einer Hochfrequenzspule, tritt Resonanzabsorption auf. Die Resonanzfrequenz hat für ein gegebenes Magnetfeld für jeden Kern in einer bestimmten chemischen Umgebung einen charakteristischen Wert. Für die Wasserstoffanalyse wird

zumeist das sogenannte „magic-angle-spinning“ eingesetzt, bei dem der Probenhalter um seine eigene Achse in einem Winkel von $54^{\circ}44'$ zum externen statischen Magnetfeld schnell rotiert wird, um ein hochaufgelöstes Probenspektrum zu erzeugen. Ein Vorteil ist die mögliche Separierung verschiedener Spezies und die Charakterisierung ihrer direkten chemischen Umgebung. Nachteile dieser Methode sind jedoch die benötigte Probenmenge (mg - g) und die Verwendung von Pulverproben. So wird diskutiert, ob polykristallines Material repräsentative Ergebnisse für äquivalente Einkristalle liefert oder, ob die nachgewiesenen Wassergehalte möglicherweise durch Wasser an Korngrenzen oder submikroskopische Einschlüsse in grossem Masse verfälscht werden (z. B. Keppler & Rauch 2000). Ferner ist die Anwendung auf Minerale mit möglichst geringen Gehalten an paramagnetischen Ionen beschränkt. Analytische Herausforderungen im Bezug auf den Nachweis von Spurenwasserstoffgehalten in geologischem Material bieten auch weitere Methoden, wie die **Sekundärionenmassenspektrometrie** (z. B. Rhede and Wiedenbeck 2006). Bei letzterer Technik wird ein Strahl beschleunigter Primärionen (meist O^+ , Cs^+) auf die zu untersuchende Probe fokussiert und trägt diese sukzessive ab, indem die Primärionen Sekundärionen aus der Probe herausschiessen, welche massenspektrometrisch analysiert werden. Zur Quantifizierung werden geeignete Eichproben mit definierten Wassergehalten benötigt. Grundlegende Vorteile, wie die Insensitivität gegenüber der Probenorientierung und eine hervorragende lokale Auflösung (Yurimoto et al. 1989; Kurosawa et al. 1992; Deloule et al. 1995; Koga et al. 2003; Hauri et al. 2002; Aubaud et al. 2007) werden durch Faktoren, wie z. B. den Einfluss der Matrixzusammensetzung (Hervig 1987; Koga et al. 2003, Aubaud et al. 2007), dem „Channeling“-Effekt, einer hohen Vakuumqualität zur Bewältigung störender Wasserstoffsignale im Untergrund, einer Mindestgrösse der Proben, einer zeitaufwendigen Präparation und der lokalen Zerstörung der Proben, in den Schatten gestellt. Andere Techniken, wie **elastische Rückstreudektektionsanalyse** (Sweeney et al. 1997) und **Proton-Proton-Streuung** (Wegden et al. 2005; Reichart et al. 2004) befinden sich in Entwicklung. Die **elastische Rückstreudektektionsanalyse** basiert auf der Rutherford-Streuung. Ein hochenergetischer $^4He^+$ -Ionenstrahl wird auf die Probe fokussiert und führt zur

Streuung der Protonen. Das rückgestreute Probenatom wird an einem Siliziumdetektor direkt nachgewiesen. Zusätzlich erhält man Tiefeninformationen durch Energieverluste, die die gestreuten Probenatome auf dem Weg durch die Probe erfahren. Bei der Verwendung von Projektil-Ionen wie Helium limitiert jedoch die Strahlenschädigung die Nachweisgrenze auf einige hundert Gew.-ppm H und die Tiefeninformation auf einige μm . Bei der **Proton-Proton-Streuung** werden keine He-Ionen sondern ein hochenergetischer Protonenstrahl auf die Probe fokussiert. Durch die Wechselwirkung der eingestrahlten Protonen mit den Probenwasserstoffatomen werden signifikante Streueignisse induziert. Reaktionsprodukte sind zwei elastisch gestreute Protonen, die die Probe in Transmission durchqueren und von zwei gegenüberliegenden Siliziumdetektoren in Koinzidenz registriert werden, an denen sie zur selben Zeit in einem definierten Winkel eintreffen. Die Koinzidenzmessung wird benutzt, um die Proton-Proton-Ereignisse von anderen Streueignissen zu filtern und man erhält ein nahezu untergrundfreies Wasserstoffsignal. Aus der Anzahl der Protonenereignisse und dem für Wasserstoff bekannten Streuquerschnitt erhält man direkt die absolute Wasserstoffkonzentration der Probe. Aus Energieverlustanalysen können gleichzeitig Tiefenprofile erzeugt werden. Analog zur elastischen Rückstreudetektionsanalyse ist es so möglich, Oberflächenwasser vom eigentlichen Wassergehalt der Probe zu separieren. Letztere Methode, obwohl bisher nur selten in den Geowissenschaften genutzt, ist vielversprechend für die Quantifizierung von Spurenwasserstoffgehalten, zieht man angestrebte Empfindlichkeiten im sub-ppm Bereich bei sub- μm Auflösungen in Betracht.

Die am häufigsten genutzte Methode zur Wasserquantifizierung bleibt jedoch die IR-Spektroskopie, die sich unter anderem durch eine hohe Empfindlichkeit, durch eine verhältnismässig einfache Handhabung und eine breite Verfügbarkeit auszeichnet. Für nominell wasserfreie Minerale wird trotz methodischer Fortschritte und Einführung neuer Extinktionskoeffizienten zumeist die Kalibrierung von Paterson (1982) angewandt (z. B. Mosenfelder 2000; Bolfan-Casanova et al. 2000; Katayama & Nakashima 2002). So gewonnene Werte können daher nur als erste Schätzungen betrachtet werden. Grundlagen für die Interpretation geophysikalischer Daten und somit für eine Modellierung dynamischer

Prozesse in Erdkruste und –mantel bilden jedoch absolute Wasserkonzentrationen. Die Kenntnis diskreter Veränderungen chemischer und physikalischer Mineraleigenschaften als Funktion des absoluten Wassergehaltes ist notwendig, um einen dynamischen inneren Wasserkreislauf zu beschreiben.

Es wäre wünschenswert und bleibt zu hoffen, dass es in nicht allzu ferner Zukunft möglich sein sollte, die Geschichte des Wassers auf der Erde, von seiner Bildung bis heute, zu kennen, um einen der wichtigsten, aber bisher leider am wenigsten verstandenen Prozesse der Erde, den globalen Wasserkreislauf, besser nachvollziehen zu können.

Einen Beitrag zur aktuellen Forschung auf diesem Gebiet soll die vorliegende Dissertation leisten. Die Aufgabenstellung dieser Arbeit beinhaltet die Synthese nominell wasserfreier Minerale, die Untersuchung verantwortlicher Hydratationsmechanismen und die Quantifizierung der Wassergehalte mit Hilfe unabhängiger Methoden, um schliesslich neue mineralspezifische Extinktionskoeffizienten für die IR-Spektroskopie zu bestimmen. Im Rahmen dieses Projektes wurden unter anderem Quarz, Coesit, Stishovit, Olivin, Ringwoodit, Germanate, Granat und Staurolith untersucht. Die vorliegende Arbeit ist in drei Teile untergliedert. Jeder Teil stellt dabei eine Einzelpublikation dar, die jeweils zur Veröffentlichung in internationalen Fachzeitschriften eingereicht wurden (Kapitel 1 und 2) oder werden (Kapitel 3). Die englischsprachigen Manuskripte wurden in Zusammenarbeit mit kollaborierenden Wissenschaftlern verfasst. Im Folgenden werden kurze Einführungen in die drei Einzelpublikationen gegeben:

Der **erste Teil** (Kapitel 1) beschäftigt sich mit der Verwendung von Germanat-Hochdruckmodellen zur Untersuchung des Wasserstoffeinbaus in Erdmantelsilikate. In zahlreichen experimentellen Studien wurden bedeutende Wassergehalte in nominell wasserfreien Mantelmineralen, wie z. B. Ringwoodit, nachgewiesen (z. B. Kohlstedt et al. 1996). Spezifische Einbaumechanismen und die Löslichkeiten von Wasser in nominell wasserfreien Mineralen sowie auch in nominell wasserhaltigen Mantelphasen, wie z. B. Superhydrous

Phase B, sind von besonderem Interesse, um deren Rolle für die Aufrechterhaltung des Wasserkreislaufs der Erde zu definieren. Zur Untersuchung von Hochdruckphasen werden häufig Germanium-Analoga verwendet. Germanate benötigen geringere Drucke für Phasenübergänge und eignen sich daher als Hochdruckmodelle für Silikate (z. B. Ringwood 1975). Zahlreiche Studien von Germanaten lieferten so in der Vergangenheit wichtige Informationen zu Kristallchemie, Struktur, Stabilitätsbereichen und Phasentransformationen wichtiger Erdmantelminerale (z.B. Ohtani et al. 2001). Die Wassereinbaumechanismen sind jedoch weitgehend unerforscht. Basierend auf atomistischen Modellierungen von OH-Defekten in Ge-Ringwoodit befürworteten Blanchard et al. (2005a, b) die Benutzung von Germanatmodellen für die Untersuchung der Hydratationsmechanismen in nominell wasserfreien Mineralen. Es existiert bis dato jedoch nur eine experimentelle Modellstudie für Ge-Ringwoodit mit 5-10 Gew.-ppm H₂O (Hertweck & Ingrin 2005).

Ziel dieser Arbeit ist es, die Anwendbarkeit von Germanatmodellen für Aussagen über den qualitativen und quantitativen Wassereinbau in Mantelsilikate zu untersuchen. Für diesen Zweck wurden Ge-Analoga von Ringwoodit, Anhydrous Phase B und Superhydrous Phase B synthetisiert und mit verschiedenen analytischen und spektroskopischen Methoden charakterisiert. Basierend auf Röntgenverfeinerungsdaten und IR-Spektren werden Hydratationsmechanismen für Ge-Ringwoodit und Ge-Anhydrous Phase B vorgeschlagen. Die Ergebnisse für die Germaniumphasen werden mit Literaturdaten ihrer Silikatäquivalente verglichen, um abschliessend die Anwendung von Germanaten als Hochdruckmodelle zu diskutieren.

Der **zweite Teil** (Kapitel 2) beschäftigt sich mit der Bestimmung von Wassergehalten in amorphen und isotropen Materialien, wie Gläsern und Granaten unter Benutzung der konfokalen Ramanspektroskopie. Letztere Methode hat sich in Verbindung mit einer externen Kalibrierung, der sogenannten „Komparator-Technik“, für die Bestimmung von Wassergehalten von 0.1 bis 40 Gew.-% in natürlichen und synthetischen Gläsern bewährt (z. B. Thomas & Davidson 2006). Die untere Nachweisgrenze ist jedoch unerforscht.

Ziel dieser Arbeit ist es, die Anwendbarkeit konfokaler Ramanspektroskopie für die Bestimmung von Wassergehalten im ppm-Bereich zu untersuchen. Ferner soll die Eignung dieser Quantifizierungstechnik für isotrope Minerale geprüft werden.

Im **dritten Teil** (Kapitel 3) werden verschiedene unabhängige Quantifizierungsmethoden verwendet, um mineralspezifische IR-Extinktionskoeffizienten für die Wasserstoffbestimmung in nominell wasserfreien Mineralen zu berechnen, da bekannt ist, dass allgemein gültige IR-Kalibrierungen für die Wasserbestimmung in Festkörpern nicht für nominell wasserfreie Minerale geeignet sind (z. B. Rossman 2006). In dieser Arbeit wurden Olivin und SiO₂-Polymorphe mit isoliert eingebauten OH-Punktdefekten synthetisiert, z. B. Quarz, Coesit und Stishovit mit $B^{3+} + H^+ = Si^{4+}$ und/oder $Al^{3+} + H^+ = Si^{4+}$ Substitutionen. Die Wassergehalte der Syntheseprodukte sowie einzelner natürlicher Proben wurden unter Anwendung von pp-Streuung, konfokaler Ramanspektroskopie und SIMS quantifiziert. Die resultierenden Daten wurden für die Berechnung neuer mineralspezifischer Extinktionskoeffizienten für die IR-Spektroskopie genutzt, um abschliessend deren Abhängigkeiten von spezifischen OH-Defekten zu diskutieren.

Im Rahmen dieser Einführung konnten viele Aspekte dieses Forschungszweigs nur kurz angesprochen werden. Detaillierte Informationen kann der Leser in der jeweilig angegebenen Literatur finden. Des Weiteren empfiehlt es sich, kürzlich erschienene Überblicksbände wie z. B. Libowitzky & Beran (2004), Keppler & Smyth (2006) oder Jacobsen & van der Lee (2006) zu studieren.

Referenzen

- Aines, R.D. & Rossman, G.R. (1984) Water content of mantle garnets. *Geology*, 12, 720-723.
- Aines, R.D. & Rossman, G.R. (1986) Relationships between radiation damage and trace water in zircon, quartz, and topaz. *American Mineralogist*, 71, 1186-1193.
- Asimow, P. D., J. E. Dixon, Langmuir, C.H. (2004), A hydrous melting and fractionation model for mid-ocean ridge basalts: application to the mid-atlantic ridge near the Azores, *Geochemistry Geophysics Geosystems*, 5, doi:10.1029/2003GC000568.
- Aubaud, C., Withers, A.C., Hirschmann, M.M., Guan, Y., Leshin, L.A., Mackwell, S.J., Bell, D.R. (2007) Intercalibration of FTIR and SIMS for hydrogen measurements in glasses and nominally anhydrous minerals. *American Mineralogist*, 92, 811-828.
- Bell, D.R. & Rossman, G.R. (1992) Water in earth's mantle: the role of nominally anhydrous minerals. *Science*, 255, 1391-1397.
- Bell, D.R., Ihinger, P.D., Rossman, G.R. (1995) Quantitative analysis of trace OH in garnet and pyroxene. *American Mineralogist*, 80, 465-474.
- Bell, D.R., Rossman, G.R., Maldener, J., Endisch, D., Rauch, F. (2003) Hydroxide in olivine: a quantitative determination of the absolute amount and calibration of the IR spectrum. *Journal of Geophysical Research*, 108(B2), 2105-2113.
- Bell, D.R., Rossman, G.R., Moore, R.O. (2004) Abundance and partitioning of OH in a high-pressure magmatic system: Megacrysts from the Monastery kimberlite, South Africa. *Journal of Petrology*, 45(8), 1539-1564.
- Beran, A. (1999) Contribution of IR spectroscopy to the problem of water in the earth's mantle. In K. Wright and R. Catlow, Eds., *Microscopic Properties and Processes in Minerals*, NATO Science Series, Kluwer Academic Publishers, 523-538.
- Beran, A. & Libowitzky, E. (2006) Water in natural mantle minerals II: olivine, garnet and accessory minerals. In H. Keppler and J.R. Smyth, Eds., *Water in nominally anhydrous minerals*, 169-191, Mineralogical Society of America, Chantilly.
- Beran, A., Libowitzky, E., Armbruster, T. (1996) A single-crystal infrared spectroscopic and X-ray diffraction study of untwinned San Benito perovskite containing OH groups. *Canadian Mineralogist*, 34, 803-809.
- Blanchard, M., Wright, K., Gale, J.D. (2005a) Atomistic simulation of Mg_2SiO_4 and Mg_2GeO_4 spinels: a new model. *Physics and Chemistry of Minerals*, 32 (5-6), 585-593.
- Blanchard, M., Wright, K., Gale, J.D. (2005b) A computer simulation study of OH defects in Mg_2SiO_4 and Mg_2GeO_4 spinels. *Physics and Chemistry of Minerals*, 32 (8-9), 585-593.

- Bolfan-Casanova, N., Keppler, H., Rubie, D.C. (2000) Water partitioning between nominally anhydrous minerals in the MgO-SiO₂-H₂O system up to 24 GPa: implications for the distribution of water in the earth's mantle. *Earth and Planetary Science Letters*, 182, 209-221.
- Brunner, G.O., Wondratschek, H., Laves, F. (1961) Ultrarotuntersuchung über den Einbau von H in natürlichem Quarz. *Zeitschrift für Elektrochemie*, 65, 735-750.
- Chakraborty, D. & Lehmann, G. (1976) On the structures and orientations of hydrogen defects in natural and synthetic quartz crystals. *Physica status solidi, A*, 34, 467-474.
- Cho, H. & Rossman, G.R. (1993) Single-crystal NMR studies of low-concentration hydrous species in minerals: grossular garnet. *American Mineralogist*, 78, 1149-1164.
- Deloule, E., Paillat, O., Pichavant, M., Scaillet, B. (1995) Ion microprobe determination of water in silicate glasses: methods and applications. *Chemical geology*, 125, 19-28.
- Demouchy, S. (2004) Water in the earth's interior: Thermodynamics and kinetics of hydrogen incorporation in olivine and wadsleyite. 165 p. PhD thesis, Universität Bayreuth.
- Dimanov, A., Dresen, G., Xiao, X., Wirth, R. (1999) Grain boundary diffusion creep of synthetic anorthite aggregates: the effect of water. *Journal of Geophysical Research*, 104, 10483-10497.
- Dimanov, A., Lavie, M.P., Dresen, G., Ingrin, J., Jaoul, O. (2003) Creep of polycrystalline anorthite and diopside. *Journal of Geophysical Research*, 108, B1, doi: 10.1029/2002JB001815.
- Dobson, D.P., Meredith, P.G., Boon, S.A. (2002) Simulation of subduction zone seismicity by dehydration of serpentine. *Science*, 298, 1407-1410.
- Frost, D.J. (2006) The stability of hydrous mantle phases. In H. Keppler and J.R. Smyth, Eds., *Water in nominally anhydrous minerals. Reviews in Mineralogy and Geochemistry*, 62, 243-271, Mineralogical Society of America, Chantilly.
- Griggs, D.T. (1967) Hydrolytic weakening of quartz and other silicates. *Geophysical Journal of the Royal Astronomical Society*, 14, 19-31.
- Hammer, V.M.F., Beran, A., Endisch, D., Rauch, F. (1996) OH concentrations in natural titanites determined by FTIR spectroscopy and nuclear reaction analysis. *European Journal of Mineralogy*, 8, 281-288.
- Hauri, E., Wang, J., Dixon, J.E., King, P.L., Mandeville, C., Newman, S. (2002) SIMS analysis of volatiles in volcanic glasses, 1, calibration, matrix effects and comparisons with FTIR. *Chemical geology*, 183, 99-114.
- Hawthorne, F.C., Groat, L.A., Raudsepp, M., Ball, N.A., Kimata, M., Spike, F.D., Gaba, R., Halden, N.M., Lumpkin, G.R., Ewing, R.C., Gregor, R.B., Lytle, F.W., Ercit, T.S., Rossman, G.R., Wicks, F.J., Ramik, R.A., Sherriff, B.L., Fleet, M.E., McCammon, C. (1991) Alpha-decay damage in titanite. *American Mineralogist*, 76, 370-396.
- Hawthorne, F.C. (1992) The role of OH and H₂O in oxide and oxysalt minerals. *Zeitschrift für Kristallographie*, 201, 183-206.

- Hertweck, B. & Ingrin, J. (2005) Hydrogen incorporation in a ringwoodite analogue: Mg_2GeO_4 spinel. *Mineralogical Magazine*, 69, 337-343.
- Hervig, R.L., Stanton, T.R., Williams, P. (1987) Ion probe microanalyses of hydrogen in glasses and minerals (abstr). *EOS*, 68, 441.
- Hier-Majumder, S., Anderson, I.M., Kohlstedt, D.L. (2005) Influence of protons on Fe-Mg interdiffusion in olivine. *Journal of Geophysical Research*, 110, doi:10.1029/2004JB003292.
- Hirschmann, M.M. (2006) Water, melting, and the deep earth H_2O cycle. *The Annual Review of Earth and Planetary Science*, 34, 629-653.
- Hirschmann, M.M., Aubaud, C., Withers, A.C. (2005) Storage capacity of H_2O in nominally anhydrous minerals in the upper mantle. *Earth and Planetary Science Letters*, 236, 167-181.
- Hirth, G. & Kohlstedt, D.L. (1996) Water in the oceanic upper mantle: implications for rheology, melt extraction and the evolution of the lithosphere. *Earth and Planetary Science Letters*, 144, 93-108.
- Hirth, G. & Kohlstedt, D.L. (2003) Rheology of the upper mantle and the mantle wedge: a view from the experimentalists. In J. Eiler, Ed., *Inside the Subduction Factory*, 138, 311 p., Washington, D.C., American Geophysical Union.
- Huang, X., Xu, Y., Karato, S. (2005) Water content in the transition zone from electrical conductivity of wadsleyite and ringwoodite. *Nature*, 434, 746-749.
- Ingrin, J. & Skogby, H. (2000) Hydrogen in nominally anhydrous upper-mantle minerals: concentrations levels and implications. *European Journal of Mineralogy*, 12, 543-570.
- Ingrin, J. & Blanchard, M. (2006) Diffusion of hydrogen in minerals. In H. Keppler and J.R. Smyth, Eds., *Water in nominally anhydrous minerals. Reviews in Mineralogy and Geochemistry*, 62, 291-320, Mineralogical Society of America, Chantilly.
- Inoue, T., Yurimoto, H., Kudoh, Y. (1995) Hydrous modified spinel, $\text{Mg}_{1.75}\text{SiH}_{0.5}\text{O}_4$: a new water reservoir in the mantle transition region. *Geophysical Research Letters*, 22, 117-120.
- Ito, E., Harris, D.M., Anderson, A.T. (1983) Alteration of oceanic crust and geologic cycling of chlorine and water. *Geochimica et Cosmochimica Acta*, 47, 1613-1624.
- Jacobsen, S.D. & van der Lee, S. (2006) Earth's deep water cycle. *Geophysical monograph series*, 168, 313 p. American Geophysical Union, Washington, D.C.
- Jacobsen, S.D., Smyth, J.R., Spetzler, H., Holl, C.M., Frost, D.J. (2004) Sound velocities and elastic constants of iron-bearing hydrous ringwoodite. *Physics of the Earth and Planetary Interiors*, 143-144, 47-56.
- Jacobsen, S.D., Demouchy, S., Frost, D.J., Ballaran, T.B., Kung, J. (2005) Systematic study of OH in hydrous wadsleyite from polarized FTIR spectroscopy and single-crystal X-ray diffraction: oxygen sites for hydrogen storage in earth's interior. *American Mineralogist*, 90, 61-70.

- Johnson, E.A. & Rossman, G.R. (2003) The concentration and speciation of hydrogen in feldspars using FTIR and ^1H MAS NMR spectroscopy. *American Mineralogist*, 88, 901-911.
- Johnson, E.A. & Rossman, G.R. (2004) A survey of hydrous species and concentrations in igneous feldspars. *American Mineralogist*, 89, 586-600.
- Johnson, E.A. (2006) Water in nominally anhydrous crustal minerals: speciation, concentration, and geologic significance. In H. Keppler and J.R. Smyth, Eds., *Water in nominally anhydrous minerals. Reviews in Mineralogy and Geochemistry*, 62, 117-154, Mineralogical Society of America, Chantilly.
- Karato, S. (1990) The role of hydrogen in the electrical conductivity of the upper mantle. *Nature*, 347, 272-273.
- Karato, S., Patterson, M.S., Fitzgerald, D. (1986) Rheology of synthetic olivine aggregates: Influence of grain size and water. *Journal of Geophysical Research*, 91, 8151-8176.
- Katayama, I. & Nakashima, S. (2002) Hydroxyl in clinopyroxene from the deep subducted crust: evidence for H_2O transport into the mantle. *American Mineralogist*, 88, 229-234.
- Kats, A. (1962) Hydrogen in alpha quartz. *Phillips Research Report*, 17, 133-279.
- Kats, A. & Haven, Y. (1960) Infrared absorption bands in α -quartz in the $3\text{-}\mu$ region. *Physics and Chemistry of Glasses*, 1, 99-102.
- Kavner, A. (2003) Elasticity and strength of hydrous ringwoodite at high pressure. *Earth and Planetary Science Letters*, 214, 645-654.
- Kekulawala, K.R.S.S., Paterson, M.S., Boland, J.N. (1981) An experimental study of the role of water in quartz deformation. *Geophysical Monograph*, 24, 49-60.
- Keppler, H. & Rauch, F. (2000) Water solubility in nominally anhydrous minerals measured by FTIR and ^1H MAS NMR spectroscopy: the effect of sample preparation. *Physics and Chemistry of Minerals*, 27, 371-376.
- Keppler, H. & Bolfan-Casanova, N. (2006) Thermodynamics of water solubility and partitioning. In H. Keppler and J.R. Smyth, Eds., *Water in nominally anhydrous minerals, Reviews in Mineralogy and Geochemistry*, 62, 193-230, Mineralogical Society of America, Chantilly.
- Keppler, H. & Smyth, J.R. (2006) Water in nominally anhydrous minerals. *Reviews in Mineralogy and Geochemistry*, 62, Mineralogical Society of America, 478 p., Chantilly.
- Koch-Müller, M., Fei, Y., Hauri, E., Liu, Z. (2001) Location and quantitative analysis of OH in coesite. *Physics and Chemistry of Minerals*, 28, 693-705.
- Koch-Müller, M., Matsyuk, S.S., Rhede, D., Wirth, R., Khisina, N. (2006) Hydroxyl in mantle olivine xenocrysts from the Udachnaya kimberlite pipe. *Physics and Chemistry of Minerals*, 33, 276-287.
- Koga, K., Hauri, E., Hirschmann, M., Bell, D. (2003) Hydrogen concentration analyses using SIMS and FTIR: comparison and calibration for nominally anhydrous minerals. *Geochemistry Geophysics Geosystems*, 4, 1019-1039.

- Kohlstedt, D.L. (2006) The role of water in high-temperature rock deformation. In H. Keppler and J.R. Smyth, Eds., *Water in nominally anhydrous minerals, Reviews in Mineralogy and Geochemistry*, 62, 377-396, Mineralogical Society of America, Chantilly.
- Kohlstedt, D.L. & Mackwell, S.J. (1998) Diffusion of hydrogen and intrinsic point defects in olivine. *Zeitschrift für Physikalische Chemie*, 207, 147-162.
- Kohlstedt, D.L., Keppler, H., Rubie, D.C. (1996) The solubility of water in α , β and γ phases of $(\text{Mg,Fe})_2\text{SiO}_4$. *Contributions to Mineralogy and Petrology*, 123, 345-357.
- Kohn, S.C. (1996) Solubility of H_2O in nominally anhydrous mantle minerals using ^1H MAS NMR. *American Mineralogist*, 81, 1523-1526.
- Kronenberg, A.K. (1994) Hydrogen speciation and chemical weakening of quartz. In P.J. Heaney, C.T. Prewitt and G.V. Gibbs, Eds., *Silica: Physical behavior, geochemistry and materials applications, Reviews in Mineralogy*, 29, 123-176, Mineralogical Society of America, Washinton, D.C.
- Kronenberg, A.K. & Wolf, G.H. (1990) Fourier transform infrared spectroscopy determinations of intragranular water content in quartz-bearing rocks: implications for hydrolytic weakening in the laboratory and within the earth. *Tectonophysics*, 172, 255-271.
- Kronenberg, A.K., Kirby, S.H., Aines, R.D., Rossman, G.R. (1986) Solubility and diffusional uptake of hydrogen in quartz at high water pressures: implications for hydrolytic weakening. *Journal of Geophysical research*, 91, 12723-12744.
- Kudoh, Y., Inoue, T., Arashi, H. (1996) Structure and crystal chemistry of hydrous wadsleyite, $\text{Mg}_{1.75}\text{SiH}_{0.5}\text{O}_4$: possible hydrous magnesium silicate in the mantle transition zone. *Physics and Chemistry of Minerals*, 23, 461-469.
- Kurka, A. (2005) Hydrogen in Ca-rich garnets: diffusion and stability of OH-defects. PhD Dissertation, University Paul Sabatier, Toulouse, France.
- Kurosawa, M., Yurimoto, H., Matsumoto, K., Sueno, S. (1992) Hydrogen analysis of mantle olivine by secondary ion mass spectrometry. In Y. Xyono and M. H. Manghnani, Eds., *High-pressure research: application to earth and planetary sciences*, 283-287, Terra Sci., Tokyo.
- Lager, G.A., Armbruster, T., Rotella, F.J., Rossman, G.R. (1989) OH substitution in garnets: X-ray and neutron diffraction, infrared, and geometric-modeling studies. *American Mineralogist*, 74, 840-851.
- Lager, G.A., Marshall, W.G., Liu, Z., Downs, R.T. (2005) Re-examination of the hydrogarnet structure at high pressure using neutron powder diffraction and infrared spectroscopy. *American Mineralogist*, 90, 639-644.
- Lathe, C., Koch-Müller, M., Wirth, R., van Westrenen, W., Müller, H.-J., Schilling, F., Lauterjung, J. (2005) The influence of OH in coesite on the kinetics of the coesite-quartz phase transition. *American Mineralogist*, 90, 36-43.
- Libowitzky, E. & Rossman, G.R. (1997) An IR absorption calibration for water in minerals. *American Mineralogist*, 82, 1111-1115.

- Libowitzky, E. & Beran, A. (1995) OH defects in forsterite. *Physics and Chemistry of Minerals*, 22, 387-392.
- Libowitzky, E. & Beran, A. (2004) IR spectroscopic characterisation of hydrous species in minerals. In A. Beran and E. Libowitzky, Eds., *Spectroscopic methods in mineralogy*. EMU Notes in Mineralogy, 6, 227-279, Eötvös University Press, Budapest, Hungary.
- Libowitzky, E. & Beran, A. (2006) The structure of hydrous species in nominally anhydrous minerals: information from polarized IR spectroscopy. In H. Keppler and J.R. Smyth, Eds., *Water in nominally anhydrous minerals*, *Reviews in Mineralogy and Geochemistry*, 62, 29-52, Mineralogical Society of America, Chantilly.
- Lu, R. & Keppler, H. (1997) Water solubility in pyrope to 100 kbar. *Contributions to Mineralogy and Petrology*, 129, 35-42.
- Mackwell, S.J., Kohlstedt, D.L., Paterson, M.S. (1985) The role of water in the deformation of olivine single crystals. *Journal of Geophysical Research*, 90, 11319-11333.
- Maldener, J., Rauch, F., Gavranic, M., Beran, A. (2001) OH absorption coefficients of rutile and cassiterite deduced from nuclear reaction analysis and FTIR spectroscopy. *Mineralogy and Petrology*, 71, 21-29.
- Maldener, J., Hösch, A., Langer, K., Rauch, F. (2003) Hydrogen in some natural garnets studied by nuclear reaction analysis and vibrational spectroscopy. *Physics and Chemistry of Minerals*, 30, 337-344.
- Martin, R.F. & Donnay, G. (1972) Hydroxyl in the mantle. *American Mineralogist*, 57, 554-570.
- Mosenfelder, J.L. (2000) Pressure dependence of hydroxyl solubility in coesite. *Physics and Chemistry of Minerals*, 27, 610-617.
- Ohtani, E., Toma, M., Litasov, K., Kubo, T., Suzuki, A. (2001) Stability of dense hydrous magnesium silicate phases and water storage capacity in the transition zone and lower mantle. *Physics of the Earth and Planetary Interiors*, 124, 105-117.
- Ohtani, E. (2005) Water in the mantle. *Elements*, 1, 25-30.
- Paterson, M. S. (1982) The determination of hydroxyl by infrared absorption in quartz, silicate glasses and similar materials. *Bulletin de Minéralogie*, 105, 20-29.
- Pawley, A.R., McMillan, P.F., Holloway, J.R. (1993) Hydrogen in Stishovite, with Implications for Mantle Water Content, *Science*, 261, 1024-1026.
- Peslier, A.H. & Luhr, J.F. (2006) Hydrogen loss from olivines in mantle xenoliths from Simcoe (USA) and Mexico: Mafic alkalic magma ascent rates and water budget of the sub-continental lithosphere. *Earth and Planetary Science Letters*, 242, 302-319.
- Prewitt, C.T. & Parise, J.B. (2000) Hydrous phases and hydrogen bonding at high pressure. In R.M. Hazen, Ed., *Crystal chemistry at high pressures and temperatures*. *Reviews in Mineralogy*, 41, 309-334, Mineralogical Society of America, Washington, D.C.

- Reichart, P., Datzmann, G., Hauptner, A., Hertenberger, R., Wild, C., Dollinger, G. (2004) Three-Dimensional Hydrogen Microscopy in Diamond. *Science*, 306, 1537-1540.
- Rhede, D. & Wiedenbeck, M. (2006) SIMS quantification of very low hydrogen contents. *Applied Surface Science*, 252, 7152-7154.
- Ringwood, A.E. (1966) The chemical composition and origin of the earth. In P.M. Hurley, Ed., *Advances in Earth Sciences*, MIT Press, 287-356.
- Ringwood, A.E. (1975) *Composition and petrology of the earth's mantle*. 618 p. McGraw-Hill, New York.
- Rossman, G.R. (1988) Vibrational spectroscopy of hydrous components. In F.C. Hawthorne, Ed., *Spectroscopic methods in mineralogy and geology*. *Reviews in Mineralogy*, 18, 193-206, Mineralogical Society of America, Washington, D.C.
- Rossman, G.R. & Aines, R.D. (1991) The hydrous component in garnets: grossular-hydrogrossular. *American Mineralogist*, 76, 1153-1164.
- Rossman, G.R., Rauch, F., Livi, R., Tombrello, T.A., Shi, C.R., Zhou, Z.Y. (1988) Nuclear reaction analysis of hydrogen in almandine, pyrope and spessartite garnets. *Neues Jahrbuch für Mineralogie, Monatshefte*, 172-178.
- Rüpke, L.H., Phillips Morgan, J.P., Hort, M., Conolly, J.A.D. (2004) Serpentine and the subduction zone water cycle. *Earth and Planetary Science Letters*, 223, 17-34.
- Rybacki, E. & Dresen, G. (2000) Dislocation and diffusion creep of synthetic anorthite aggregates. *Journal of Geophysical Research*, 105, B11, 26017-26036.
- Rybacki, E. & Dresen, G. (2004) Deformation mechanism maps for feldspar rocks. *Tectonophysics*, 382, 173-187.
- Skogby, H., Bell, D.R., Rossman, G.R. (1990) Hydroxide in pyroxene: Variations in the natural environment. *American Mineralogist*, 75, 764-774.
- Smyth, J.R. (1987) β - Mg_2SiO_4 : a potential host for water in the mantle? *American Mineralogist*, 72, 1051-1055.
- Smyth, J.R. (2006) Hydrogen in high pressure silicate and oxide mineral structures. In H. Keppler and J.R. Smyth, Eds., *Water in nominally anhydrous minerals*, *Reviews in Mineralogy and Geochemistry*, 62, 85-115, Mineralogical Society of America, Chantilly.
- Smyth, J.R. & Frost, D.J. (2002) The effect of water on the 410-km discontinuity: an experimental study. *Geophysical Research Letters*, 1485, doi: 10.1029/2001GL014418.
- Smyth, J.R., Swope, R.J., Pawley, A.R. (1995) H in rutile-type compounds: II. Crystal chemistry of Al substitution in H-bearing stishovite. *American Mineralogist*, 80, 454-456.
- Smyth, J.R., Holl, C., Frost, D.J., Jacobsen, S.D., Langenhorst, F., McCammon, C.A. (2003) Structural systematics of hydrous ringwoodite and water in earth's interior. *American Mineralogist*, 88, 1402-1407.

- Smyth, J.R., Frost, D.J., Nestola, F., Holl, C.M., Bromiley, G. (2006) Olivine hydration in the deep upper mantle: effects of temperature and silica activity. *Geophysical Research Letters*, 33, doi: 2006GL026194.
- Sweeney, R.J., Prozesky, V.M., Springhorn, K.A. (1997) Use of elastic recoil detection analysis (ERDA) microbeam technique for the quantitative determination of hydrogen in materials and hydrogen partitioning between olivine and melt at high pressures. *Geochimica and Cosmochimica Acta*, 61, 101-113.
- Thomas, R. and Davidson, P. (2006) Progress in the determination of water in glasses and melt inclusions with Raman spectroscopy: A short review. *Zeitschrift für geologische Wissenschaften*, Berlin, 34, 159-163.
- Thompson, A.B. (1992) Water in the earth's upper mantle. *Nature*, 358, 295-302.
- Wang, D., Mookherjee, M., Xu, Y., Karato, S. (2006) The effect of hydrogen on the electrical conductivity in olivine. *Nature*, 443, 977-980.
- Wegdén, M., Kristiansson, P., Skogby, H., Auzelyte, V., Elfman, M., Malmqvist, K.G., Nilsson, C., Pallon, J., Shariff, A. (2005) Hydrogen depth profiling by p-p scattering in nominally anhydrous minerals. *Nuclear Instruments and Methods in Physics Research, B*, 231, 524-529.
- Wood, B.J. (1995) The effect of H₂O on the 410-kilometer seismic discontinuity. *Science*, 268, 74-76.
- Wright, K., Freer, R., Catlow, C.R.A. (1994) Energetics and structure of the hydrogarnet defect in grossular: a computer simulation study. *Physics and Chemistry of Minerals*, 20, 500-504.
- Yurimoto, H., Kurosawa, M., Sueno, S. (1989) Hydrogen analysis in quartz crystals and quartz glasses by secondary ion mass spectrometry. *Geochimica and cosmochimica Acta*, 53, 751-755.

Kapitel 1

**“Protonation in germanium equivalents of ringwoodite, anhydrous
phase B and superhydrous phase B”**

Protonation in germanium equivalents of ringwoodite, anhydrous phase B and superhydrous phase B

Sylvia-Monique Thomas¹, Monika Koch-Müller¹, Volker Kahlenberg², Rainer Thomas¹, Dieter Rhede¹, Richard Wirth¹, and Bernd Wunder¹

¹ GeoForschungsZentrum Potsdam (GFZ), Telegrafenberg, 14473 Potsdam, Germany, Section 4.1.

E-mail: smthomas@gfz-potsdam.de

² Institute for Mineralogy / Petrography, University Innsbruck, Innrain 52, A-6020 Innsbruck, Austria.

Abstract

To gain insight into hydroxyl solubilities and possible hydration mechanisms of mantle silicates, as well as to test the utility of germanium analogue models in studies of water-related defects, our present work is focused on the protonation of germanium analogues of silicates.

For this purpose Ge-analogues of ringwoodite, anhydrous phase B (anhB), and for the first time, superhydrous phase B (shyB), were synthesized in a piston cylinder device at 2 GPa and 950-1000 °C under water-excess conditions. Electron probe microanalysis (EPMA), Transmission electron microscopy (TEM), and X-ray diffraction as well as Raman and infrared (IR) spectroscopy were used to characterize the experimental products.

Ge-ringwoodite incorporates from 900 to 2200 ppm H₂O by weight, which is much less than Smyth et al. (2003) observed for the Si-equivalent synthesized at 22 GPa and 1500 °C, but up to 200 times more than published for γ -Mg₂GeO₄ by Hertweck and Ingrin (2005). In addition to this discrepancy, the incorporation mechanism of H in Ge-ringwoodite also differs from that of Si-ringwoodite.

Ge-anhB, which is currently believed to be anhydrous in the Si-system, contains from 2400 to 5300 ppm water by weight. A hydration model for germanate anhB was constructed based on single-crystal X-ray diffraction analysis and IR spectroscopy, in which OH is incorporated via the hydrogarnet substitution $[V_{\text{Ge}} \cdot 4(\text{OH})_{\text{O}}]^{\times}$ and via vacant Mg sites $[V_{\text{Mg}} \cdot 2(\text{OH})_{\text{O}}]^{\times}$.

For Ge-shyB the water concentration and incorporation mechanism obtained in this study are identical to results reported for the silicate phase synthesized at 22 GPa and 1200 °C (Koch-Müller et al. 2005). Thus, germanates are good low-pressure analogues for hydrous mantle silicates in which protonation is controlled by stoichiometry. However, for nominally anhydrous minerals we cannot recommend the use of germanates as high-pressure models in water-related studies. In these Ge-analogues, which are usually synthesized at much lower pressures, i.e., lower water fugacities, OH incorporation seems to differ from the high-pressure silicate equivalents qualitatively and quantitatively, as hydroxyl solubility is governed by other factors such as water fugacity and intrinsic defects.

Keywords: germanates, ringwoodite, nominally anhydrous minerals, FTIR, anhydrous phase B, superhydrous phase B

Introduction

A significant number of high-pressure and high-temperature experiments have been carried out in the past to characterize phase relations in the system $\text{MgO-SiO}_2\text{-H}_2\text{O}$ (MSH). Numerous investigations have established that major mantle constituents, e.g., olivine and its two dense polymorphs, are able to dissolve several wt% water, although their formulas indicate that they are nominally anhydrous minerals (NAMs) (e.g., Kohlstedt et al. 1996, Smyth 1987; Smyth et al. 1997; Kudoh et al. 2000; Bolfan-Casanova et al. 2000; Kleppe et al. 2002; Kohn et al. 2002). Cubic ringwoodite [$\gamma\text{-(Mg,Fe)}_2\text{SiO}_4$] with the space group $\text{Fd } \bar{3}m$ is one of the most abundant minerals in the Earth's transition zone from about 525 to 660 km depth. Therefore, the ability to store hydroxyl in its structure is of particular interest. With the same motivation a large variety of dense hydrous magnesium silicates, first discovered by Ringwood and Major (1967), have been recognized, that are stable at very high pressure and temperature and cover a wide range of water and silica contents (e.g., phase D, phase E; e.g., Yamamoto and Akimoto 1974; Akaogi and Akimoto 1986; Kato and Kumazawa 1985; Kanzaki 1991; Gasparik 1993; Luth 1993; Cynn et al. 1996; Frost 1999; Ohtani et al. 2001, Ganguly and Frost 2006). One of these phases is anhB ($\text{Mg}_{14}\text{Si}_5\text{O}_{24}$) with an atomic Mg/Si ratio of 2.8. It was first synthesized at 2380 °C and 16.5 GPa by Herzberg and Gasparik (1989). Another phase in the MSH system is shyB [$\text{Mg}_{10}\text{Si}_3\text{O}_{14}(\text{OH})_4$], a nominally hydrous phase with an atomic Mg/Si ratio of 3.3, and 5.8 wt% of stoichiometrically incorporated water. It was first synthesized at 19 GPa and 1450 °C and described by Gasparik (1993). According to their PT-stabilities these dense hydrous magnesium silicates are potential hosts for water in cold subduction zones. However, whether they really exist in nature is still under debate, if so, their dehydration at hotter parts of the lower mantle could have, among other effects, implications for as yet poorly understood deep-focus earthquakes (Silver et al. 1995). Such examples suggest the geological importance of studying the protonation of compounds in the MSH system, qualitatively and quantitatively, as water dissolved in these minerals may

change their chemical and physical properties, and might have an unforeseen impact on mantle processes.

To investigate such mantle silicates, germanates have been extensively used as analogues. In contrast to silicates, germanates require much lower pressures for specific phase transitions, because at zero pressure tetravalent Ge inherently has a slightly larger atomic radius than tetravalent Si. As shown by Ringwood (1975) phase transformations are controlled by critical effective radius ratios.

In recent studies, Blanchard et al. (2005a, b) modeled OH defects in germanate ringwoodite and suggested using germanium analogues to study the protonation of NAMs. However, only dry Ge-anhB (e.g., von Dreele et al. 1970) and Ge-ringwoodite, containing 5 to 10 wt ppm water (Hertweck and Ingrin 2005), have previously been synthesized as high-pressure models. The data obtained provided useful constraints on structure, crystal chemistry, phase transformations and PT-stabilities. However, the hydrogen incorporation mode in those phases is still largely unknown. The aim of this work is to test the utility of germanium analogue models in studies of water-related defects, and to do this we synthesized the Ge-analogues of ringwoodite, anhB and Ge-shyB. On the basis of X-ray refinements and IR spectra we developed new hydrogen incorporation models for Ge-ringwoodite and Ge-anhB. Furthermore, we compare our results with the associated silicon equivalents and discuss the application of germanates as low-pressure analogues.

Experimental Methods

Syntheses

Starting materials were made up from MgO, Mg(OH)₂ and GeO₂ to give compositions with different MgO-GeO₂ ratios. The starting powders were loaded in 10 mm long gold capsules with an outer diameter of 6 mm and a wall thickness of 0.5 mm and were sealed by cold welding to avoid water loss. All experiments were carried out in an end-loaded piston-cylinder apparatus (Boyd and England 1960) at 2 GPa and 950 °C or 1000 °C with up to 23 wt%

water. Starting mixtures, experimental conditions and compositions of the run products are summarized in Table 1. After quenching, the recovered capsule was opened and checked for the presence of excess water, which could be observed in all runs.

Table 1. Starting compositions, experimental conditions, electron probe microanalyses (wt%) and structural formulae.

| Sample | Starting composition (wt %) | | | p (GPa) | T (°C) | Run duration (h) | Characteristics |
|----------------|-----------------------------|--|------------------|-----------|---|------------------|--|
| | MgO | GeO ₂ | H ₂ O | | | | |
| Ge-anhB | 43.51 | 37.06 | 19.43 | 2 | 1000* | 10 | clear crystals, up to 200 μm, no coexisting phase |
| Ge-Ringwoodite | 43.51 | 46.77 | 9.72 | 2 | 950 | 24 | clear crystals with nearly ideal cubic sections, up to 400 μm in size, no coexisting phase |
| Ge-shyB | 51.88 | 24.95 | 23.17 | 2 | 1000 | 16 | clear crystals of Ge-shyB, up to 50 μm in size, coexisting phases: periclase, brucite |
| Sample | No. anal. | MgO | GeO ₂ | Total | Formula | | |
| Ge-anhB | 28 | 51.18(16) | 48.34(47) | 99.52(51) | Mg _{13.89(6)} Ge _{5.06(3)} O ₂₄ | | |
| Ge-shyB | 12 | 51.33(24) | 40.43(25) | 91.77(32) | Mg _{9.96(3)} Ge _{3.02(2)} O ₁₄ (OH) ₄ | | |
| Notes: | | Numbers in parantheses give 1 σ standard deviation in terms of the preceding figure. | | | | | |
| * | | – Temperature between 1000 and 1100 °C. | | | | | |

Electron probe microanalysis

For chemical analyses several grains of Ge-anhB and Ge-shyB were mounted, polished and coated with carbon. Compositions were measured with a Cameca SX-50 electron microprobe using wavelength-dispersive spectrometers with a PAP correction procedure. The microprobe was operated at 15 kV with a beam current of 20 nA and a spot size of 2 μm . Counting times were 60 s on peaks (Mg, Ge) and 30 s on backgrounds (left and right side of the peaks). Ge-ringwoodite synthesized in this study was used as the standard. This was justified by single-crystal X-ray refinement of this sample (see below).

Transmission electron microscopy

To characterize microstructures, sample homogeneities and compositions by TEM, specific foils were prepared from single crystals mounted in crystal-bond, using the focused-ion-beam technique (Wirth 2004), and a FEI FIB200 focused ion beam device with a Ga-ion source operated with an acceleration voltage of 30 kV. Final foils of $15 \times 10 \times 0.2 \mu\text{m}$ in size were removed from the sample using an optical microscope and placed onto a perforated TEM carbon grid. No further carbon coating was required. TEM analyses of Ge-anhB and Ge-ringwoodite were performed in a Philips CM200 electron microscope operating at 200 kV with a LaB₆ electron source. Ge-shyB was analyzed with a FEI TecnaiTMG² F20 X-Twin at 200 kV equipped with a FEG electron source. Both microscopes are provided with a Gatan imaging filter for the acquisition of energy-filtered images and high-resolution electron micrographs, and an energy-dispersive X-ray spectroscopy system for analytical electron microscopy. Electron diffraction was used to determine the orientation of the samples.

X-ray diffraction

The samples were identified by polarized light microscopy and X-ray diffraction. Table 1 lists the run products with their characteristics. X-ray powder measurements on Ge-shyB were done with a fully automated STOE Stadi P diffractometer, equipped with a curved Ge (111) primary monochromator, a 7°-wide position sensitive detector (PSD) and CuK α -radiation. The X-ray tube was operated at 40 kV and 40 mA, using a take-off angle of 6°. Intensities were recorded in the range of 5 - 125° with a detector step size of 0.1° and a resolution of 0.02°. Unit cell dimensions and lattice parameters were determined using the GSAS software package for Rietveld refinement (Larson and von Dreele 1987).

In addition, small platy specimens of Ge-anhB and Ge-Ringwoodite were measured on a Stoe IPDS-II imaging plate diffractometer at the Mineralogical Institute of the University of Innsbruck, Austria. Parameters pertaining to the data collection and the subsequent structure refinements are summarized in Table 2. All data were numerically corrected for absorption by

use of indexed crystal faces. Further data reduction including Lorentz and polarization corrections was performed with the STOE program package X-RED (XRED, 1996).

Raman spectroscopy

Raman spectra of several sample grains were taken using a Dilor XY Laser Triple 800 mm spectrometer (1800 lines/mm gratings), equipped with a Peltier cooled CCD detector (1024 elements), a Coherent water-cooled Argon Laser, an Olympus optical microscope and a long working distance 80 \times objective (ULWD MSPlan80). The slit width was 100 μm at a corresponding spectral resolution of about 1 cm^{-1} . Other spectra were acquired with a LabRAM HR800 UV-VIS spectrometer with a motorized XY-stage and a long working distance 100 \times objective (LWD VIS, NA = 0.80, WD = 3.4 mm). The 488 nm line of an Ar⁺ Laser (Model Innova 70-3) was generally used for sample excitation, at 450 mW and 500 mW laser power and thus 65.7 mW and 73 mW power on the specimen, respectively. However, the excitation source of some measurements was the 514 nm line of an air-cooled Melles Griot Ar⁺ Laser at 30 mW laser power and a power of 6.5 mW on the sample. The confocal hole of the LabRAM HR800 spectrometer was chosen according to requirements (100 to 300 μm). All spectra were recorded in two frequency ranges, high-frequencies between 2800 and 4000 cm^{-1} and low-frequencies between 200 and 1400 cm^{-1} . Spectra acquisition time varied from 3 \times 10 s to 3 \times 50 s for each window.

Infrared spectroscopy

For the Fourier-transform infrared (FTIR) measurements optically clear single-crystals with smooth crystal faces were selected, and dried for 18 hours at 170 $^{\circ}\text{C}$ (SMT501, SMT507) or 400 $^{\circ}\text{C}$ (SMT502) in a muffle type furnace. The sample thickness was determined under an optical microscope using the eyepiece reticule and a stage micrometer scale for calibration. The final thickness ranged from 45 μm to 90 μm ; errors are estimated as $\pm 5 \mu\text{m}$.

Unpolarized IR spectra of Ge-anhB and Ge-Ringwoodite were recorded from room

temperature down to - 180 °C with a Bruker IFS 66v FTIR spectrometer and a Hyperion microscope, an InSb detector, a KBr beamsplitter, a globar and a Linkam FTIR600 heating/cooling stage. The spot size used in the measurements ranged from $50 \times 50 \mu\text{m}$ to $100 \times 100 \mu\text{m}$, and up to 1024 scans were taken with a resolution of 2 cm^{-1} . To avoid detector saturation due to a strong OH absorbance, IR studies on Ge-shyB were carried out on a thin aggregate of randomly oriented sample particles, produced by crushing a crystal in a Megabar-type diamond anvil cell (DAC) (Mao and Hemley 1998) without a gasket. In-situ IR spectra as a function of pressure were taken in the DAC with type II diamonds (culet sizes of $800 \mu\text{m}$) and a stainless steel gasket. The sample was placed in a $300 \mu\text{m}$ -gasket hole with KBr as pressure medium and ruby grains. For each spectrum 1024 scans were accumulated in the range of $400\text{-}4000 \text{ cm}^{-1}$ with a KBr beam splitter, a MCT detector and 2 cm^{-1} resolution. The pressure was determined using the pressure-dependent energy shift of the R_1 ruby fluorescence line (Mao et al. 1986). High-pressure spectra for the other two samples were collected on single-crystals under the same conditions, but in the $1850 - 4000 \text{ cm}^{-1}$ range.

Polarized IR spectra of single-crystals of Ge-anhB were obtained under the above-mentioned conditions, and in addition with synchrotron radiation at the Infrared beamline at BESSY II using a Nicolet 870 FTIR spectrometer equipped with a Continuum microscope. The orientation of the samples was determined using electron diffraction patterns from TEM analyses (see results). For the polarized spectra 512 scans were collected at 4 cm^{-1} resolution. The absorbance of the oriented single-crystals was measured in extinction position, with the electric vector (E) parallel to each optical indicatrix axis. The integrated intensity, and area-weighted average (Libowitzky and Rossman 1997) of the peak positions were obtained using the PeakFit software by Jandel Scientific. Due to the lack of specific absorption coefficients for Ge-anhB and Ge-Ringwoodite we used the calibration of Libowitzky and Rossman (1997) to quantify the hydrogen content. For Ge-anhB total absorbances were used, i.e., the sum of the fitted integrated intensities measured parallel to the three crystallographic axes. For the unpolarized spectra of $\gamma\text{-Mg}_2\text{GeO}_4$ total absorbances

have been calculated by multiplying the integrated absorbance by three. Synchrotron FTIR was used to study the OH distribution in the samples. Due to the high brilliance of the synchrotron beam the spatial resolution is much higher compared to a conventional light source. It was possible to obtain area maps of the OH distribution in the spectral region 2700-3800 cm^{-1} for Ge-anhB and Ge-Ringwoodite with a local resolution of $10 \times 10 \mu\text{m}$ and $12 \times 12 \mu\text{m}$, respectively.

Results

EPMA and TEM analyses

Our syntheses resulted in clear single-crystals of Ge-ringwoodite, Ge-anhB and Ge-shyB up to several 100 μm in size (Fig. 1, Table 1). EPM analyses yielded the chemical formulae $\text{Mg}_{13.89}\text{Ge}_{5.06}\text{O}_{24}$ for Ge-anhB and $\text{Mg}_{9.97}\text{Ge}_{3.01}\text{O}_{14}(\text{OH})_4$ for Ge-shyB. Results are summarized in Table 1.

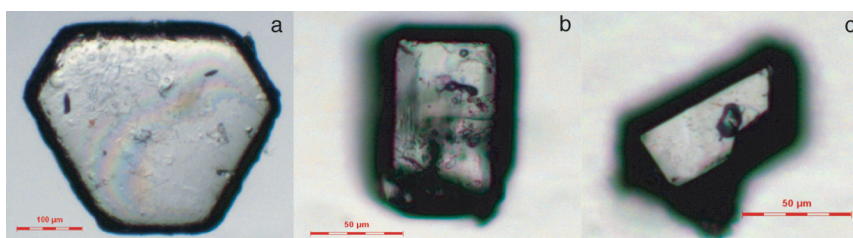


Figure 1. Images of (a) Ge-ringwoodite, (b) Ge-anhB and (c) Ge-shy B crystals synthesized in this study. Black spots reflect surface contamination.

TEM studies allowed us to check the run products for impurities. Figure 2 is the lattice fringe image of Ge-anhB, which shows no inclusions of foreign phases, and demonstrates the nearly perfect crystal structure that could be observed in all samples in this study. From the electron diffraction pattern of Ge-anhB we were able to determine the crystal orientation (Fig. 2) and used this information for the collection of polarized single-crystal IR spectra.

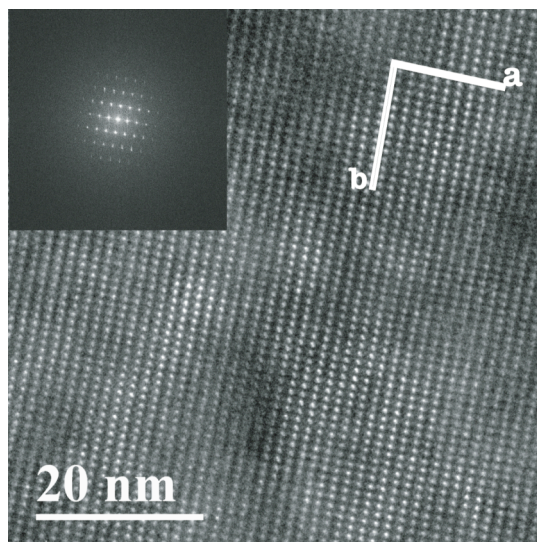


Figure 2. High-resolution transmission electron microscopy image and corresponding electron diffraction pattern of Ge-anhB. Lattice fringes reveal the homogeneous nature of the sample.

X-ray diffraction

Ge-Ringwoodite. Given that there was some controversy about the cation distribution in Ge-ringwoodite in the early 1960's, the crystal structure was refined by von Dreele et al. (1977) using powder neutron diffraction. The space group was confirmed as $Fd\bar{3}m$ with no detectable disorder on the cation sites. Hence, Ge-ringwoodite, isostructural with $\gamma\text{-Mg}_2\text{SiO}_4$, has a true spinel structure. Each oxygen atom is bonded to one Ge and three Mg atoms. The structure consists of two alternately stacked layers, OT (MgO_6 octahedra and GeO_4 tetrahedra) and O (MgO_6 octahedra). The results of the single-crystal X-ray refinement for Ge-ringwoodite of this study are shown in Table 2. Unfortunately, no indication for site occupation of hydrogen can be extracted from the structure refinement. Atomic coordinates, equivalent isotropic and anisotropic displacement parameters, selected bond distances and angles are available as deposit items (Tables D1-D3) on the MSA website at <http://www.minsocam.org>.

Table 2. Crystal structure data and statistic parameters for Ge-ringwoodite and Ge-anhB at room temperature from single-crystal refinements. Numbers in parantheses give 2σ standard deviation in terms of the preceding figure.

| | Ge-ringwoodite | | Ge-anhB | |
|--------------------------------------|--|---------------------|--|---------------------|
| Empirical formula | $\gamma\text{-Mg}_2\text{GeO}_4$ | | $\text{Mg}_{14}\text{Ge}_5\text{O}_{24}$ | |
| Temperature | 293(2) K | | 293(2) K | |
| Wavelength | 0.71069 Å | | 0.71069 Å | |
| Crystal system | cubic | | orthorhombic | |
| Space group | $\text{Fd } \overline{3} m$ | | $Pbam$ | |
| Unit cell dimensions | $a = 8.246(2) \text{ Å}$ | $\alpha = 90^\circ$ | $a = 14.52(2) \text{ Å}$ | $\alpha = 90^\circ$ |
| | $b = 8.246(2) \text{ Å}$ | $\beta = 90^\circ$ | $b = 10.231(16) \text{ Å}$ | $\beta = 90^\circ$ |
| | $c = 8.246(2) \text{ Å}$ | $\gamma = 90^\circ$ | $c = 5.947(8) \text{ Å}$ | $\gamma = 90^\circ$ |
| Volume | $560.7(6) \text{ Å}^3$ | | $884(2) \text{ Å}^3$ | |
| Z | 8 | | 2 | |
| Density (calculated) | 4.388 Mg/m^3 | | 4.095 Mg/m^3 | |
| Absorption coefficient | 11.186 mm^{-1} | | 9.053 mm^{-1} | |
| Theta range for data collection | 4.28 to 28.55° | | 2.43 to 29.27° | |
| Index ranges | $-11 \leq h \leq 11$, $-10 \leq k \leq 11$, $-11 \leq l \leq 11$ | | $-19 \leq h \leq 19$, $-14 \leq k \leq 14$, $-8 \leq l \leq 8$ | |
| Reflections collected | 1189 | | 7977 | |
| Independent reflections | 50 [R(int) = 0.0629] | | 1307 [R(int) = 0.0521] | |
| Refinement method | Full-matrix least-squares on F^2 | | Full-matrix least-squares on F^2 | |
| Data / restraints / parameters | 50 / 0 / 8 | | 1307 / 0 / 125 | |
| Goodness-of-fit on F^2 | 1.442 | | 1.185 | |
| Final R indices [I > 2 σ (I)] | R1 = 0.0397, wR2 = 0.1436 | | R1 = 0.0354, wR2 = 0.0669 | |
| R indices (all data) | R1 = 0.0401, wR2 = 0.1457 | | R1 = 0.0516, wR2 = 0.0710 | |
| Extinction coefficient | 0.07(2) | | 0.0008(4) | |

Ge-anhydrous phase B and Ge-superhydrous phase B. The crystal structures of the members of the phase B series are closely related (Finger et al. 1991). They consist of an ordered intergrowth of three layers, double OT layers (MgO_6 octahedra and TO_4 tetrahedra) alternate along the crystallographic b-axis with O layers (MgO_6 and TO_6). The members of the phase B series all contain both tetrahedral and octahedral coordinated silicon atoms, which in turn are strictly segregated into distinct structural elements (Pacalo and Parise 1992). Finger et al. (1991) demonstrated that the structure of anhB is in space group Pmcb .

The diffraction symmetry of the crystal investigated in this study was consistent with Laue group mmm. An analysis of the systematic absences indicated the diffraction symbol mmmPba-. The structure could be solved in the centrosymmetric space group Pbam (Table 2) using the program SIR97 (Altomare et al. 1999). Least-squares refinements were performed with the program SHELXL-97 (Sheldrick 1997). Neutral atomic scattering factors and anomalous-dispersion corrections were taken from the International Tables for X-ray crystallography (Ibers and Hamilton 1974). Final calculations using anisotropic displacement parameters for all atoms converged at $R1 = 0.0354$. The largest shift in the last cycle for these refinements was < 0.001 . The atomic positions obtained correspond well with those reported by von Dreele et al. (1970) for Ge-anhB, so, for better comparison, all positions were re-labeled in accordance with the earlier study. However, all lattice parameters are slightly larger than those given in Finger et al. (1991) due to substitution of Si^{4+} by Ge^{4+} (Table 3). Results of the refinement are given in Table 2. The final atomic coordinates, equivalent isotropic and anisotropic displacement parameters, as well as selected bond distances and angles can be found as supplementary Tables D1 and D4-D6 on the MSA website at <http://www.minoscam.org>. Crystal structure refinements showed no significant deviation from full occupancy for the Ge sites. However, for the Mg2-Mg6 sites inclusive, an occupancy slightly less than one may indicate the possible presence of vacancies (13.88 Mg per formula unit instead of 14.00), which moreover is in conformity with the formula deduced from EPMA (Table 1). In contrast, occupancy slightly more than one was observed for the Mg1 site which could indicate the incorporation of Ge (supplementary Table D1). Difference Fourier synthesis identified as potential hydrogen position (0.2963 0.0003 0.0000), associated to O3. That would imply a vacant Ge2 site although not identified in the structure refinement.

Table 3. Lattice parameters of Si-anhB compared to Ge-anhB.

| Lattice parameters | Si-anhydrous phase B [Å] (Finger et al. 1991) | Ge-anhydrous phase B [Å] (von Dreele et al. 1970) | Ge-anhydrous phase B [Å] (this study) |
|--------------------|--|--|--|
| a | 5.868(1)* | 5.944(1) | 5.947(8) |
| b | 14.178(1) | 14.512(2) | 14.52(2) |
| c | 10.048(1) | 10.219(2) | 10.231(16) |

Notes:

* Numbers in parantheses are the estimated standard deviation in the preceding figure.

Pacalo and Parise (1992) refined the crystal structure of shyB, and assigned it to the orthorhombic centrosymmetric space group Pnnm, with H in just one general position (multiplicity 8) – consistent with the proposed formula ($Z = 2$). Koch-Müller et al. (2005) showed that shyB exists in at least two modifications: a disordered high-temperature polymorph which crystallizes in the centrosymmetric space group Pnnm, and an ordered low-temperature polymorph which crystallizes in the acentric space group Pnn2. In the low-temperature polymorph there are two different H positions (multiplicity 4) – consistent with the proposed formula ($Z = 2$) and the results from IR and Raman spectroscopy. Whereas the centrosymmetric phase exhibits one OH band (IR and Raman) and 9 lattice modes in the Raman spectra, the acentric phase reveals two OH bands (IR and Raman) and 22 lattice modes in the Raman spectra (Koch-Müller et al. 2005).

First attempts to investigate single-crystals of Ge-shyB by X-ray diffraction failed due to strong twinning of the crystals, which has also been observed for the Si-analogue (Koch-Müller et al. 2005). To resolve this problem we used X-ray powder diffraction and Rietveld refinement, and as the basis for the crystal structure refinement for Ge-shyB we took the structure data of the LT polymorph of shyB according to Koch-Müller et al. (2005), i.e., the space group Pnn2. This was justified by the presence of two OH bands in the IR spectra (see above). From the X-ray diffraction perspective the distinction between space group Pnnm and Pnn2 cannot be made from powder diffraction data. However, taking into account vibrational data of our sample (2 OH bands and 23 lattice modes), we refined the structure in analogy to the silicate equivalent, also in the space group Pnn2. Otherwise the existence of the two OH bands and the high number of lattice bands in our Raman spectra (cf. Raman section) cannot be explained. Results of the refinement are given in supplementary Tables

D7 and D8.

Raman spectroscopy

Room temperature and pressure single-phase Raman spectra of Ge-ringwoodite, Ge-anhB and Ge-shyB are given in Figure 3. A comparison of lattice vibrations of germanates studied herein, with those previously reported for the silicate equivalents is compiled in Table 4. For the germanates a significant band shift to lower frequencies (Table 4) can be noted, caused by the substitution of tetravalent silicon by tetravalent germanium.

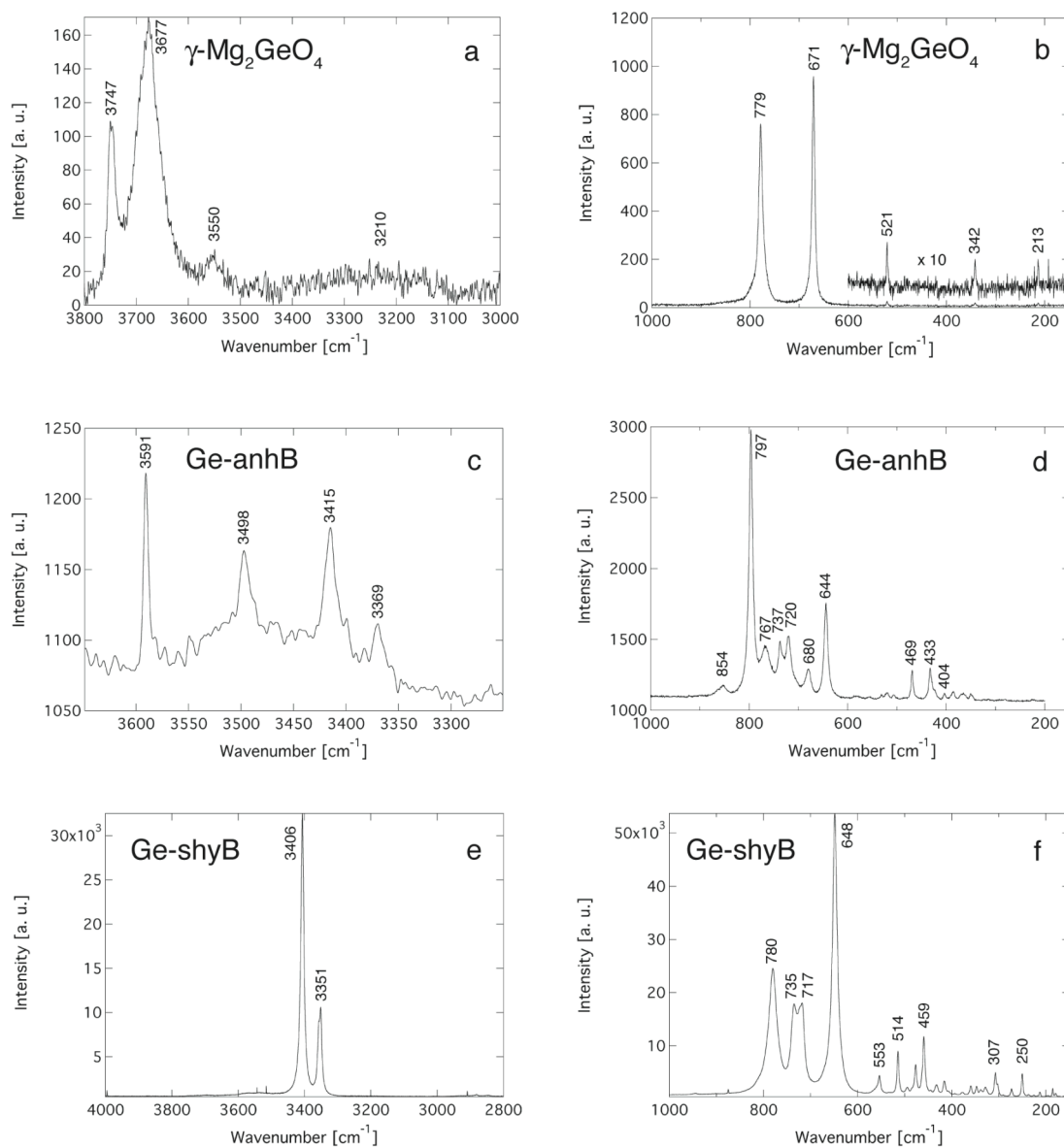


Figure 3. Single-crystal Raman spectra of γ -Mg₂GeO₄ (a, b) Ge-anhB (c,d) and Ge-shyB (e, f). (a) High-frequency range of γ -Mg₂GeO₄ showing modes caused by OH stretching vibrations. (b) The Raman spectrum of γ -Mg₂GeO₄ reveals five lattice modes. In the upper spectrum the low-energy modes are plotted at ten-times magnification. (c, d) High- and low-frequency range of Ge-anhB. (e) OH bands and (f) lattice modes of Ge-shyB.

For pure endmember γ - Mg_2SiO_4 (McMillan and Akaogi 1987; Chopelas et al. 1994) modes at 302, 372, 600, 796 and 835 cm^{-1} have been reported. From the site group analysis of γ - Mg_2SiO_4 the five Raman bands are due to antisymmetric and symmetric stretching vibrations of the isolated SiO_4 tetrahedron (Chopelas et al. 1994). However, previous studies also suggest that the lowest-frequency mode may be associated with octahedral cation motions (McMillan and Akaogi 1987; Chopelas et al. 1994). In analogy, the Raman spectrum of Ge-Ringwoodite consists of five Raman modes at 213, 342, 521, 671 and 779 cm^{-1} (Fig. 3b). These bands show excellent correspondence with those of previous workers (e.g., Ross and Navrotsky 1987). According to earlier studies the bands at 520, 669 and 777 cm^{-1} derive from bending and stretching motions of the GeO_4 tetrahedron (Jeanloz 1980; Guyot et al. 1986; Ross and Navrotsky 1987). For the two low-frequency bands no unique mode specification currently exists, however, in analogy to Si-Ringwoodite MgO_6 octahedral modes are highly probable (e.g., Ross and Navrotsky 1987).

In the OH stretching region Ge-ringwoodite reveals sharp features at 3747, 3677 and 3550 cm^{-1} and a broad band with the maximum at $\sim 3210\text{ cm}^{-1}$ which may be related to OH stretching vibrations in the crystal structure (Fig. 3a).

Raman modes attributed to lattice vibrations in Ge-anhB are shown in Figure 3d. In the high-frequency range (Fig. 3c) Raman modes caused by OH stretching vibrations at 3369, 3415, 3498 and 3591 cm^{-1} can be detected. This is surprising, as, thus far, Si-anhB has not been considered to store traces of hydrogen (e.g., Ohtani et al. 2001; Smyth 2006). Our spectrum suggests that incorporation of water in Ge-anhB is much higher than previously reported for the Si phase.

In the Raman spectrum of Ge-shyB we observe 23 lattice vibrations in the low-frequency range (Fig. 3f). In the Si analogue peaks between 645 and 730 cm^{-1} have previously been assigned to bending of Si octahedra, and bands between 800 and 1000 cm^{-1} to Si-O stretching vibrations of the SiO_4 tetrahedra (Cynn et al. 1996). The high-frequency Raman spectrum of Ge-shyB is characterized by two OH stretching vibrations at 3406 and 3351 cm^{-1}

(Fig. 3e). This is in agreement with earlier vibrational studies of the low-temperature polymorph of Si-shyB (Cynn et al. 1996; Ohtani et al. 2001; Koch-Müller et al. 2005), which exhibits OH bands at 3414 cm^{-1} and 3353 cm^{-1} .

Table 4. Raman peak positions for lattice vibrations prominent in silicates and their Ge-analogues. All frequencies are given in cm^{-1} ; “sh” indicates shoulder; “w” indicates weak.

| $\gamma\text{-Mg}_2\text{SiO}_4$ (McMillan and Akaogi 1987; Chopelas et al. 1994) | $\gamma\text{-Mg}_2\text{GeO}_4$ (Ross and Navrotsky 1987) | $\gamma\text{-Mg}_2\text{GeO}_4$ This study | Si-anhB (Ohtani et al. 2001) | Ge-anhB This study | Si-shyB (Hofmeister et al. 1999) | Si-shyB (Ohtani et al. 2001) | Ge-shyB This study |
|---|---|--|------------------------------------|-----------------------|--|------------------------------------|-----------------------|
| 835 | 777 | 779 | 1025 | 853 | 1096 | 847sh | 780 |
| 796 | 669 | 671 | 953 | 797 | 832 | 834 | 735 |
| 600 | 520 | 521 | 898 | 767 | | 755 | 717 |
| 372 | 341 | 342 | 876 | 738 | 682 | 684 | 648 |
| 302 | 213 | 213 | 846 | 730sh | 603 | 606 | 553 |
| | | | 824 | 720 | 589 | 590w | 514 |
| | | | 724 | 680 | 577 | 555 | 494 |
| | | | 687 | 530w | 534 | 537 | 477 |
| | | | 647 | 520w | 495 | 504 | 459 |
| | | | 617 | 506w | 455 | 481w | 433 |
| | | | 593 | 469 | 432 | 434 | 416 |
| | | | 523 | 432 | 405 | 406w | 377w |
| | | | 477 | 423sh | 365 | 368w | 360 |
| | | | 465 | 404 | 337 | 344 | 347 |
| | | | 443 | 386 | 329 | | 338 |
| | | | 410 | 366 | 309 | | 328 |
| | | | 393 | 349 | 288 | | 307 |
| | | | 366 | | 276 | 279 | 302sh |
| | | | 348 | | 259 | | 273 |
| | | | 336 | | | 231 | 250 |
| | | | 310 | | 222 | | 213w |
| | | | 255 | | 212 | | 186 |
| | | | 219 | | | | 171w |

Infrared spectroscopy

Ge-Ringwoodite. The unpolarized single-crystal IR spectrum of $\gamma\text{-Mg}_2\text{GeO}_4$ (Fig. 4a) at *ambient conditions* consists of several OH bands, probably due to different hydroxyl groups in the structure (cf. discussion). In the region from 3800 to 3000 cm^{-1} we observe at least 5 OH bands: four at relatively high wavenumbers 3742 , 3688 , 3650 , 3548 cm^{-1} and one much broader band at 3207 cm^{-1} . Whereas the normalized absorbances of the high-frequency

bands are more or less equal from grain to grain, those of the broad band at 3207 cm^{-1} with a full width at half maximum (FWHM) of 230 cm^{-1} are highly variable (Fig. 4). Additional weak bands are indicated by small shoulders at 3531 cm^{-1} and 3345 cm^{-1} . *Low-temperature* IR spectra down to -180°C (Fig. 4b) show that with decreasing temperature the OH band at 3742 cm^{-1} shifts 16 cm^{-1} to higher energies (3758 cm^{-1}) (Fig. 4b, supplementary Table D10) whereas the band at 3688 cm^{-1} is almost insensitive ($+3\text{ cm}^{-1}$). Bands that are obscured under ambient conditions are separated upon cooling. Additional OH bands could be observed in the spectral region around 3540 cm^{-1} . Furthermore, low-temperature spectra (Fig. 4b, Table D11) imply that the band with the center at 3207 cm^{-1} is composed of at least 2 single OH bands (3240 and 3170 cm^{-1}); a third band is indicated by a shoulder at 3345 cm^{-1} .

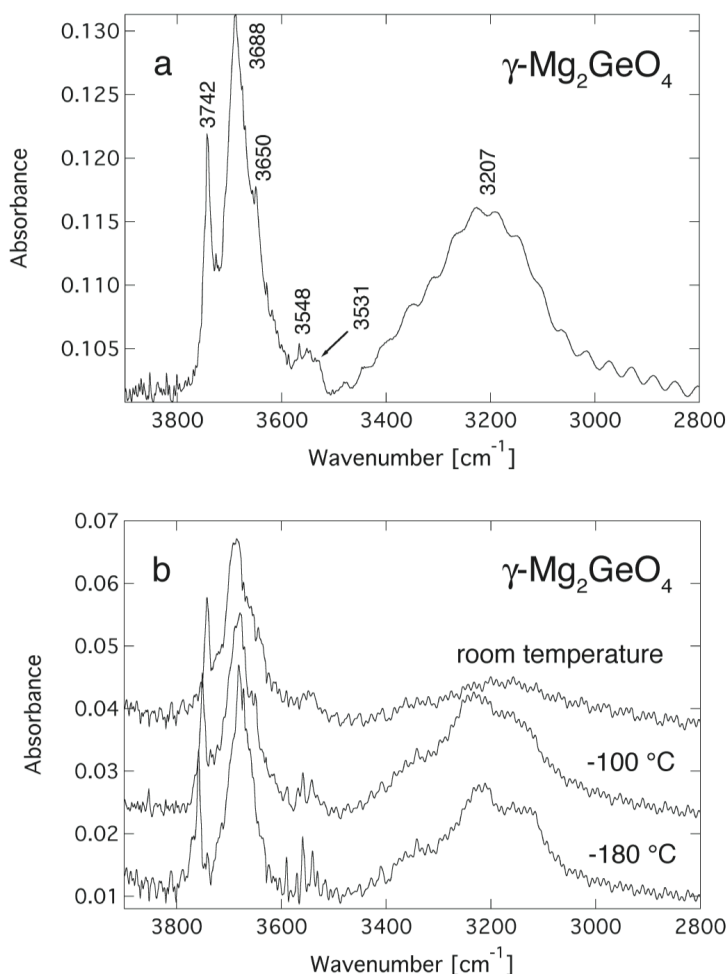


Figure 4. a) Unpolarized IR spectrum of a $53\text{ }\mu\text{m}$ thick single-crystal of Ge-ringwoodite and (b) of a $73\text{ }\mu\text{m}$ thick single-crystal, as a function of temperature. The spectra are offset for clarity.

Ge-anhydrous phase B. Single-crystal IR spectra (Fig. 5, 6) of Ge-anhB confirm the presence of OH groups in the structure. IR spectra show absorption bands due to fundamental OH stretching vibrations in the region from 3650 to 3200 cm^{-1} : ν_1 (3621 cm^{-1}), ν_2 (3592 cm^{-1}), ν_3 (3582 cm^{-1}), ν_4 (3497 cm^{-1}), ν_5 (3418 cm^{-1}), ν_6 (3368 cm^{-1}). In addition, two weak bands at 3613 cm^{-1} and 3450 cm^{-1} are observed in the spectra.

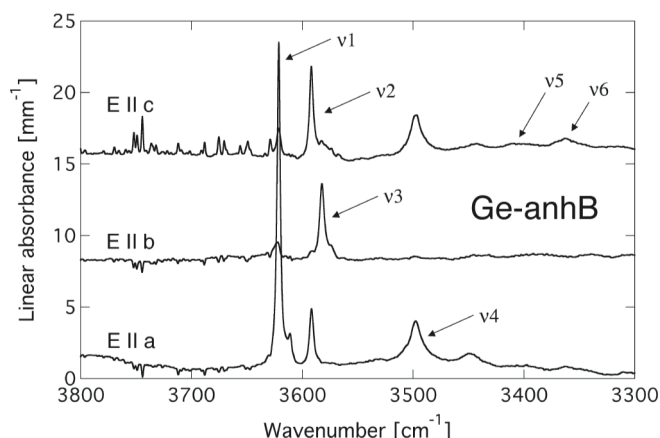


Figure 5. Polarized IR spectra of Ge-anhB recorded with synchrotron radiation with E parallel to a, b and c demonstrating the strong pleochroism of the OH bands. The spectra are offset for clarity.

All crystals studied show uniform features but with varying intensities. For the majority of the crystals the integral absorbance of the bands ν_5 and ν_6 make up $\sim 50\%$ of the observed total IR absorbance (Fig. 6, 7). However in exceptional cases those bands constitute only a minor component (Fig. 5), although the reason for this is unclear. Polarized IR spectra show a strong pleochroic behavior of the OH bands (Fig. 5), e.g., ν_1 reveals the strongest intensity with E parallel to the crystallographic a-axis. *Low-temperature* IR spectra show neither band splitting nor band sharpening, but distinctive small mode shifts (up to 4 cm^{-1}) of the bands ν_1 - ν_3 , ν_5 and ν_6 to higher energies (Fig. 6) can be observed. OH stretching band ν_4 exhibits a positive band displacement of + 11 cm^{-1} (Table D11). Upon compression all previously observed OH stretching vibrations, apart from the weak bands at 3613 cm^{-1} and 3450 cm^{-1} , are resolvable (Fig. 7). We observe a negative mode shift of all vibrations, and a slight broadening of the bands with increasing pressure (Fig. 7, supplementary Table D12). The

highest peak position displacements are displayed by ν_2 and ν_6 , with -27 cm^{-1} and -39 cm^{-1} , respectively.

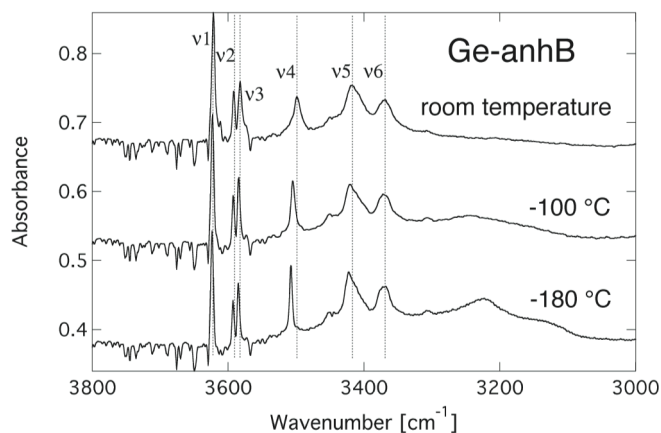


Figure 6. Unpolarized low-temperature IR spectra of Ge-anhB down to -180°C . The spectra are offset for clarity.

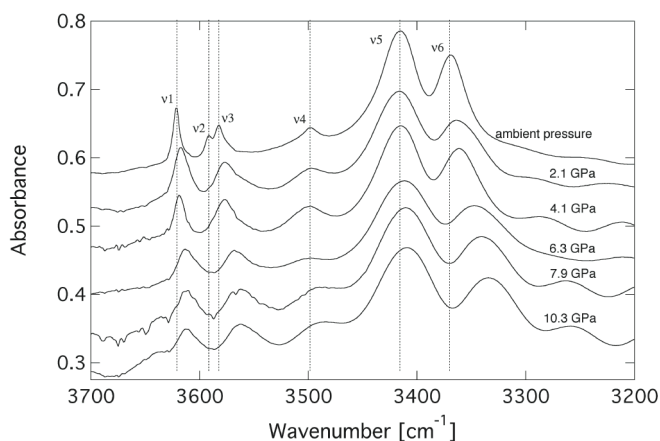


Figure 7. Pressure-dependent IR spectra of Ge-anhB determined in a DAC. The spectra are offset for clarity.

Ge-superhydrous phase B. The IR spectrum of Ge-shyB (Fig. 8) shows two OH stretching bands at 3404 cm^{-1} (ν_1) and 3353 cm^{-1} (ν_2). With increasing pressure a shift of ν_2 to lower energies (-16 cm^{-1}) and a minor increase in FWHM of $\sim 3\text{ cm}^{-1}$ can be observed in the spectra. In contrast, ν_1 position and FWHM do not change significantly with increasing pressure (Fig. 8). Both bands have been reported in previous studies for Si-shyB (Cynn et al. 1996; Koch-Müller et al. 2005).

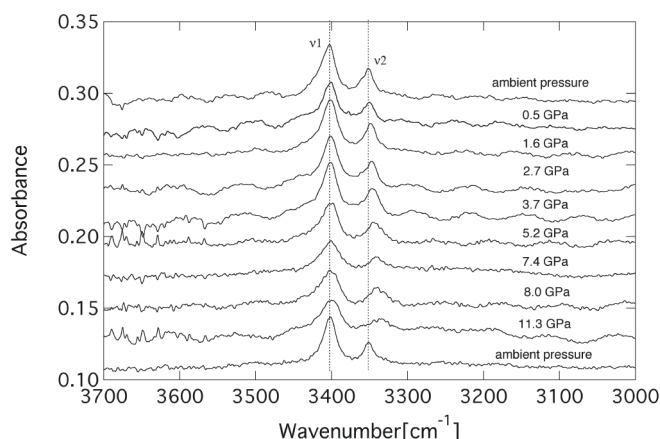


Figure 8. Pressure-dependent IR spectra of Ge-shyB recorded in a DAC. The lower ambient pressure spectrum has been recorded after pressure release. The spectra are offset for clarity.

OH distribution and quantification

Unpolarized IR maps of Ge-ringwoodite and Ge-anhB of regions of equal thickness confirm the assumption that hydroxyl groups are homogeneously distributed in the crystal structure. However, as previously mentioned the defect concentration may vary from crystal to crystal. Table 5 lists the total integrated absorbances of the hydroxyl bands obtained by fitting the unpolarized (Ge-ringwoodite) and polarized IR spectra (Ge-anhB). Water contents of Ge-ringwoodite and Ge-anhB range from 900 to 2200 wt ppm H₂O and from 2400 to 5300 wt ppm H₂O, respectively (Table 5), depending on the proportions of low-frequency OH bands in the spectra. In contrast to the above-mentioned samples Ge-shyB is a hydrous phase in which H is incorporated by stoichiometry. According to its chemical formula $\text{Mg}_{10}\text{Ge}_3\text{O}_{14}(\text{OH})_4$ it contains 4.8 wt% water. Simply taking the difference from 100 % in the microprobe analyses totals as wt% H₂O would indicate a higher amount of water (Table 1), however, higher water concentrations would require additional H positions, and there is no indication of such a deviation from stoichiometry, neither from IR-spectroscopy nor from the X-ray refinement. Moreover, the difference from 100% in microprobe analysis reflects water concentration plus total experimental error, so will be affected by other errors in the sample preparation or measurement procedure. However, despite the low total sum obtained by EPMA the chemical formula could be calculated correctly on the basis of 14 O²⁻ and 4 OH⁻.

Therefore, we assume the water content of Ge-shyB to be analogous to the Si-phase at least to the same order of magnitude.

Table 5. Estimated water contents from IR spectra of Ge-anhB and Ge-ringwoodite.

| Sample | no. of IR measurements | ϵ | Water content (wt ppm H ₂ O) | $A_{i,tot}$ (mm ⁻¹) | Density (g/cm ³) | Peak position (cm ⁻¹) |
|----------------|------------------------|------------|---|---------------------------------|------------------------------|-----------------------------------|
| | | | Libowitzky and Rossman (1997) | | | |
| Ge-anhB | 4 | 40689 | 5313 | 4918 | 4.10 | 3588* |
| | | 63130 | 2433 | 3494 | 4.10 | 3497 |
| | | 69889 | 3336 | 5304 | 4.10 | 3470 |
| | | 70557 | 3710 | 5955 | 4.10 | 3467 |
| Ge-ringwoodite | 6 | 47962 | 2049 | 2402 | 4.39 | 3559 |
| | | 82581 | 1579 | 3187 | 4.39 | 3418 |
| | | 33538 | 1727 | 1416 | 4.39 | 3617 [#] |
| | | 65433 | 1926 | 3081 | 4.39 | 3488 |
| | | 34771 | 2195 | 1866 | 4.39 | 3612 [#] |
| | | 56225 | 904 | 1242 | 4.39 | 3525 |

Notes:

* – v5 und v6 not observed in IR spectra.

† – The area-weighted average of the peak positions is used as suggested by Libowitzky and Rossman (1997). The standard deviation of the peak position resembles grain-to-grain intensity differences of the broad band at ~ 3200 cm⁻¹.

– Peak position resembles minor contributions of the broad band at ~ 3200 cm⁻¹.

Discussion

Ringwoodite

Hertweck and Ingrin (2005) report much lower water contents (5 - 10 wt ppm) for γ -Mg₂GeO₄, than those observed in this study, although those authors conducted their synthesis under similar PT-conditions. Their IR spectra are also quite different from those of this study, as they consist of only one band at 3531 cm⁻¹, with a shoulder at 3502 cm⁻¹. A possible explanation for the significant differences in the water concentration, and incorporation mechanism, between the two samples would be that the experiment by Hertweck and Ingrin (2005) was water-undersaturated. Compared to pure γ -Mg₂SiO₄, storing up to ~ 2.2 wt% H₂O (e.g., Inoue et al. 1998), Ge-ringwoodite samples synthesized at much lower pressures in this study show a much lower water concentration and different hydration mechanisms.

The main feature in the IR spectrum of pure γ -Mg₂SiO₄, synthesized at 22 GPa and 1500 °C, is a broad band (FWHM ~ 530 cm⁻¹) at 3105 cm⁻¹ (e.g., Smyth et al. 2003). However,

additional weaker bands at about 3645 cm^{-1} (Kohlstedt et al. 1996), 3668 cm^{-1} (Chamorro-Perez et al. 2006) or 3685 cm^{-1} (Kudoh et al. 2000) have been reported for hydrous magnesian ringwoodite, synthesized under lower pressures and temperatures (19 - 19.55 GPa and 1100-1300 °C).

Both, Mg- and Si-vacancies were proposed for the incorporation of hydroxyl groups in the ringwoodite structure (Kohlstedt et al. 1996; Kudoh et al. 2000; Smyth et al. 2003, 2004; Hertweck and Ingrin 2005; Blanchard et al. 2005a,b; Chamorro-Perez et al. 2006). From single-crystal X-ray studies Smyth et al. (2003) suggest the protonation of an octahedral site for pure $\gamma\text{-Mg}_2\text{SiO}_4$. However, they also state that the absorption feature at $\sim 3105\text{ cm}^{-1}$ would correlate with short O-O distances of a tetrahedral site. Kohlstedt et al. (1996) and Kudoh et al. (2000) propose a small amount of cation disorder (partial occupancy of the tetrahedral site by Mg) and protonation of both tetrahedral and octahedral sites, since they observe additional OH stretching bands at about 3645 cm^{-1} (Kohlstedt et al. 1996) and 3685 cm^{-1} (Kudoh et al. 2000), whose frequencies correlate with protonation of octahedral sites.

Blanchard et al. (2005a, b) calculated similar defect energies for $\gamma\text{-Mg}_2\text{SiO}_4$ and its low-pressure analogue $\gamma\text{-Mg}_2\text{GeO}_4$ using classical atomistic computer simulations, and thus imply that both compounds follow the same protonation trends. According to their models, the most favorable hydration mechanism for $\gamma\text{-Mg}_2\text{SiO}_4$ is associated with tetrahedral vacancies, namely the hydrogarnet substitution. However, in a more recent recalculation of their data (Blanchard and Wright 2006), applying density functional theory, and in consideration of mantle pressures, they now suggest hydroxyl groups prefer Mg vacancies, when entering the spinel structure. This is consistent with proposed protonation sites by Ross et al. (2003) located by studying the properties of the electron density distribution in $\gamma\text{-Mg}_2\text{SiO}_4$.

The spinel structure in the space group $\text{Fd}\bar{3}\text{m}$ contains only one oxygen position, which must be the bonding site for hydrogen. There are 4 O...O distances relevant in discussing the OH direction and band position. Due to the cubic symmetry we cannot determine the OH direction from polarized IR measurements, the only evidence on which to assign OH bands

to OH groups are the band positions, and the band temperatures and pressure dependences. For cubic $\gamma\text{-Mg}_2\text{SiO}_4$ the O...O distance within a tetrahedral site is 2.7137 Å. The octahedra show two different O...O distances 2.8546 and 2.9922 Å. Another very long O...O distance is a line between an oxygen atom of a Si tetrahedron and an oxygen atom of a Mg octahedron with 3.9387 Å. From the Libowitzky (1999) model it would be convincing to assign the low-energy band to vacant tetrahedral sites, and the high-energy band to a vacant octahedral site, since the O-H...O distances correlate well with the band positions. However, it has been proposed (e.g., Lager et al. 1987, 1989) that a vacant tetrahedron will expand locally with the magnitude of the expansion depending on the host. Hence, given a very large expansion, the tetrahedral edge will be longer than the octahedral edge (e.g., Lager et al. 1987, 1989). For this reason an OH band assignment to distinct sites is even more complex. Hertweck and Ingrin (2005) propose the hydrogarnet substitution for their Ge-ringwoodite, e.g., OH incorporation coupled with a vacant tetrahedral site. They propose that the band position correlates with the GeO_4 tetrahedra edge length of ~ 2.9 (1) Å. However, Hertweck and Ingrin (2005) also point out that a proton position assignment in Ge-ringwoodite is very difficult due to the fact that, unlike the silicate compound, tetrahedral and octahedral edge lengths have nearly equivalent values of ~ 2.9 Å (von Dreele et al. 1970). The IR spectra of the Ge-ringwoodite in our study indicate at least five different OH groups. The O...O distances within a tetrahedral site are 2.923 Å, within an octahedral site 2.895 Å and 2.909 Å, and the very long distance is 4.104 Å. From the relationship suggested by Libowitzky (1999) these distances are rather long, and would correlate with high-energy band positions. From the same model, the origin of the low-energy band in the Ge-analogue cannot be explained. A possible cause could be that a vacant tetrahedral Ge site is much smaller than an occupied site. However, this would be opposite to that observed for silicates (Armbruster and Gnos 2000). Another option would be to interpret this broad absorption feature as molecular water, discussed by Smyth et al. (2003, 2004) for $\gamma\text{-Mg}_2\text{SiO}_4$, but excluded by reason of a high reproducibility of the absorption signal from grain to grain and its strong correlation with unit

cell volume. In the case of Ge-ringwoodite the incorporation of molecular water would explain the low-energy of the band, and the fact that the integrated area was not highly reproducible from grain to grain. Moreover, band splitting was observed in the low-temperature IR spectra, as reported for IR spectra of ice. However, γ -Mg₂GeO₄ in this study showed no stretch-bend combination mode in the 5200 cm⁻¹ region. Moreover, contrary to the generally strong mode shifts of ~ 200 cm⁻¹ reported for the water-ice transition, in our sample only a small negative total band shift was found. Hence, we suggest that this band is due to a range of O-H...O distances rather than molecular water. The very large FWHM of the low-energy band in Si-ringwoodite spectra could be explained as statistical distribution of the protons among three possible H symmetry sites (1, m or 3m) due to the 3m-site symmetry of the oxygen atom (Kudoh et al. 2000). The latter specification would be consistent with our low-temperature spectra of γ -Mg₂GeO₄ in which the low-energy band splits into at least two bands with decreasing temperature (cf. IR section). Our data give no evidence that the broad band in Ge-ringwoodite is equivalent to the broad absorption signal found in γ -Mg₂SiO₄. For example, Bolfan-Casanova et al. (2000) observe no significant change of the appearance of the broad band upon cooling to -50 °C in Si-ringwoodite. Moreover, our broad band has a smaller FWHM of 230 cm⁻¹, and, in contrast to the silicate, is only modestly reproducible from crystal to crystal. In the γ -Mg₂GeO₄ spectra from this study the high-frequency bands are the dominant features, whereas the broad band at ~ 3100 cm⁻¹ is the main feature in γ -Mg₂SiO₄. The single band at the highest energy of 3742 cm⁻¹ has not previously been reported for γ -Mg₂SiO₄. Based on its shift to even higher frequencies upon cooling, it would be a good candidate for the very long bond distance (4.104 Å), moreover, it is indicative of a very strong OH dipole, with no hydrogen bonding. The band shift to even higher energies during cooling supports the latter suggestion, as the OH dipole gets even stronger. The band at 3688 cm⁻¹ could be due to vibration of an OH dipole occupying a vacant octahedron, pointing in the direction of the octahedral O...O distances (2.895 and/or 2.909 Å). In conclusion, compared

to $\gamma\text{-Mg}_2\text{SiO}_4$, Ge-ringwoodite synthesized in this study contains much less "water", and based on our observations, seems to incorporate "water" in a different way to the Si-analogue.

Ge-anhydrous phase B

In contrast to previous data on anhB (e.g., Ohtani et al. 2001) our spectra of its germanium equivalent reveal the presence of OH groups in the structure. We have developed a hydration model for Ge-anhB on the basis of X-ray structure refinements and polarized IR spectra on oriented crystals. We propose two OH defects, the first defect (Fig. 9a, b) based on the results of X-ray structure refinement, corresponds to the hydrogarnet substitution: a vacant GeO_4 tetrahedron where four charge-compensating protons combine with the oxygen atoms to four OH groups. These OH groups give rise to four OH stretching vibrations ν_1 , ν_2 , ν_{3a} and ν_{3b} . The difference Fourier synthesis showed a potential hydrogen position H1 close to O3 (see results), which would imply a vacant Ge2 site. In contrast to models for coesite (Koch-Müller et al. 2003) or garnet (e.g., Lager et al. 1987, 1989; Libowitzky and Beran 2006) where OH dipoles involved in these defects are located outside the tetrahedron, the O3-H1 dipole suggested here points inwards. Taking into account that a Ge tetrahedron is much larger than a Si tetrahedron, and that a vacant tetrahedron may expand locally (e.g., Lager et al. 1987, 1989), such a dipole pointing inwards does not lead to unrealistic short H...O distances. The atomic position of the potential hydrogen position from the difference map would result in an O3-H1 distance of only 0.65 Å. However, again we have to take into account that the oxygen positions are averaged over the structure, and that real oxygen positions for the vacant tetrahedron are different. The proposed final atom position for H1 (Table 6) therefore deviates slightly from the position taken from the Fourier synthesis, resulting in a more realistic O3-H1 distance of 0.918 Å. Vibrations of the proposed O3-H1 dipole give rise to the ν_1 OH band, which is in good agreement with the polarized spectra.

From the pleochroic behavior, and the positions of bands ν_2 , ν_{3a} and ν_{3b} , we propose two additional protons labeled as H2 and H3 (Figs. 9a and 9b; Table 6).

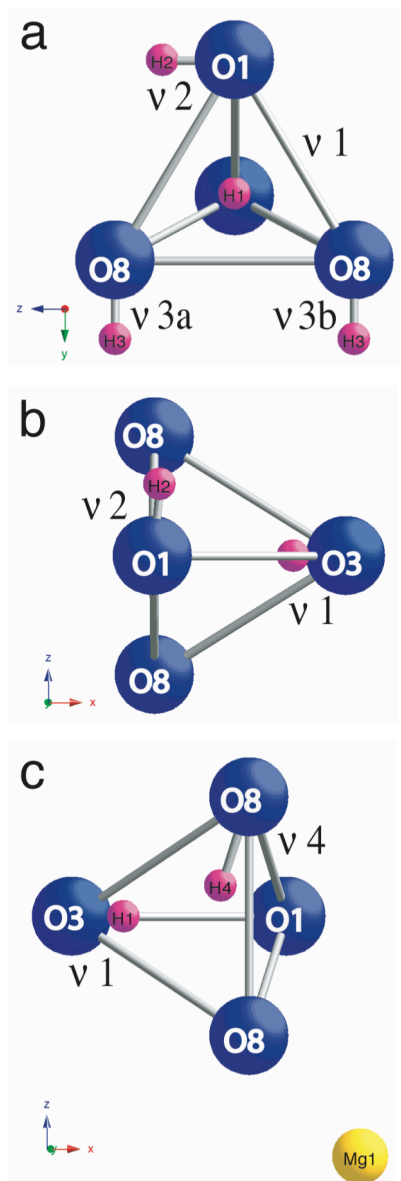


Figure 9. Projection of a vacant GeO_4 tetrahedron in Ge-anhB (a) parallel to (100) and (b) parallel to (010) showing defect 1. (c) Projection of atoms involved in defect 2 in Ge-anhB parallel to (010).

The second defect (Fig. 9c) is most probably associated with the substitution of Mg1 by Ge^{4+} , where two charge-balancing OH groups at the adjacent vacant Ge2 tetrahedron cause vibrations ν_1 and ν_4 . This assignment is based on the refined site occupancy of the Mg1 site, which is slightly larger than 1 (supplementary Table D1), indicating the incorporation of Ge. Thus, the OH bands in Ge-anhB, ν_1 , ν_2 , ν_{3a} , ν_{3b} and ν_4 can be explained by the vibration of dipoles O3-H1, O1-H2, O8-H3 and O8-H4, respectively (Figs. 5 and 7; Table 6).

The proposed H positions and associated O-H distances were estimated from the polarized IR measurements, and the observed band positions, taking into account the correlation of O-H-stretching frequencies and O-H...O distances given in Libowitzky (1999). However, note the atomic positions and associated O-H distances are only estimates, and should not be taken as absolute values. O3-H1 (ν_1) dipoles are involved in both defects, reflecting the high intensity of the associated OH band in the IR spectra, and explains the fact that only one hydrogen position was refined by X-ray diffraction.

Table 6. Structure data of the proposed protons in Ge-anhB at ambient conditions.

| Dipole corresponding OH-band | Atomic positions of protons x, y, z * | O-H distance [Å] | Band position [cm ⁻¹] | FWHM [†] [cm ⁻¹] |
|------------------------------|---------------------------------------|---|-----------------------------------|---------------------------------------|
| O3-H1 ν_1 | 0.815 0.500 0.000 | 0.918 | 3622 | 5.1 |
| O1-H2 ν_2 | 0.590 0.162 0.155 | 0.926 | 3592 | 4.4 |
| O8-H3 ν_{3a} | 0.586 0.823 0.249 | 0.980 | 3582 | 7.2 |
| O8-H3 ν_{3b} | 0.586 0.823 0.752 | 0.980 | 3582 | 7.2 |
| O8-H4 ν_4 | 0.390 0.081 0.080 | 1.063 | 3497 | 14.8 |
| <i>Notes:</i> | | | | |
| * | | – Atomic positions and therewith the calculated O-H distances are only rough estimates and should not be taken as absolute values. They match the dipole direction determined from the polarized measurements and the band position which decreases with increasing OH distance. Other atomic coordinates are given in Table D1 of supplementary online material. | | |
| † | | – FWHM calculated using peak fit software (Jandel scientific). | | |

Analyses of axial compressibilities by Crichton et al. (1999) in anhB reveal that the c-axis is most compressible, the b-axis is least compressible, and the a-axis is intermediate. The authors conclude that the compression of the a- and c-axes is controlled by edge-sharing octahedra in the O layer (MgO₆ and TO₆ octahedra), which promote the rigidity. Chains of edge-sharing octahedra in the OT layer (MgO₆ octahedra and TO₄ tetrahedra) are, in turn, responsible for the rigidity of the b-axis. Our pressure-dependent IR spectra of Ge-anhB (Fig. 7, supplementary Table D12) reveal that with increasing pressure there is a strong negative

shift for vibrations ν_2 and ν_6 , and a moderate negative shift for vibrations ν_1 , ν_3 , ν_4 and ν_5 . A strong negative shift of OH bands indicates stronger compression in the direction of the corresponding OH dipole. The dipole involved in the ν_2 vibration should point towards the ac-plane, based on the strong response upon compression and our polarized IR spectra (Figs. 5 and 7), where ν_2 shows the highest intensity parallel to the c-axis and a less intense contribution parallel to the a-axis. This is consistent with the structure model suggested herein. Agreement of pressure data and polarized IR spectra is also obtained in the case of vibrations ν_1 and ν_4 . Their moderate compressibility and polarization behavior (Fig. 5) suggests the OH dipoles point in the ac-direction, with ν_1 having a stronger a-component than ν_4 . According to the pleochroism observed for ν_3 the corresponding dipole is placed along the b-axis. Under the terms of Crichton et al. (1999) the b-axis is least compressible, which explains the intermediate response of ν_3 upon compression. The slightly higher displacement value of ν_3 compared to ν_1 and ν_4 can be explained by the fact that latter vibrations both have a component along a and c, which should lead to average total shifts. A comparison of the compressibility model with IR measurements for ν_6 is made difficult by the fact that this vibration exhibits very weak intensities in the polarized spectra.

The OH bands ν_5 and ν_6 and the weaker bands not labeled are most probably connected with Mg vacancies, since X-ray refinement indicates vacancies at the Mg2 to Mg5 sites. Applying the results of Crichton et al. (1999) vibrations ν_5 and ν_6 would point in the a/c or c direction, respectively and therefore might be coupled to MgO_6 octahedra of the O layer. A potential additional hydration site in Ge-anhB could be the O4 oxygen, as was previously proposed for anhB by Smyth (2006). This non-silicate oxygen has the lowest electrostatic potential in the structure. Combining all this information, we propose that ν_5 is most probably associated with a vacancy on the Mg5 site, and a charge-balancing proton bound to the coordinating O4 or O5 oxygen, whose O...O bond distance is 2.769 Å. Since the charge-balancing of an octahedral Mg-vacancy requires two protons, we suggest the second proton is bound to either the O4 or O8 oxygen, whose O...O bond distance is 2.81 Å, giving rise to

vibration ν_6 . The estimated hydrogen positions are in good agreement with the observed low-energy band positions of ν_5 and ν_6 . However, we suggest that to gain further understanding of structural details of Ge-anhB, and to fully explain the IR spectra more work will be required.

We note a different trend in temperature-dependent spectra. All bands but ν_4 remain more or less at the same position, while ν_4 shifts to higher wavenumbers with decreasing temperature.

In conclusion, Ge-anhydrous phase B incorporates “water” differently than its silicate equivalent. Based on our data Ge-anhB is either an unsuitable analogue material for the equivalent mantle silicate, or the ability of anhB to incorporate significant amounts of “water” has simply been overlooked in the past.

Ge-superhydrous phase B

In analogy to the Si-phase and based on its vibrational spectra Ge-shyB has been refined in the acentric space group Pnn2 (Koch-Müller et al. 2005), which is supported by the symmetry analysis of the vibrational spectra. Infrared spectra of low-temperature Si-shyB as well as Ge-shyB show the presence of two OH bands. Based on its composition this can only be explained in an acentric space group. Correspondence of Ge-shyB with the silicate equivalent is also indicated by their vibrational signatures as a function of pressure. As observed by Koch-Müller et al. (2005) both OH bands in the Si-phase are very insensitive to changes in pressure, which is quite unusual for OH bands with band positions around 3350 cm^{-1} . For example OH band ν_3 (3360 cm^{-1}) in coesite, in the same pressure range, exhibits a shift of -68 cm^{-1} . Such a behavior cannot be observed for Ge-shyB. The stretching mode ν_1 (total shift -0.6 cm^{-1}) is almost insensitive to pressure, the OH stretching mode ν_2 displays a slight negative shift (-16 cm^{-1}) as function of pressure, which is reversible upon decompression, and indicates a small pressure-induced increase of the hydrogen bonding.

The proposed atomic positions are chosen in analogy to the silicate (see supplementary Table D 8 and Koch-Müller et al. 2005).

Our data are interpreted as evidence that germanates are good low-pressure analogues for hydrous silicates with stoichiometrically incorporated water, since we observe an identical water concentrations and incorporation mechanism for Ge-superhydrous phase B. The most important implication of this study is that germanates, though conveniently applicable as analogues for hydrous magnesium silicates, do not necessarily behave as strict analogue material for hydrogen defect studies of nominally anhydrous mantle silicates, as the concentration of “water” and the incorporation mechanism of “water” in nominally anhydrous phases depend on water fugacity and also on pressure and other intrinsic defects. A second point is the surprisingly high hydroxyl solubility observed in Ge-anhB. Following our study there is a possibility that anhB is able to store a significant amount of water, if present in the Earth’s mantle as proposed by Ganguly and Frost (2006).

Acknowledgements

We thank U. Schade and M. Schmidt for help with the synchrotron measurements at Bessy II in Berlin-Adlershof, and G. Berger for help with the preparation of single-crystals. Useful comments by M. Gottschalk and W. Heinrich are gratefully appreciated. S.-M.T. would like to thank P. Davidson who kindly helped to improve the English. The suggestions and comments of two anonymous reviewers, and the editors A. Locock and E. Libowitzky significantly improved the manuscript.

References

- Akaogi, M. and Akimoto, S. (1986) Infrared spectra of high-pressure hydrous silicates in the system $\text{MgO-SiO}_2\text{-H}_2\text{O}$. *Physics and Chemistry of Minerals*, 13, 161-164.
- Altomare, A., Burla, M.C., Camalli, M., Cascarano, G.L., Giacovazzo, C., Guagliardi, A., Moliterni, A.G.G.,

- Polidori, G., and Spagna, R. (1999) A new tool for crystal structure determination and refinement. *Journal of Applied Crystallography*, 32, 115-119.
- Armbruster, T. and Gnos, E. (2000) Tetrahedral vacancies and cation ordering in low-temperature Mn-bearing vesuvianites: indication of a hydrogarnet-like substitution. *American Mineralogist*, 85, 570-577.
- Blanchard, M., Wright, K., and Gale, J.D. (2005a) Atomistic simulation of Mg_2SiO_4 and Mg_2GeO_4 spinels: a new model. *Physics and Chemistry of Minerals*, 32 (5-6), 585-593.
- Blanchard, M., Wright, K., and Gale, J.D. (2005b) A computer simulation study of OH defects in Mg_2SiO_4 and Mg_2GeO_4 spinels. *Physics and Chemistry of Minerals*, 32 (8-9), 585-593.
- Blanchard, M. and Wright, K. (2006) Defects associated with water in ringwoodite. MSA Short Course on 'Water in Nominally Anhydrous Minerals' Verbania, Italy, Abstract volume, 43.
- Bolfan-Casanova, N., Keppler, H., and Rubie, D.C. (2000) Partitioning of water between mantle phases in the system $\text{MgO-SiO}_2\text{-H}_2\text{O}$ up to 24 GPa: Implications for the distribution of water in the Earth's mantle. *Earth and Planetary Science Letters*, 182, 209-221.
- Boyd, F.R. and England, J.L. (1960) Apparatus for phase-equilibrium measurements at pressures up to 50 kbar and temperatures up to 1740 °C. *Journal of Geophysical Research*, 65, 741-748.
- Chamorro-Pérez, E.M., Daniel, I., Chervin, J.-C., Dumas, P., Bass, J.D., and Inoue, T. (2006) Synchrotron IR study of hydrous ringwoodite ($\gamma\text{-Mg}_2\text{SiO}_4$) up to 30 GPa. *Physics and Chemistry of Minerals*, 33, 502-510.
- Chopelas, A., Boehler, R., and Ko, T. (1994) Thermodynamics and behavior of $\gamma\text{-Mg}_2\text{SiO}_4$ at high pressure: Implications for Mg_2SiO_4 phase equilibrium. *Physics and Chemistry of Minerals*, 21, 351-359.
- Crichton, W.A., Ross, N.L., and Gasparik, T. (1999) Equations of state of magnesium silicates anhydrous B and superhydrous B. *Physics and Chemistry of Minerals*, 26, 570-575.
- Cynn, H., Hofmeister, A.M., Burnley, P.C., and Navrotsky, A. (1996) Thermodynamic properties and hydrogen speciation from vibrational spectra of dense hydrous magnesium silicates. *Physics and Chemistry of Minerals*, 23, 361-376.
- von Dreele, R.B., Bless, P.W., Kostiner, E., and Hughes, R.E. (1970) The crystal structure of magnesium germanate: A reformulation of Mg_4GeO_6 as $\text{Mg}_{28}\text{Ge}_{10}\text{O}_{48}$. *Journal of Solid State Chemistry*, 2, 612-618.
- von Dreele, R.B., Navrotsky, A., and Bowman, A.L. (1977) Refinement of the crystal structure of Mg_2GeO_4 spinel. *Acta Crystallographica*, B33, 2287-2288.
- Finger, L.W., Ko, J., Hazen, R.M., Gasparik, T., Hemley, R.J., Prewitt, C.T., and Weidner, D.J. (1989) Crystal chemistry of phase B and an anhydrous analogue: implications for water storage in the upper mantle. *Nature*, 341, 140-142.
- Finger, L.W., Hazen, R.M., and Prewitt, C.T. (1991) Crystal structures of $\text{Mg}_{12}\text{Si}_4\text{O}_{19}(\text{OH})_2$ (phase B) and $\text{Mg}_{14}\text{Si}_5\text{O}_{24}$ (phase AnhB). *American Mineralogist*, 76, 1-7.

- Frost, D.J. (1999) The stability of dense hydrous magnesium silicates in Earth's transition zone and lower mantle. In Y. Fei, C.M. Bertka, and B.O. Mysen, Eds., *Mantle Petrology: Field observations and high-pressure experimentation*. Geochemical Society, Special Publication No. 6, 283-295.
- Ganguly, J. and Frost, D.J. (2006) Stability of anhydrous phase B: Experimental studies and implications for phase relations in subducting slab and the X discontinuity in the mantle. *Journal of Geophysical Research*, 111, 6, B06203.
- Gasparik, T. (1993) The role of volatiles in the transition zone. *Journal of Geophysical Research*, 98, 4287-4299.
- Guyot, F., Boyer, H., Madon, M., Velde, B. and Poirier, J.P. (1986) Comparison of the Raman microprobe spectra of $(\text{Mg,Fe})_2\text{SiO}_4$ and Mg_2GeO_4 with olivine and spinel structures. *Physics and Chemistry of Minerals*, 13, 91-95.
- Ibers, J.A. and Hamilton, W.C., Eds. (1974) *International Tables for X-ray Crystallography*, Vol. IV, Revised and Supplementary Tables, The Kynoch Press, Birmingham, UK.
- Hertweck, B. and Ingrin, J. (2005) Hydrogen incorporation in a ringwoodite analogue: Mg_2GeO_4 spinel. *Mineralogical Magazine*, 69, 337-343.
- Herzberg, C. and Gasparik, T. (1989) Melting experiments on chondrite at high pressures: Stability of anhydrous phase B. *EOS, Transactions of the American Geophysical Union*, 70, 484.
- Hofmeister, A.M., Cynn, H., Burnley, P.C., and Meade, C. (1999) Vibrational spectra of dense, hydrous magnesium silicates at high pressure: Importance of the hydrogen bond angle. *American Mineralogist*, 84, 454-464.
- Inoue, T., Weidner, D.J., Northrup, P.A., Parise, J.B. (1998) Elastic properties of hydrous ringwoodite (γ -phase) of Mg_2SiO_4 . *Earth and Planetary Science Letters*, 160, 107-113.
- Jeanloz, R. (1980) Infrared spectra of olivine polymorphs: α , β -phase and spinel. *Physics and Chemistry of Minerals*, 5, 327-339.
- Kanzaki, M. (1991) Stability of hydrous magnesium silicates in the mantle transition zone. *Physics of the Earth and Planetary Interiors*, 66, 307-312.
- Kato, T. and Kumazawa, M. (1985) Melting experiment on natural Iherzolite at 20 GPa: formation of phase B coexisting with garnet. *Geophysical Research Letters*, 13, 181-184.
- Kleppe, A.K., Jephcoat, A.P., and Smyth, J.R. (2002) Raman spectroscopic study of hydrous $\gamma\text{-Mg}_2\text{SiO}_4$ to 56.5 GPa. *Physics and Chemistry of Minerals*, 29, 473-476.
- Koch-Müller, M., Dera, P., Fei, Y., Hellwig, H., Liu, Z., Van Orman, J., and Wirth, R. (2005) Polymorphic phase transition in superhydrous phase B. *Physics and Chemistry of Minerals*, 32, 349-361.
- Kohlstedt, D.L., Keppler, H., and Rubie, D.C. (1996) The solubility of water in α , β and γ phases of $(\text{Mg,Fe})_2\text{SiO}_4$. *Contributions to Mineralogy and Petrology*, 123, 345-357.

- Kohn, S.C., Brooker, R.A., Frost, D.J., Slesinger, A.E., and Wood, B.J. (2002) Ordering of hydroxyl defects in hydrous wadsleyite (β - Mg_2SiO_4). *American Mineralogist*, 87, 293-301.
- Kudoh, Y., Kuribayashi, T., Mizohata, H., and Ohtani, E. (2000) Structure and cation disorder of hydrous ringwoodite, γ - $\text{Mg}_{1.89}\text{Si}_{0.97}\text{H}_{0.34}\text{O}_4$. *Physics and Chemistry of Minerals*, 27, 474-479.
- Lager, G.A., Armbruster, T., and Faber, J. (1987) Neutron and X-ray diffraction study of hydrogarnet $\text{Ca}_3\text{Al}_2(\text{O}_4\text{H}_4)_3$. *American Mineralogist*, 72, 758-767.
- Lager, G.A., Armbruster, T., Rotella, F.J., and Rossman, G.R. (1989) OH substitution in garnets: X-ray and neutron diffraction, infrared, and geometric-modeling studies. *American Mineralogist*, 74, 840-851.
- Larson, A.C. and von Dreele, R.B. (1987) Generalized structure analysis system. Los Alamos National Laboratory Report, No. LA-UR-86-748.
- Libowitzky, E. (1999) Correlation of O-H stretching frequencies and O-H...O hydrogen bond lengths in minerals. *Monatshefte für Chemie*, 130, 1047-1059.
- Libowitzky, E. and Beran, A. (2006) The structure of hydrous species in nominally anhydrous minerals: Information from polarized IR spectroscopy. In H. Keppler and J.R. Smyth, Eds., *Water in nominally anhydrous minerals. Reviews in Mineralogy and Geochemistry*, 62, 29-52, Mineralogical Society of America, Chantilly.
- Libowitzky, E. and Rossman, G.R. (1997) An IR absorption calibration for water in minerals. *American Mineralogist*, 82, 1111-1115.
- Luth, R.W. (1993) Melting in the Mg_2SiO_4 - H_2O system at 3 to 12 GPa. *Geophysical Research Letters*, 20, 233-235.
- Mao, H.K., Xu, J., and Bell, P.M. (1986) Calibration of the ruby pressure gauge to 800 kbar under quasi-hydrostatic conditions. *Journal of Geophysical Research*, 91, 4673-4676.
- Mao, H.K. and Hemley, R.J. (1998) New windows on the Earth's deep interior. In R.J. Hemley, Ed., *Ultrahigh-Pressure Mineralogy. Review in Mineralogy* 37: 1-32.
- McMillan, P. and Akaogi, M. (1987) Raman spectra of β - Mg_2SiO_4 (modified spinel) and γ - Mg_2SiO_4 (spinel). *American Mineralogist*, 72, 361-364.
- Ohtani, E., Toma, M., Litasov, K., Kubo, T., and Suzuki, A. (2001) Stability of dense hydrous magnesium silicate phases and water storage capacity in the transition zone and lower mantle. *Physics of the Earth and Planetary Interiors*, 124, 105-117.
- Pacalo, R.E.G. and Parise, J.B. (1992) Crystal structure of superhydrous B, a hydrous magnesium silicate synthesized at 1400 °C and 20 GPa. *American Mineralogist*, 77, 681-684.
- Ringwood, A.E. (1975) *Composition and petrology of the earth's mantle*. 618 p. McGraw-Hill, New York.
- Ringwood, A.E. and Major, A. (1967) High-pressure reconnaissance investigations in the system Mg_2SiO_4 - MgO - H_2O . *Earth and Planetary Science Letters*, 2, 130-133.

Ross, N.L. and Navrotsky, A. (1987) The Mg_2GeO_4 Olivine-Spinel Phase Transition. *Physics and Chemistry of Minerals*, 14, 473-481.

Ross, N.L., Gibbs, G.V. and Rosso, K.M. (2003): Potential docking sites and positions of hydrogen in high-pressure silicates. *American Mineralogist*, 88, 1452-1459.

Sheldrick, G.M. (1997) SHELXL-97, Programs for crystal structure analysis. University of Goettingen, Germany, Release 97-2.

Silver, P.G., Beck, S.L., Wallace, T.C., Meade, C., Myers, S.C., James, D.E., and Kuhnel, R. (1995) Rupture characteristics of the deep Bolivian earthquake of 9 June 1994 and the mechanism of deep-focus earthquakes. *Science*, 268, 69-73.

Smyth, J.R. (1987) $\beta\text{-Mg}_2\text{SiO}_4$: a potential host for water in the mantle? *American Mineralogist*, 72, 1051-1055.

Smyth, J.R., Kawamoto, T., Jacobsen, S.D., Swope, R.J., Hervig, R.L., and Holloway, J.R. (1997) Crystal structure of monoclinic hydrous wadsleyite [$\beta\text{-(Mg,Fe)}_2\text{SiO}_4$]. *American Mineralogist*, 82, 270-275.

Smyth, J.R., Holl, C.M., Frost, D.J., Jacobsen, S.D., Langenhorst, F., and McCammon, C.A. (2003) Structural systematics of hydrous ringwoodite and water in Earth's interior. *American Mineralogist*, 88, 1402-1407.

Smyth, J.R., Holl, C.M., Frost, D.J., and Jacobsen, S.D. (2004) High pressure crystal chemistry of hydrous ringwoodite and water in the Earth's interior. *Physics of the Earth and Planetary Interiors*, 143-144, 271-278.

Smyth, J.R. (2006) Hydrogen in high-pressure silicate and oxide mineral structures. In H. Keppler and J.R. Smyth, Eds., *Water in nominally anhydrous minerals. Reviews in Mineralogy and Geochemistry*, 62, 85-115, Mineralogical Society of America, Chantilly.

Wirth, R. (2004) Focused Ion Beam (FIB): A novel technology for advanced application of micro- and nanoanalysis in geosciences and applied mineralogy. *European Journal of Mineralogy*, 16, 863-876.

X-RED (1996) Data Reduction Program, Stoe and Cie GmbH, Darmstadt, Germany.

Yamamoto, K. and Akimoto, S. (1974) High-pressure and high-temperature investigations in the system $\text{MgO-SiO}_2\text{-H}_2\text{O}$. *Journal of Solid State Chemistry*, 9, 187-195.

Appendix

Table D1. Atomic coordinates ($\times 10^4$) and equivalent isotropic displacement parameters ($\text{\AA}^2 \times 10^3$) for Ge-ringwoodite and Ge-anhB. $U(\text{eq})$ is defined as one third of the trace of the orthogonalized U_{ij} tensor. Atomic positions of protons in Ge-anhB are given in Table 6.

| | x | y | z | U (eq) |
|--|---------|---------|---------|--------|
| Ge-ringwoodite | | | | |
| Ge | 1250 | 1250 | 6250 | 20(2) |
| Mg | 0 | 0 | 0 | 21(2) |
| O | 2(6) | 2(6) | 7498(6) | 22(2) |
| Ge-anhydrous phase B | | | | |
| Ge(1) | 0 | 0 | 0 | 4(1) |
| Ge(2) | 1256(1) | 5016(1) | 0 | 4(1) |
| Ge(3) | 1863(1) | 3250(1) | 5000 | 6(1) |
| Mg(1) [*] | 0 | 5000 | 5000 | 6(1) |
| Mg(2) [*] | 0 | 0 | 5000 | 5(1) |
| Mg(3) [*] | 1757(1) | 1781(2) | 0 | 6(1) |
| Mg(4) [*] | 3260(1) | 1463(2) | 5000 | 6(1) |
| Mg(5) [*] | -44(1) | 2517(1) | 2423(2) | 5(1) |
| Mg(6) [*] | 3316(1) | 4190(1) | 2461(2) | 6(1) |
| O(1) | 836(3) | 3380(4) | 0 | 6(1) |
| O(2) | 4218(3) | 3481(4) | 0 | 4(1) |
| O(3) | 2518(3) | 31(4) | 0 | 7(1) |
| O(4) | 686(3) | 3299(4) | 5000 | 5(1) |
| O(5) | 4131(3) | 3314(4) | 5000 | 7(1) |
| O(6) | 2565(3) | -220(4) | 5000 | 6(1) |
| O(7) | 756(2) | 774(3) | 2235(5) | 5(1) |
| O(8) | 4145(2) | 812(3) | 2485(5) | 5(1) |
| O(9) | 2427(2) | 2509(3) | 2723(5) | 6(1) |
| <i>Notes:</i> | | | | |
| * refined occupancies: Mg(1) 1.02(2); Mg(2) 0.99(2); Mg(3) 0.99(1); Mg(4) 0.98(1); Mg(5) 0.99(1); Mg(6) 0.99(1). | | | | |

Table D2. Bond lengths [Å] and angles [°] for Ge-Ringwoodite.

| | |
|--------------|----------|
| Ge-O(1) | 1.782(9) |
| Ge-O | 1.782(9) |
| Ge-O(2) | 1.782(9) |
| Ge-O(3) | 1.782(9) |
| Mg-O(4) | 2.063(5) |
| Mg-O | 2.063(5) |
| Mg-O(5) | 2.063(5) |
| Mg-O(6) | 2.063(5) |
| Mg-O(7) | 2.063(5) |
| Mg-O(8) | 2.063(5) |
| O(1)-Ge-O | 109.5 |
| O(1)-Ge-O(2) | 109.5 |
| O-Ge-O(2) | 109.5 |
| O(1)-Ge-O(3) | 109.5 |
| O-Ge-O(3) | 109.5 |
| O(2)-Ge-O(3) | 109.5 |
| O(4)-Mg-O | 89.9(3) |
| O(4)-Mg-O(5) | 180.0 |
| O-Mg-O(5) | 90.1(3) |
| O(4)-Mg-O(6) | 90.1(3) |
| O-Mg-O(6) | 89.9(3) |
| O(5)-Mg-O(6) | 89.9(3) |
| O(4)-Mg-O(7) | 89.9(3) |
| O-Mg-O(7) | 90.1(3) |
| O(5)-Mg-O(7) | 90.1(3) |
| O(6)-Mg-O(7) | 180.0 |
| O(4)-Mg-O(8) | 90.1(3) |
| O-Mg-O(8) | 180.0 |
| O(5)-Mg-O(8) | 89.9(3) |
| O(6)-Mg-O(8) | 90.1(3) |
| O(7)-Mg-O(8) | 89.9(3) |

Table D3. Anisotropic displacement parameters ($\text{\AA}^2 \times 10^3$) for $\gamma\text{-Mg}_2\text{GeO}_4$. The anisotropic displacement factor exponent takes the form: $-2p^2[h^2a^*2U^{11} + \dots + 2hk a^* b^* U^{12}]$.

| | U ¹¹ | U ²² | U ³³ | U ²³ | U ¹³ | U ¹² |
|----|-----------------|-----------------|-----------------|-----------------|-----------------|-----------------|
| Ge | 20(2) | 20(2) | 20(2) | 0 | 0 | 0 |
| Mg | 21(2) | 21(2) | 21(2) | -1(1) | -1(1) | -1(1) |
| O | 22(2) | 22(2) | 22(2) | -2(2) | -2(2) | 2(2) |

Table D4. Selected bond lengths [Å] for Ge-anhB.

| | | | |
|------------|----------|-------------|----------|
| Ge(1)-O(7) | 1.897(3) | Mg(3) -O(9) | 2.030(4) |
| Ge(1)-O(7) | 1.897(3) | Mg(3) -O(9) | 2.030(4) |
| Ge(1)-O(7) | 1.897(3) | Mg(3) -O(3) | 2.104(5) |
| Ge(1)-O(7) | 1.897(3) | Mg(3) -O(1) | 2.113(5) |
| Ge(1)-O(2) | 1.925(5) | Mg(3) -O(7) | 2.223(4) |
| Ge(1)-O(2) | 1.925(5) | Mg(3) -O(7) | 2.223(4) |
| Ge(2)-O(3) | 1.780(5) | Mg(4) -O(6) | 1.995(5) |
| Ge(2)-O(1) | 1.782(5) | Mg(4) -O(8) | 2.082(4) |
| Ge(2)-(8) | 1.784(3) | Mg(4) -O(8) | 2.082(4) |
| Ge(2)-(8) | 1.784(3) | Mg(4) -O(9) | 2.108(4) |
| Ge(3)-(4) | 1.710(5) | Mg(4) -O(9) | 2.108(4) |
| Ge(3)-O(9) | 1.754(3) | Mg(4) -O(5) | 2.278(5) |
| Ge(3)-O(9) | 1.754(3) | Mg(5) -O(4) | 2.028(3) |
| Ge(3)-O(6) | 1.772(5) | Mg(5) -O(2) | 2.066(4) |
| Mg(1)-O(4) | 2.006(5) | Mg(5) -O(8) | 2.077(4) |
| Mg(1)-O(4) | 2.006(5) | Mg(5) -O(1) | 2.119(4) |
| Mg(1)-O(8) | 2.114(4) | Mg(5) -O(5) | 2.123(4) |
| Mg(1)-O(8) | 2.114(4) | Mg(5) -O(7) | 2.131(4) |
| Mg(1)-O(8) | 2.114(4) | Mg(6) -O(6) | 2.069(4) |
| Mg(1)-O(8) | 2.114(4) | Mg(6) -O(3) | 2.086(4) |
| Mg(2)-O(7) | 2.130(4) | Mg(6) -O(2) | 2.094(4) |
| Mg(2)-O(7) | 2.130(4) | Mg(6) -O(7) | 2.112(4) |
| Mg(2)-O(5) | 2.138(5) | Mg(6) -O(5) | 2.117(4) |
| Mg(2)-O(5) | 2.138(5) | Mg(6) -O(9) | 2.156(4) |

Table D5. Selected angles [°] for Ge-anhB.

| | | | | | | | | | | | |
|------|-------|-------|------------|------|-------|------|------------|------|-------|------|------------|
| O(7) | Ge(1) | O(7) | 91.0(2) | O(8) | Mg(1) | O(8) | 90.08(19) | O(6) | Mg(4) | O(8) | 92.07(15) |
| O(7) | Ge(1) | O(7) | 89.0(2) | O(8) | Mg(1) | O(8) | 89.92(19) | O(8) | Mg(4) | O(8) | 91.9(2) |
| O(7) | Ge(1) | O(7) | 180.0(2) | O(4) | Mg(1) | O(8) | 87.19(13) | O(6) | Mg(4) | O(9) | 98.51(16) |
| O(7) | Ge(1) | O(2) | 90.27(14) | O(8) | Mg(1) | O(8) | 89.92(19) | O(8) | Mg(4) | O(9) | 168.10(14) |
| O(7) | Ge(1) | O(2) | 89.73(14) | O(8) | Mg(1) | O(8) | 90.08(19) | O(8) | Mg(4) | O(9) | 93.17(15) |
| O(2) | Ge(1) | O(2) | 180.0(2) | O(8) | Mg(1) | O(8) | 180.0 | O(6) | Mg(4) | O(9) | 98.51(16) |
| O(7) | Ge(1) | Mg(5) | 46.08(9) | O(7) | Mg(2) | O(7) | 180.0 | O(9) | Mg(4) | O(9) | 80.0(2) |
| O(3) | Ge(2) | O(1) | 110.5(2) | O(7) | Mg(2) | O(7) | 101.07(18) | O(6) | Mg(4) | O(5) | 176.6(2) |
| O(3) | Ge(2) | O(8) | 108.80(12) | O(7) | Mg(2) | O(7) | 78.93(18) | O(8) | Mg(4) | O(5) | 85.59(14) |
| O(1) | Ge(2) | O(8) | 108.48(13) | O(7) | Mg(2) | O(7) | 180.00(12) | O(9) | Mg(4) | O(5) | 84.06(15) |
| O(8) | Ge(2) | O(8) | 111.8(2) | O(7) | Mg(2) | O(5) | 90.25(12) | O(4) | Mg(5) | O(2) | 173.36(16) |
| O(4) | Ge(3) | O(9) | 118.60(13) | O(7) | Mg(2) | O(5) | 89.75(12) | O(4) | Mg(5) | O(8) | 87.63(17) |
| O(9) | Ge(3) | O(9) | 101.0(2) | O(5) | Mg(2) | O(5) | 180.0 | O(2) | Mg(5) | O(8) | 97.17(17) |
| O(4) | Ge(3) | O(6) | 116.3(2) | O(9) | Mg(3) | O(9) | 105.8(2) | O(4) | Mg(5) | O(1) | 91.96(16) |
| O(9) | Ge(3) | O(6) | 99.40(14) | O(9) | Mg(3) | O(3) | 93.48(14) | O(2) | Mg(5) | O(1) | 92.56(16) |
| O(4) | Mg(1) | O(4) | 180.0 | O(9) | Mg(3) | O(1) | 91.10(14) | O(8) | Mg(5) | O(1) | 90.64(17) |
| O(4) | Mg(1) | O(8) | 87.19(13) | O(3) | Mg(3) | O(1) | 172.40(19) | O(4) | Mg(5) | O(5) | 84.71(16) |
| O(4) | Mg(1) | O(8) | 92.81(13) | O(9) | Mg(3) | O(7) | 163.74(13) | O(2) | Mg(5) | O(5) | 90.71(15) |
| O(4) | Mg(1) | O(8) | 87.19(13) | O(9) | Mg(3) | O(7) | 90.36(15) | O(8) | Mg(5) | O(5) | 89.81(17) |
| O(8) | Mg(1) | O(8) | 180.00(13) | O(3) | Mg(3) | O(7) | 87.07(16) | O(1) | Mg(5) | O(5) | 176.62(13) |
| O(4) | Mg(1) | O(8) | 92.81(13) | O(1) | Mg(3) | O(7) | 86.84(16) | O(4) | Mg(5) | O(7) | 94.86(17) |
| O(7) | Mg(3) | O(7) | 73.43(19) | O(9) | Mg(3) | O(7) | 90.36(15) | O(2) | Mg(5) | O(7) | 80.36(16) |
| O(9) | Mg(4) | O(5) | 84.06(15) | O(3) | Mg(6) | O(9) | 91.84(17) | O(8) | Mg(5) | O(7) | 177.50(13) |
| O(7) | Mg(6) | O(5) | 90.77(17) | O(2) | Mg(6) | O(9) | 98.57(16) | O(1) | Mg(5) | O(7) | 89.09(17) |
| O(6) | Mg(6) | O(9) | 79.06(16) | O(3) | Mg(6) | O(7) | 90.52(17) | O(5) | Mg(5) | O(7) | 90.60(17) |
| O(3) | Mg(6) | O(5) | 178.47(16) | O(2) | Mg(6) | O(7) | 79.74(16) | O(6) | Mg(6) | O(3) | 91.87(16) |
| O(2) | Mg(6) | O(5) | 90.13(15) | O(6) | Mg(6) | O(5) | 87.06(16) | O(6) | Mg(6) | O(2) | 176.41(16) |

Table D6. Anisotropic displacement parameters ($\text{\AA}^2 \times 10^3$) for Ge-anhB. The anisotropic displacement factor exponent takes the form: $-2p^2[h^2a^{*2}U^{11} + \dots + 2hk a^* b^* U^{12}]$.

| | U ¹¹ | U ²² | U ³³ | U ²³ | U ¹³ | U ¹² |
|-------|-----------------|-----------------|-----------------|-----------------|-----------------|-----------------|
| Ge(1) | 5(1) | 3(1) | 5(1) | 0 | 0 | 0(1) |
| Ge(2) | 4(1) | 4(1) | 5(1) | 0 | 0 | 0(1) |
| Ge(3) | 6(1) | 6(1) | 6(1) | 0 | 0 | 1(1) |
| Mg(1) | 9(1) | 3(1) | 6(1) | 0 | 0 | 2(1) |
| Mg(2) | 6(2) | 7(1) | 3(1) | 0 | 0 | 1(1) |
| Mg(3) | 5(1) | 6(1) | 7(1) | 0 | 0 | -1(1) |
| Mg(4) | 5(1) | 4(1) | 8(1) | 0 | 0 | 1(1) |
| Mg(5) | 6(1) | 5(1) | 4(1) | 0(1) | 0(1) | 0(1) |
| Mg(6) | 5(1) | 7(1) | 6(1) | 1(1) | 1(1) | 0(1) |
| O(1) | 9(2) | 4(2) | 6(2) | 0 | 0 | -1(1) |
| O(2) | 5(2) | 3(2) | 5(2) | 0 | 0 | -1(1) |
| O(3) | 9(2) | 5(2) | 7(2) | 0 | 0 | 1(2) |
| O(4) | 5(2) | 5(2) | 5(2) | 0 | 0 | -2(1) |
| O(5) | 5(2) | 8(2) | 9(2) | 0 | 0 | 0(2) |
| O(6) | 5(2) | 5(2) | 9(2) | 0 | 0 | -1(1) |
| O(7) | 6(1) | 5(1) | 4(1) | 1(1) | -1(1) | 0(1) |
| O(8) | 6(1) | 7(1) | 3(1) | -3(1) | -1(1) | -2(1) |
| O(9) | 6(1) | 7(1) | 6(1) | 0(1) | 1(1) | 0(1) |

Table D7. Rietveld results for Ge-shyB. Quality of refinement resembles trace amount of unidentified accessory phase.

| phase | a (2σ) [Å] | b (2σ) [Å] | c (2σ) [Å] | V (2σ) [Å ³] | Wt (2σ) fraction | W _{Rp} | Durbin-Watson | X ² |
|-----------|------------|------------|------------|--------------------------|------------------|-----------------|---------------|----------------|
| Ge-shyB | 14.202(1) | 5.1676(2) | 8.8756(4) | 651.3(1) | 0.80(0) | 0.085 | 0.749 | 2.04 |
| periclase | 4.211(1) | 4.211(1) | 4.211(1) | 74.70(2) | 0.10(1) | | | |
| brucite | 3.146(1) | 3.146(1) | 4.769(2) | 40.87(2) | 0.09(1) | | | |

Table D8. Atomic coordinates for Ge-shyB.

| | x | y | z |
|--------|----------|-----------|------------|
| Ge1 | 0.000 | 0.000 | -0.096(6) |
| Ge2 | 0.377(1) | 0.012(2) | -0.092(6) |
| H1 | 0.300 | 0.600 | 0.100 |
| H2 | 0.270 | 0.180 | 0.310 |
| Mg(1) | 0.174(2) | 0.332(4) | -0.086(6) |
| Mg(2A) | 0.174(3) | 0.862(9) | 0.086(6) |
| Mg(2B) | 0.323(3) | 0.334(9) | 0.234(6) |
| Mg(3A) | 0.000 | 0.500 | 0.732(8) |
| Mg(3B) | 0.000 | 0.500 | 0.089(8) |
| Mg(4A) | 0.000 | 0.000 | 0.567(9) |
| Mg(4B) | 0.000 | 0.000 | 0.234(9) |
| O(1) | 0.413(3) | 0.680(8) | 0.893(11) |
| O(2) | 0.085(4) | 0.685(8) | -0.113(9) |
| O(6) | 0.253(3) | 0.019(14) | -0.078(10) |
| O(3A) | 0.257(4) | 0.006(20) | 0.244(10) |
| O(3B) | 0.263(4) | 0.506(18) | 0.057(9) |
| O(4A) | 0.067(5) | 0.142(15) | 0.068(9) |
| O(4B) | 0.419(5) | 0.647(16) | 0.268(9) |
| O(5A) | 0.408(4) | 0.163(14) | 0.069(9) |
| O(5B) | 0.077(4) | 0.695(14) | 0.234(9) |

Table D9. Selected bond lengths [Å] for Ge-shyB.

| | |
|--------------|-----------|
| Ge(1)-O(4B) | 1.824(13) |
| Ge(1)-O(4A) | 1.894(13) |
| Ge(1)-O(2) | 2.031(7) |
| Ge(2)-O(5A) | 1.689(12) |
| Ge(2)-O(5B) | 1.919(12) |
| Ge(2)-O(6) | 1.780(6) |
| Ge(2)-O(1) | 1.796(7) |
| Mg(1)-O(6) | 1.971(11) |
| Mg(1)-O(3A) | 2.009(17) |
| Mg(1)-O(3B) | 1.999(15) |
| Mg(1)-O(4B) | 2.076(15) |
| Mg(2A)-O(3A) | 1.965(16) |
| Mg(2A)-O(6) | 1.994(13) |
| Mg(2A)-O(5B) | 1.965(16) |
| Mg(2B)-O(3A) | 1.959(17) |
| Mg(2B)-O(3B) | 1.991(14) |
| Mg(3B)-O(5B) | 1.980(14) |
| Mg(4A)-O(1) | 2.180(15) |
| Mg(4A)-O(5A) | 2.173(11) |
| Mg(4B)-O(5B) | 1.924(11) |
| Mg(4B)-O(4A) | 1.976(15) |
| Mg(4B)-O(1) | 2.030(14) |
| O(3A)-H(2) | 1.086(17) |
| O(3B)-H(1) | 0.811(12) |

Table D10. Band positions in the IR spectrum of Ge-ringwoodite as function of temperature.

| Temperature [°C] | Band position [cm ⁻¹] | | | | |
|--|-----------------------------------|------|------|------|------|
| 25 | 3742 | 3688 | | 3207 | |
| -100 | 3751 | 3689 | 3350 | 3240 | 3150 |
| -180 | 3758 | 3691 | 3345 | 3227 | 3138 |
| Total shift 25 to -180 [cm ⁻¹] | +16 | +3 | -5 | -13 | -12 |

Table D11. Band positions in the IR spectrum of Ge-anhB as function of pressure.

| Pressure [GPa] | Band position [cm ⁻¹] | | | | | |
|---------------------------------|-----------------------------------|------|------|------|------|------|
| | v1 | v2 | v3 | v4 | v5 | v6 |
| 0.0 | 3621 | 3592 | 3582 | 3497 | 3418 | 3371 |
| 0.3 | 3620 | 3591 | 3581 | 3497 | 3417 | 3369 |
| 2.1 | 3618 | 3583 | 3577 | 3497 | 3417 | 3359 |
| 4.1 | 3618 | 3578 | 3563 | 3497 | 3416 | 3355 |
| 6.3 | 3614 | 3569 | | 3498 | 3411 | 3345 |
| 7.9 | 3612 | 3568 | | 3490 | 3411 | 3339 |
| 10.3 | 3612 | 3565 | | 3486 | 3411 | 3332 |
| Total shift [cm ⁻¹] | -9 | -27 | -17 | -11 | -7 | -39 |

Kapitel 2

“Application of Raman spectroscopy to quantify trace water concentrations in glasses and garnets”

Application of Raman spectroscopy to quantify trace water concentrations in glasses and garnets

Sylvia-Monique Thomas^{1,*}, Rainer Thomas¹, Paul Davidson², Patrick Reichart³, Monika Koch-Müller¹, and Günther Dollinger³

¹ GeoForschungsZentrum Potsdam, Telegrafenberg, 14473 Potsdam, Germany. Section 4.1.

* E-mail: smthomas@gfz-potsdam.de

² ARC Centre of Excellence in Ore Deposits, University of Tasmania, Hobart 7001, Australia.

³ Universität der Bundeswehr München, LRT 2, 85577 Neubiberg, Germany.

Abstract

We present a new technique for the quantification of water in glasses down to the ppm level, using confocal microRaman spectroscopy with the recently developed “Comparator Technique”. To test this method we used a suite of glasses and gemstone-quality garnets with varying chemical compositions. Water contents were independently determined with proton-proton(pp)-scattering and infrared(IR) spectroscopy. Moreover, water concentrations obtained for the garnets were compared to data of a study of Maldener et al. (2003) using nuclear reaction analysis (NRA). For each sample we recorded Raman spectra in the frequency range from 3100 to 3750 cm^{-1} and standardized them using an independently well-characterized glass. In this paper we demonstrate the usefulness of this technique for quantifying water concentrations in natural and synthetic glass samples and garnets, and verify its adaptability for concentrations from 40 wt ppm up to 40 wt % H_2O . However, in case of absorbing material (e.g., Fe-bearing samples) the suggested method needs to be modified to overcome problems due to heating and melting of those phases. Furthermore, we propose an integrated molar absorption coefficient for water in quartz glass $\epsilon_{\text{itot}} = 72000 \pm 12000 \text{ l mol}^{-1}_{\text{H}_2\text{O}} \text{ cm}^{-2}$ for quantitative IR spectroscopy, which is higher than a prior reported value of Paterson (1982) or the datum predicted by the general calibration trend determined by Libowitzky & Rossman (1997).

Keywords: Raman spectroscopy, glasses, garnet, water determination, proton-proton scattering, FTIR spectroscopy

Introduction

Confocal microRaman spectroscopy has proven useful for the accurate and rapid determination of the total water content ($\text{H}_2\text{O}_\text{T}$) of natural and synthetic glasses with widely variable compositions (Thomas 2000 and 2002; Thomas et al. 2006; Thomas and Davidson 2006 and 2007), for concentrations from 0.1 to over 40 wt%, with high precision ($< 10\%$ relative error) and high spatial resolution (about $1\ \mu\text{m}$). Using the “Comparator Technique” (see, e.g., Thomas and Davidson 2006) the water content of a sample can be determined by simple comparison with a known standard, and consequently a calibration curve is unnecessary. This method was confirmed by an independent study of Di Muro et al. (2006), in which furthermore advantages and disadvantages of external vs. internal calibrations as well as composition, reproducibility, preparation and spectra treatment issues were extensively discussed. Based on our experience, internal standardization (Thomas 2000; Chabiron et al. 2004; Zajacz et al. 2005; Behrens et al. 2006; Di Muro et al. 2006) employing normalization of the total water band ($\text{H}_2\text{O}_\text{T}$) to either the T-O-T (T: tetrahedrally coordinated cations) bending band near $500\ \text{cm}^{-1}$, or the T-O stretching band near $1000\ \text{cm}^{-1}$ is unsuitable for concentrations $< 0.1\ \text{wt}\%$ because of potential high errors due to, e.g., the strong influence of variable glass compositions, interference peaks from the embedding medium, or the host matrix, on the internal reference intensity. Using an external reference material permits an independent selection and adoption of suitable measurement conditions according to specific requirements, which is particularly important for the measurement of very small amounts of $\text{H}_2\text{O}_\text{T}$ in geological samples. Since the Raman signal in the frequency range of 2800 to $4000\ \text{cm}^{-1}$ is directly proportional to the $\text{H}_2\text{O}_\text{T}$ concentration, and the integrated intensity increases linearly with the concentration, the determination of water is dramatically simplified by adopting an external calibration combined with a well-characterized reference glass. However, until now the lower detection limit remains un-explored. The object of this paper is to verify the utility of this Raman method for the determination of water

concentrations at the ppm level, using well-characterized samples with water contents < 0.1 wt% independently quantified by NRA, pp-scattering and IR spectroscopy.

Analytical Techniques

Samples

The samples in this study were polished sections of a set of natural and synthetic silicate glasses with basaltic to rhyolitic compositions (see also Thomas and Davidson 2007), 2 synthetic quartz glasses and 4 gem-quality garnet crystals HESS1, MALI, PYRALTAN² and SPESSOR (see Maldener et al. 2003; Rhede and Wiedenbeck 2006). The garnets, prior quantified with NRA by Maldener et al. (2003), and the synthetic quartz glasses were selected to provide samples with low water contents < 1000 wt ppm. The optical isotropic nature of cubic garnet allows unpolarized spectra acquisition and a comparison with glass samples. IR line scans as well as randomly chosen spots for Raman measurements of our samples did not reveal significant heterogeneities in the sample water distribution (see Tables 1 and 2).

Raman spectroscopy

All measurements were performed using a LabRam HR800 UV-VIS spectrometer (grating: 1800 grooves/mm) equipped with a motorized XY-stage, an Olympus optical microscope and a long working distance 100x objective (LWD VIS, NA = 0.80, WD = 3.4 mm). The spectra of glasses and garnets were collected with a Peltier-cooled CCD detector. The 488-nm line of a Coherent Ar⁺ Laser Model Innova 70-3 at 300 mW was used for sample excitation (corresponding to 44 mW on the sample). To obtain well-resolved spectra for selected samples containing water concentrations at the ppm level (PYRALTAN and SPESSOR) and to detect a potential temperature dependency of recorded spectral intensities (KG) an even

² PYRALTAN, according to text in Maldener et al. 2003; corresponds to the sample PYALTAN referred to Table 1 of Maldener et al. (2003) or the article of Rhede and Wiedenbeck (2006).

higher laser power of 1000 mW was employed. For all measurements a confocal pinhole of 100 μm was used at a corresponding spectral resolution of about 1 cm^{-1} . The spectra were taken in the frequency range of 2800 to 3980 cm^{-1} . To get a whole Raman spectrum in the latter spectral range we used the multi-window accumulation mode (multi-window acquisition) of the Labspec Software. For a grating of 1800 groves/mm three spectral windows are required. The laser beam was focused on the top of the sample surface using the 100x objective and then lowered by 4 μm before starting the measurement to avoid errors due to sample surface heterogeneities. To maintain consistency, this procedure was repeated for each Raman measurement throughout this study. Before and after each sample measurement a standard spectrum, in this case of the rhyolitic SD-6.53% glass (Table 1) with 6.53 wt% water, was recorded. The integrated intensity obtained in the frequency range 3100 to 3750 cm^{-1} served as intensity reference, and to monitor the device stability (laser power). All subsequent spectra taken under the same conditions were normalized using this standard. Measuring conditions are listed in Tables 1 and 2. Spectra acquisition times varied from generally 100 seconds for glasses with > 1 wt % $\text{H}_2\text{O}_\text{T}$ to 600 s or even 1000 s for samples containing water concentrations at the ppm-level. All calculated correlation coefficients are based on intensity data standardized on counts per second (cps). We adopted a linear background correction to all our spectra in the integration interval between 3100 and 3750 cm^{-1} . For glasses with a narrow compositional range with densities $\sim 2.2 \text{ g/cm}^3$, such as analyzed throughout this study, this method has proven to be matrix-independent (Thomas and Davidson 2006). Therefore, a density correction of measured Raman intensities is unnecessary. However, since we excite a different sample mass in a constant sampling volume in the denser garnets, we corrected our integrated intensity obtained from garnet Raman spectra for density variations between reference material ($\rho_{\text{ref}} = 2.26 \text{ g/cm}^3$) and sample ($\rho_{\text{PYRALTAN}} = 3.76 \text{ g/cm}^3$, $\rho_{\text{SPESSOR}} = 4.13 \text{ g/cm}^3$, $\rho_{\text{MALI}} = 3.65 \text{ g/cm}^3$, $\rho_{\text{HESS1}} = 3.62 \text{ g/cm}^3$) prior to calculating corresponding water concentrations. Effective sampling volume in turn is a function of laser focusing, sample dimension, sample

transparency, reflections, refractions and roughness of the sample surface. Thus, given a constant focusing and the density correction applied herein, an additional reflectance correction should be considered for our garnets. According to the Snell's law and the Fresnel equations measured intensities are underestimated and should be corrected for a reflectance/refraction error of 8% for garnet that in turn is defined by the differences of refractive indices between reference material ($n_{\text{ref}} = 1.5$) and sample ($n_{\text{garnet}} = 1.8$; mean value according to Maldener et al. 2003). Moreover, we conducted up to 5 single analyses on garnet HESS1 by rotating the crystal plate by 45° with respect to the microscope axis before subsequent spectrum acquisition. This was done to account for potential dependencies of the measured intensities on the crystal orientation (Kolesov and Geiger 1997). As Raman spectroscopy measures the molar concentration of the activated species the water concentration in mol/l was calculated using following equation: $c_{\text{H}_2\text{O}}(\text{mol/l}) = I_{\text{icorr sample}} \times c_{\text{H}_2\text{O ref}}(\text{mol/l}) / I_{\text{iref}}$, where I_i are the integrated density-corrected intensities of sample and reference and c is the water concentration of the reference glass given in mol/l (8,21 mol/l). The water concentration in wt% can be recalculated using the equation $c_{\text{H}_2\text{O}}(\text{wt}\%) = c_{\text{H}_2\text{O}}(\text{mol/l}) \times 1.8 / \rho_{\text{sample}}(\text{g/cm}^3)$.

Proton-Proton-scattering

For hydrogen analysis by the pp-scattering method the scattering geometry requires thin unsupported samples and hence these were ground and polished until they had a final thickness $< 200 \mu\text{m}$ (HESS1 $172 \mu\text{m}$, PYRALTAN $155 \mu\text{m}$, KG $83 \mu\text{m}$). Samples were typically sections $3 \text{ mm} \times 4 \text{ mm}$ in size. Pp-scattering analysis was performed at the Munich tandem accelerator lab using a 13 MeV and a 25 MeV proton beam for the thin KG sample and the thicker samples, respectively. This technique enables sensitive hydrogen depth profiling, or even 3D microscopy at hydrogen concentrations < 0.1 at ppm (Reichart et al. 2004). This method is sensitive to all hydrogen atoms in the sample, and it is self-calibrating, i.e. does not need any reference standards. This is because protons from the beam hitting a

hydrogen atom in the sample give significant elastic scattering reactions where the scattering cross section (i.e., the scattering probability) is well known for the incident proton energy, and not dependent on the chemical and structural environment of the impacted hydrogen atom. The reaction products are two indistinguishable elastically scattered protons that leave the reaction point at an angle of 90° to each other. This is used to separate these reactions from all other scattering events by a fast coincidence filtering detector setup, and results in a nearly background-free energy spectrum of all detected proton pairs. The energy information of the coincidence pairs is then used to generate a depth scale for the detected hydrogen atoms, as shown, e.g., in Figure 1.

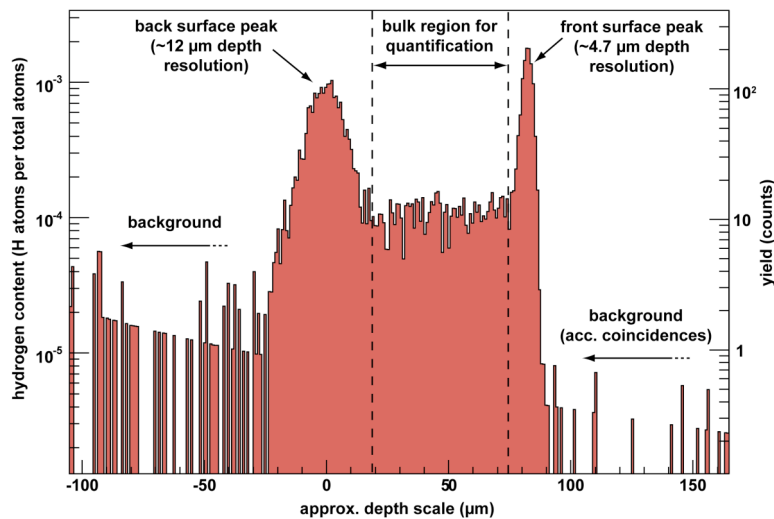


Figure 1. Depth profile of the hydrogen concentration (measured as H atoms per total atoms) in synthetic quartz glass KG derived from pp-scattering. The depth scale is approximately calculated from the energy loss of the coincident proton pairs. Note the log on the y-scale and that the background is not constant due to depth-dependent efficiency correction and background tail (to less depth). The depth resolution varies with depth as noted. Therefore the narrow surface hydrogen distribution is broadened and appears as two peaks in the front and back of the sample respectively (7.3 and 5.5×10^{16} H atoms/cm², 20% uncertainty). The spectrum demonstrates that it is possible to convincingly separate surface water from internal bulk hydrogen, and gives a background-corrected value of 83 at ppm H corresponding to 37 wt ppm H₂O.

The depth resolution depends on the depth, and ranges from about 3 % at the front of the sample, up to 10 % of the total thickness. This is sufficient to separate the surface hydrogen and identify clearly the bulk hydrogen with high sensitivity. The quantitative analysis of the (unprepared) sample surfaces gives a hydrogen surface density of more than $10^{16} - 10^{17}$ H atoms/cm². The depth resolution is not sufficient to reveal the thickness of the hydrogen

contaminated surface layer. As a rough guess, if this amount of hydrogen atoms is spreaded into say the first 10 nm of a garnet sample (8×10^{22} atoms/cm³), it gives a concentration of 10 - 100 at%, corresponding to 3-35 wt% H₂O. A garnet sample with 100 μ m thickness has an total atomic areal density of 8×10^{20} atoms/cm² and, if not separated from the bulk, the surface hydrogen would result in a hydrogen signal of 10-100 at ppm or corresponding 3-35 wt ppm H₂O. Hence the depth profiling ability is essential for hydrogen analysis of minerals at the ppm level.

The detector efficiency depends on the scattering depth, and is calibrated on samples with well-constrained hydrogen contents (Mylar, Polycarbonate, Diaspore). The thickness of the samples is verified by proton energy loss measurements, which are accurate to within a few μ m. Therefore, the measured hydrogen content within a certain thickness given in absolute units (H atoms/cm²) is converted into H atoms per total atoms using the thickness and atomic density of the samples (KG: $7.98 \cdot 10^{22}$ atoms/cm³, HESS1: $7.88 \cdot 10^{22}$ atoms/cm³, PYRALTAN: $9.01 \cdot 10^{22}$ atoms/cm³).

Due to unavailability of the SNAKE microbeam setup at that time, we used a millimeter-focused beam and a spare detector setup with two 40 mm \times 60 mm large semiconductor silicon strip detector pads (7 strips each) at scattering angles of 40°-50°, which filters for coincidence events in opposite sectors within a timing window of about 2-3 ns. The beam was averaged on an area of about 1 mm² diameter. The hydrogen content could be quantified with a hydrogen detection limit corresponding to about 0.6 wt ppm for KG and 2 wt ppm for HESS1 and PYRALTAN, that is worse than previously achieved (Reichart et al. 2004) due to the temporary spare detector setup.

IR spectroscopy

Unpolarized IR spectra of the synthetic quartz glasses KG and KOG (Korth Kristalle GmbH) and two garnet specimens PYRALTAN and HESS1 (for sample description see Maldener et al. 2003) were recorded at ambient conditions with a Bruker ISF 66v FTIR spectrometer

equipped with a Hyperion microscope, an InSb detector, a KBr beamsplitter and a global light source. The spot size used in the measurements ranged from $30 \times 30 \mu\text{m}$ to $100 \times 100 \mu\text{m}$, and up to 1024 scans were taken with a resolution of 2 cm^{-1} . Sample thickness was determined using a micrometer to be 1 mm (KG, KOG), 2 mm (PYRALTAN) and $172 \mu\text{m}$ (HESS1); errors are estimated as $\pm 5 \mu\text{m}$. The spectra were fitted using the PeakFit software by Jandel Scientific. To quantify the water concentration of the quartz glass KOG we utilized a new integrated molar absorption coefficient for quartz glass (see results and discussion), which was calculated according to the equation $\epsilon_l = (1.8 \times A_{\text{itot}}) (c_{\text{H}_2\text{Owt}\%} \times t \times \rho)$, using the water content (c) independently determined by pp-scattering, the total integrated absorbance (A_{itot}) derived from IR spectra, the thickness (t) and the density of the sample (ρ).

Results

Raman spectroscopy

To show that the method suggested by Thomas and Davidson (2007) is also applicable to concentrations down to the ppm level, we carefully measured Raman spectra of several albitic to rhyolitic glass standards and garnets relative to a well-characterized glass. In this study we used the rhyolitic SD-6.53% glass with 6.53 wt% water (Fig. 2, Table 1), determined with Karl Fischer titration (see Thomas 2000). Over several months we obtained $13652.60 \pm 527.00 \text{ cps}$ as the mean of the integrated intensity for the reference glass with the standard deviation of 3.9 % (relative error) indicating good spectral reproducibility.

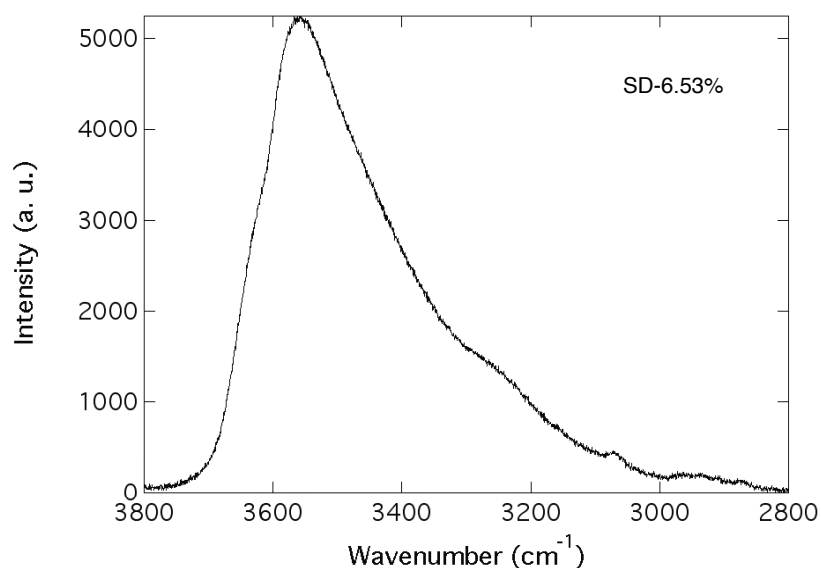


Figure 2. Raman spectrum of the rhyolitic reference glass SD-6.53% containing 6.53 wt% H₂O, previously quantified by Karl-Fischer titration (see Thomas 2000). The asymmetric OH stretching band with the peak at 3550 cm⁻¹ reflects contributions from both molecular water and OH groups (cf., e.g., Chabiron et al. 2004).

The results of our test study are listed in Tables 1 and 2 and plotted in Figure 3.

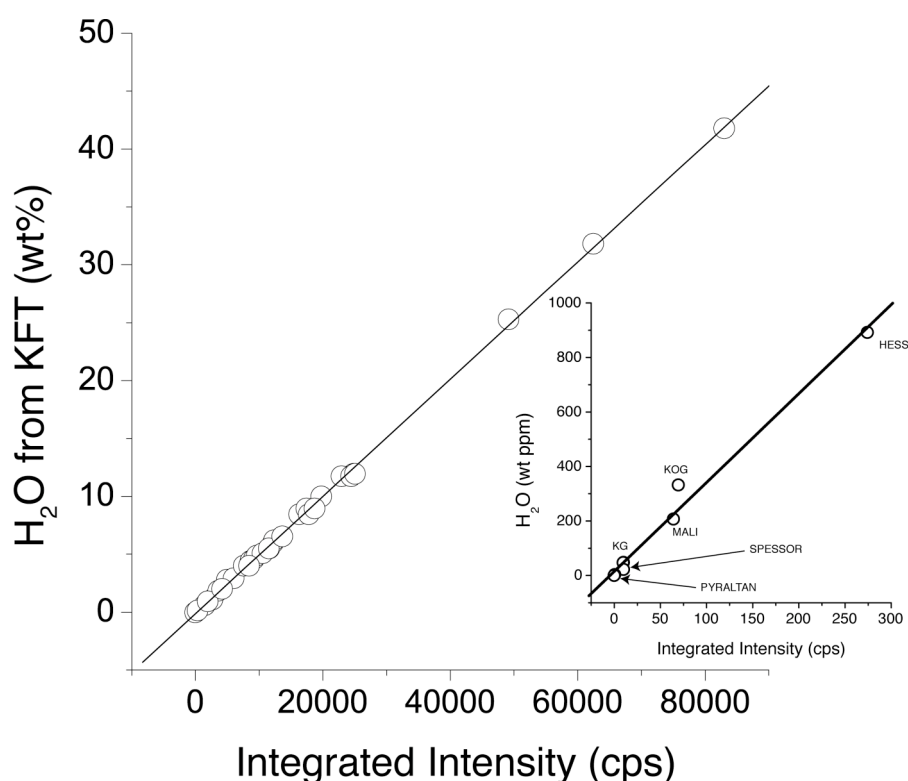


Figure 3. Correlation between the H₂O concentration in glasses and garnets, and the integrated intensity in the frequency range between 3100 and 3750 cm⁻¹, which demonstrates a linear relationship for water concentrations from 0 to 40 wt% for glasses and garnets of different compositions. Water concentrations of the samples were independently determined using Karl Fischer titration (see Thomas 2000), NRA (Maldener et al. 2003), pp-scattering or IR spectroscopy. The inset shows the correlation at the ppm level from 0 to 0.1 wt% for the samples KG, KOG, HESS1, MALI, SPESSOR and PYRALTAN (see Table 2).

Table 1. Raman spectroscopic analyses of H₂O concentrations in different synthetic glasses.

| Glass | I(cps) | 1σ | n | H ₂ O (wt ppm) | Time (s) | Accumulations | H ₂ O estimated using the SD-6.53% glass (wt ppm) [†] |
|---------------------------|---|---------------|-----------|---------------------------|------------|---------------|---|
| Westrich PCD | 355.40 | 13.80 | 5 | 1700 | 600 | 41 | 1700 ± 120 |
| Westrich 1N | 1923.50 | 122.5 | 5 | 9200 | 100 | 11 | 9200 ± 560 |
| Westrich 2N | 4223.30 | n.d. | 1 | 20200 | 50 | 6 | 20200 ± 790‡ |
| SD-4.0% | 8362.80 | 414.35 | 5 | 40000 | 100 | 6 | 40000 ± 2060 |
| SD-5.51% | 11519.80 | 806.40 | 5 | 55100 | 100 | 6 | 55100 ± 3600 |
| SD-6.53% | 13652.60 | 527.00 | 14 | 65300* | 100 | 21 | 65300 ± 2550 |
| SD-8.48% | 17729.20 | 878.40 | 5 | 84800 | 100 | 6 | 84800 ± 4360 |
| SD-8.96% | 18732.70 | 952.60 | 5 | 89600 | 100 | 6 | 89600 ± 4880 |
| SD-11.71% | 24482.20 | 1052.70 | 5 | 117100 | 100 | 6 | 117100 ± 5530 |
| SD-11.95% | 24984.00 | n.d. | 1 | 119500 | 100 | 6 | 119500 ± 4770 [‡] |
| <i>Notes:</i> | | | | | | | |
| Glass | – glasses used in this study see Thomas, 2002; Thomas et al., 2006, and Thomas and Davidson, 2007. Information on the reference glass (SD-6.53%) used to determine sample water concentrations at the ppm-level is given in bold letters. | | | | | | |
| I(cps) | – integrated intensity in the 3100-3750 cm ⁻¹ frequency range. | | | | | | |
| 1σ | – standard deviation (1 sigma). | | | | | | |
| n | – number of measurements. | | | | | | |
| H ₂ O (wt ppm) | – determined with Karl Fischer titration. | | | | | | |
| Time (s) | – Acquisition time for 1 window out of 3 in the 2800 to 3980 cm ⁻¹ frequency range. | | | | | | |
| Accumulations | – number of accumulations of each window. | | | | | | |
| n.d. | – not determined. | | | | | | |
| * | – equals 8,21 mol/l, which was used for calculating the garnet water concentrations. | | | | | | |
| † | – relative mean error using SD-6.53% glass = 3.9% and measured standard deviations listed in the 3rd column of this table. | | | | | | |
| ‡ | – error estimated using the standard deviation of the SD-6.53% glass. | | | | | | |

Table 2. Comparison of H₂O concentrations in different glasses and garnets.

| Sample | I(cps) | 1 σ | Accumulations | n | Time (s) | wt ppm H ₂ O estimated using the SD-6.53% glass | Independently determined H ₂ O (wt ppm) | | |
|-----------------------------------|--|------------|---------------|----|----------|--|--|------------------|------------------|
| | | | | | | | pp-scattering* | NRA [†] | IR ^{§§} |
| KG ^{††} | 10.00 | 1.00 | 42 | 5 | 600 | 48 ± 5 | 37 ± 8 | | |
| KG [†] | 9.74 | 0.75 | 42 | 5 | 1000 | 47 ± 4 | 37 ± 8 | | |
| KOG ^{††} | 69.40 | 3.84 | 21 | 5 | 500 | 332 ± 20 | | | 395 ± 68 |
| HESS1(garnet) ^{††} | 438.26 (274.28) | 42.31 | 6 | 5 | 100 | 892 ± 80 | 800 ± 240 | 870 ± 90 | |
| MALI(garnet) ^{††} | 103.37 (64.13) | 3.19 | 6 | 2 | 300 | 207 ± 20 | | 170 ± 20 | |
| SPESSOR (garnet) [†] | 18.33 (10.05) | n. d. | 31 | 1 | 600 | 22 [#] | | 25 ± 5 | |
| PYRALTAN (garnet) [†] | 0.76 (0.59) | 0.19 | 23 | 13 | 1000 | < 3 ^{§#} | < 2 | 17 ± 4 | |
| Notes: | | | | | | | | | |
| I(cps) | – integrated intensity in the 3100-3750 cm ⁻¹ frequency range. Data in parentheses represent density-corrected intensities used for the quantification of sample water contents. For calculation of garnet data H ₂ O contents in mol/l were used. | | | | | | | | |
| 1s | – standard deviation (1 sigma). | | | | | | | | |
| n | – number of measurements. | | | | | | | | |
| Time (s) | – acquisition time for 1 window out of 3 in the 2800 to 3980 cm ⁻¹ frequency range. | | | | | | | | |
| Accumulations | – number of accumulations of each window. | | | | | | | | |
| n.d. | – not determined. | | | | | | | | |
| * | – pp-scattering (this paper), wt ppm H ₂ O values from measured at ppm H values. | | | | | | | | |
| † | – measured at 1000 mW, I _{SD} = 17628.25 cps. | | | | | | | | |
| †† | – measured at 300 mW. | | | | | | | | |
| ‡ | – see Maldener et al. 2003. | | | | | | | | |
| § | – estimated value according to 2 sigma of calculated value. | | | | | | | | |
| §§ | – determined by IR spectroscopy using $\epsilon_{\text{H}_2\text{O}} = 72000 \pm 12000 \text{ l mol}^{-1} \text{ cm}^{-2}$, error is sd of e. | | | | | | | | |
| # | – high systematic errors > 100 % may be caused by very low signal/noise ratios of the Raman spectra. | | | | | | | | |

From a plot combining all samples ($n = 34$) given in Thomas and Davidson (2007), and the data given in Table 1, we obtain the following linear regression:

$$\text{H}_2\text{O (wt \%)} = I \times 0.00051 - 0.13577 \quad r^2 = 0.99$$

The regression value indicates a very good correlation between the total water concentration (H_2O_T) from 0 to 40 wt% for glassed with different compositions and the integrated intensity of the asymmetric OH stretching band at 3550 cm^{-1} , which reflects vibrational contributions from both, molecular water and hydroxyl groups (e.g., Chabiron et al. 2004). Hence, using one well-characterized reference glass from Table 1 should allow us to determine any unknown sample water concentration.

To test if such a method is also applicable on samples containing less than 0.1 wt % H_2O , and in order to establish the lower detection limit, we recorded Raman spectra of 2 quartz glass samples (KG, KOG) and 4 gem-quality garnet specimens (HESS1, MALI, PYRALTAN and SPESSOR) and standardized them using the SD-6.53% glass (see Table 1). Results are summarized in Table 2. Figure 4 represents unpolarized Raman spectra of the studied quartz glasses (KG and KOG) that reveal a characteristic asymmetric OH stretching band with the area-weighted average of the peak positions at 3642 and 3645 cm^{-1} , respectively. Furthermore, they demonstrate that it is possible to detect and quantify even low water concentrations $< 0.1 \text{ wt \%}$ with a high signal/noise ratio. For KG and KOG we determined a water content of 48 wt ppm and 332 wt ppm H_2O , respectively (Table 2). To study a potential temperature dependence of the recorded Raman spectra due to the employment of large beam energies in our study, the quartz glass KG was measured at 1000 mW, in addition to the generally used 300 mW laser energy. The results for KG obtained with the high beam energy show no significant difference compared to that derived at 300 mW (Table 2) and thus verify the assumption that a potential temperature dependence of our measurements is negligible.

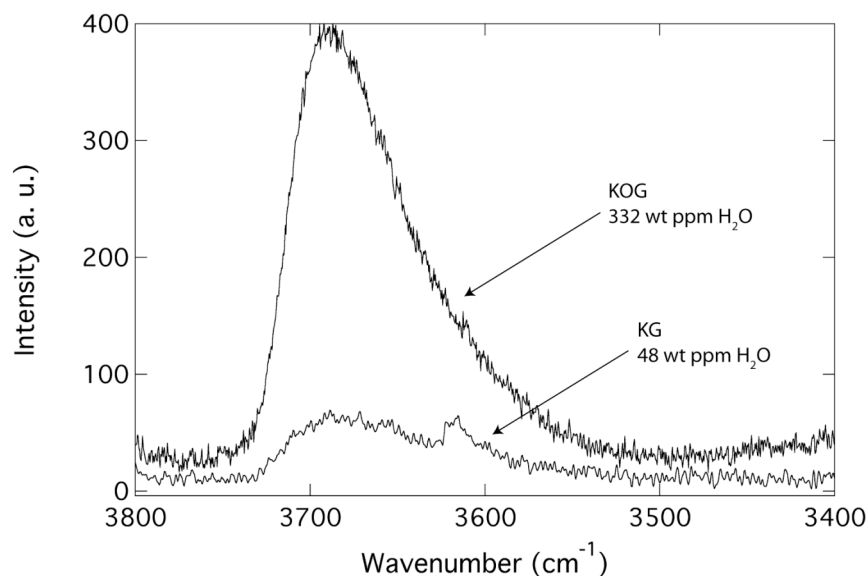


Figure 4. Raman spectra of KOG and KG recorded at 300 mW laser energy showing an asymmetric OH stretching band with the area-weighted average of the peak position at 3645 cm⁻¹ and 3642 cm⁻¹, respectively. Quantification using the integrated intensity of the band in KG resulted in a water concentration of 48 ± 5 wt ppm (c/f 37 ± 8 wt ppm H₂O obtained by pp-scattering), which demonstrates the applicability of the “Comparator Technique” to ppm-level H₂O concentrations.

In case of the garnets HESS1, MALI, SPESSOR and PYRALTAN (Table 2, Figs. 5 and 6) we calculated concentrations of 892 wt ppm, 207 wt ppm, 22 wt ppm and < 3 wt ppm H₂O, respectively. Raman measurements of the garnets SPESSOR and PYRALTAN (Fig. 6) were undertaken to explore the lower detection limit. Appropriate Raman spectra show that higher technical complexity (in this case 1000 mW laser power and 600 or 1000 s measuring time) permits determination of amounts < 40 wt ppm H₂O. The lower signal/noise ratio in the Raman spectrum of SPESSOR compared to the spectrum of PYRALTAN can be explained by the lower spectra acquisition time of the SPESSOR spectrum, and the fact that this spectrum represents only one measurement, in contrast to 13 single measurements in the case of PYRALTAN.

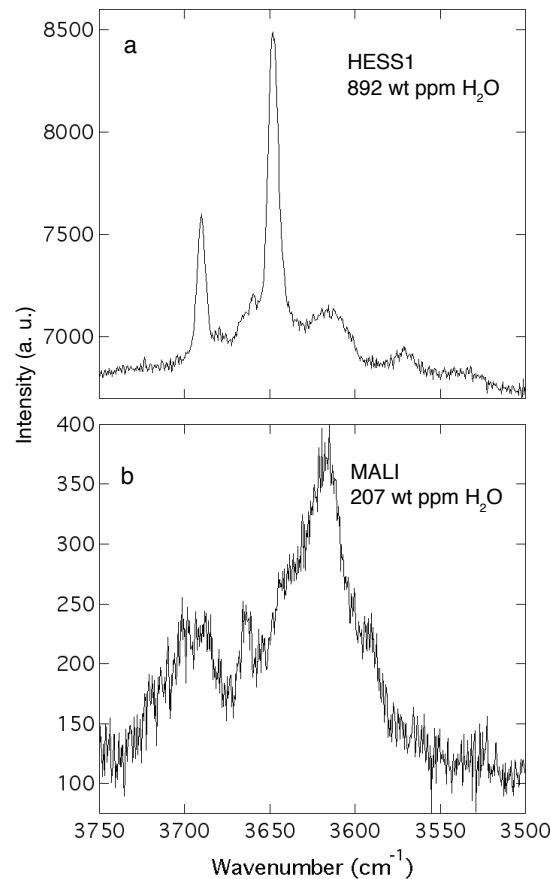


Figure 5. Raman spectra of the garnets HESS1 and MALI (corresponding IR spectrum is given in Maldener et al. 2003) showing several OH bands in the high-frequency range due to various OH defects in the crystal structure.

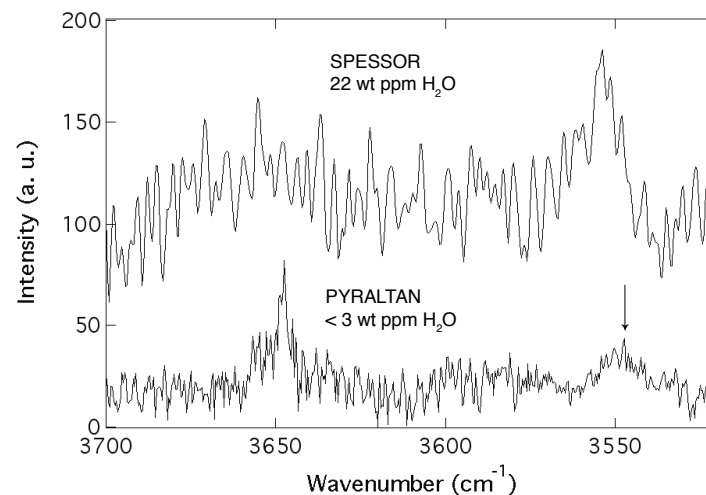


Figure 6. Raman spectrum of the garnet SPESSOR recorded at 1000 mW and 600 s acquisition time, showing OH bands in the high-frequency range due to OH defects in the crystal structure (for the corresponding IR spectrum see Maldener et al. 2003). Raman sum spectrum of the garnet PYRALTAN recorded at 1000 mW laser power and 1000 s acquisition time during 13 separate measurements. As a function of time the intensity of the OH stretching band at 3550 cm^{-1} (arrow) decreases due to local amorphization of the sample due to the very high laser power (1000 mW) and the long exposure time. In contrast the intensity of the 3650 cm^{-1} band remains constant. Due to melting and the high background noise high systematic errors ($> 100\%$) may be produced. Hence, a quantification of the water content in both garnets by our method is not recommended.

The Raman spectrum of the PYRALTAN crystal, which has a deep red color and the highest Fe-content of the garnets studied herein (cf. Maldener et al. 2003), reveals two bands at 3550 cm^{-1} and 3650 cm^{-1} (Fig. 6). As a function of time a slow decrease of the intensity of the 3550 cm^{-1} band was observed, that might be a result of local amorphization and water loss of the sample. Water loss or even sample melting may be initiated by the very high beam power (1000 mW) and the long exposure time, particularly in specimens with strong light absorption, e.g., Fe-bearing phases (e.g., Behrens et al. 2006). The estimated water concentration for PYRALTAN is $< 3\text{ ppm H}_2\text{O}$ (at 2 sigma of the calculated value) using our reference glass, and the integrated intensity of both OH bands in the Raman spectrum of the garnet. However, it should be noted that quantification of such low water contents as detected for SPESSOR and PYRALTAN is not to be recommended without further statistical enhancement, since low background/noise ratios may produce high systematic errors ($> 100\%$).

Raman spectroscopy vs. Independent quantification methods

Water concentrations derived from Raman spectroscopy (Table 2) were compared to hydrogen contents independently determined by the coincident pp-scattering method (Reichart et al. 2007), IR spectroscopy and NRA (Maldener et al. 2003). Figures 1, 7 and 8 show resulting depth profiles for KG, HESS1 and PYRALTAN derived from pp-scattering.

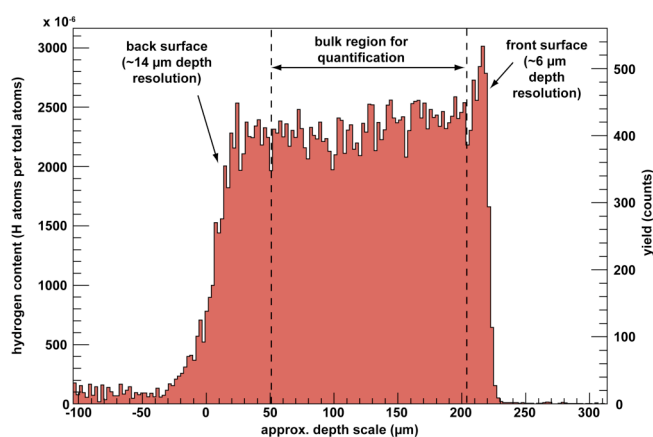


Figure 7. Depth profile of the hydrogen concentration in garnet HESS1 derived from pp-scattering. The bulk hydrogen content was derived from the marked region in order to avoid contribution from the surface, and gives a background-corrected value of (2300 ± 600) at ppm H that corresponds to (800 ± 240) wt ppm H_2O .

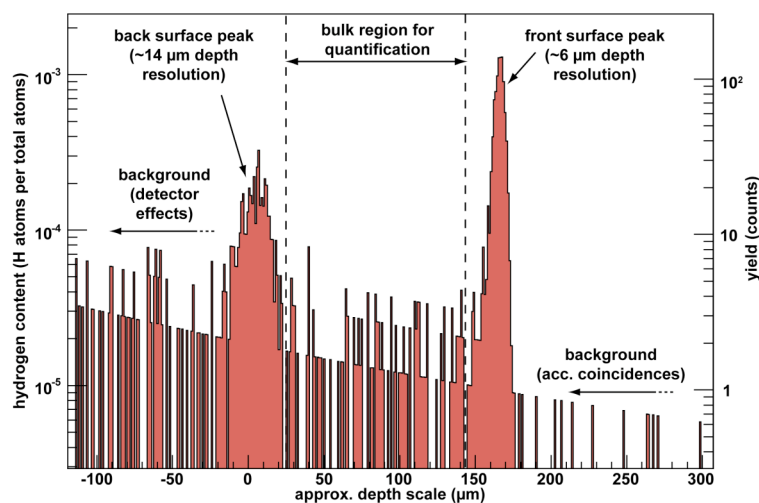


Figure 8. Depth profile of the hydrogen concentration in garnet PYRALTAN derived from pp-scattering. In the marked bulk region the background-corrected hydrogen content is in agreement with zero, with an upper limit of about 5 at ppm H that corresponds to about 2 wt ppm H₂O. The surface peaks give a content of about 6×10^{16} H atoms/cm² each and the tail of the right peak causes the main background.

Note that the surface peaks appear broader than the actual width of the hydrogen distribution (probably few nm) due to limited depth resolution. Note also the log scale for KG and PYRALTAN that emphasizes the background over the large surface peaks. The background is not constant due to depth-dependent efficiency correction, and furthermore is caused partly by accidental coincidences, and partly a surface peak tail to the left, respectively. For KG, the background-corrected analysis of the detected hydrogen events gives a bulk hydrogen content corresponding to (37 ± 8) wt ppm H₂O, assuming all detected hydrogen is bound in water and hydroxyl groups. For HESS1 we obtained (800 ± 240) wt ppm H₂O and for PYRALTAN we are able to give an upper limit of about 2 wt ppm H₂O. Corresponding unpolarized IR spectra (Fig. 9: HESS1 and PYRALTAN) show OH bands caused by different hydroxyl groups in the sample structure.

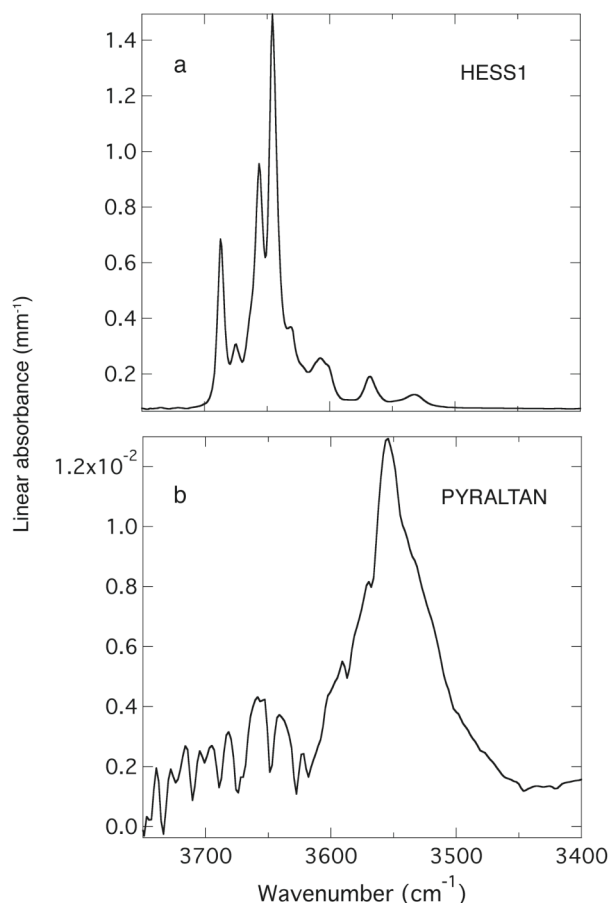


Figure 9. Unpolarized single-crystal IR spectra of the garnets HESS1 and PYRALTAN revealing several OH stretching bands at high frequencies with the area-weighted average of the peak position at 3643 cm⁻¹ and 3549 cm⁻¹, respectively (see also Maldener et al. 2003). In the lower spectrum a small contribution of an OH stretching feature is indicated around 3650 cm⁻¹ (see also Maldener et al. 2003).

IR spectra of MALI and SPESSOR are shown in Maldener et al. (2003). All recorded IR spectra are in good agreement with the obtained Raman spectra, except in the case of PYRALTAN. The IR spectrum of PYRALTAN is characterized by a broad OH band centered at 3550 cm⁻¹ and a small contribution of an OH stretching vibration around 3650 cm⁻¹ (Fig. 9). In contrast, the Raman spectrum (Fig. 6) is dominated by the 3650 cm⁻¹ band (see above), which may be caused by water loss due to the sample melting observed and would explain deviating spectra obtained with both methods.

Using a combination of integrated IR absorption intensities, with water contents independently determined by pp-scattering (KG, see Table 2) we calculated an IR molar integrated absorption coefficient for water in quartz glass $\epsilon_{\text{tot}} = 72000 \pm 12000 \text{ l mol}^{-1} \text{ cm}^{-2}$, which is higher than prior proposed values. Based on literature and own IR data Paterson

(1982) estimated for quartz glass with a narrow band peaked at $\sim 3660 \text{ cm}^{-1}$ an ϵ -value of $37600 \text{ l mol}^{-1}_{\text{H}_2\text{O}} \text{ cm}^{-2}$. The general calibration trend of Libowitzky and Rossman (1997) predicts an ϵ -value of $\sim 27000 \text{ l mol}^{-1}_{\text{H}_2\text{O}} \text{ cm}^{-2}$. By using our IR data and adopting the ϵ_{itot} determined herein for the quartz glass KOG we obtained a water concentration of 395 wt ppm H_2O (see Table 2), with the latter value in excellent agreement with the value determined from Raman spectroscopy.

Sample water contents derived from Raman spectroscopy are in very good agreement with those from independent quantification methods (see Table 2). However, the errors of the water concentrations obtained by the different techniques may be influenced by multiple factors, as errors in thickness determination (IR analyses), low statistics, errors due to polarization effects (Kolesov and Geiger 1997), vibrational spectra treatment (baseline, fits) (cf., e.g., Di Muro et al. 2006, Zajacs et al. 2005), statistical deviations within a certain sample suite or technical errors due to the quality of polarizing and analyzing material used for the spectroscopic methods. Moreover, errors may be introduced into the calculations due to the fact that the techniques compared herein as FTIR, Raman, NRA and pp-scattering probe different sample volumes. However, high surface water contaminations can be excluded from this discussion as such would be evident in FTIR analyses as broad background feature, pp-scattering clearly makes a separation of surface water and inside H contents possible, and in the Raman procedure employed herein we avoid probing the sample surface by focusing into the sample. Additional problems could be due to the fact that Karl Fischer Titration underestimates sample concentrations, as $\sim 1000 \text{ wt ppm H}_2\text{O}$ could remain unextracted in the sample investigated (Behrens 1995). However, such a value would translate into a systematical error that is well within the standard deviations in our measurements.

Discussion

The analytical method applied herein enabled us to determine very low water contents (< 40 wt ppm H_2O), which have been demonstrated on the studied quartz glasses and garnets. As verified, H_2O concentrations derived from independent methods such as pp-scattering are in good agreement with those from the Raman measurements, and thus validate the “Comparator Technique” for very low H_2O concentrations. Furthermore, our results show that in case of the garnets investigated it was sufficient to use a well-characterized glass as reference, and to adopt a density and a reflectance correction (see Analytical techniques) to account for matrix effects. This is contrary to observations of an earlier approach by Arredondo and Rossman (2002) who aimed to test the feasibility of Raman spectroscopy for trace water determination in garnets. The authors concluded that the latter technique is not generally suitable to determine trace OH concentrations in those minerals, as they could not observe a consistent correlation of OH/Si ratio with sample water concentrations. However, Arredondo and Rossman (2002) utilized an internal calibration employing the ratio of the integrated area of depolarized Raman bands in the $\sim 3600 \text{ cm}^{-1}$ stretching region to Si-O stretching bands in the $800 - 900 \text{ cm}^{-1}$ region, that may be subject of, e.g., compositional differences (cf. Introduction). Furthermore, surface heterogeneities may have influenced their results as they did not focus into their samples. Moreover, differences in detector efficiencies between the low- and the high-frequency range might have also affected intensities recorded.

The commonly used IR calibrations (Paterson 1982; Libowitzky and Rossman 1997) are not necessarily correct for low water concentrations in minerals and glasses, though they are widely used in research on water-bearing geological material (Rossman 2006). Since the calibrations have been established on different minerals and glasses the correlations may be affected by varying chemical compositions or structures. Hence, applying quantitative IR spectroscopy requires material-specific calibrations by means of an independent method, such as used in this study. Such calibrations have already been performed for garnets e.g.

by Rossman and Aines (1991), Bell et al. (1995) or Maldener et al. (2003). That the usage of material-specific integrated IR absorption coefficients is strongly recommended can be shown on the example of the KOG quartz glass measured in our study (Table 2). Using the new mineral-specific IR calibration coefficient for quartz glass from independent pp-scattering, we obtain comparable water concentrations using Raman and IR spectroscopy, whereas the use of general calibration trends (e.g., Paterson 1982; Libowitzky and Rossman 1997) would result in much higher values. This moreover confirms that not using mineral-specific integrated absorption coefficients for minerals leads to significant errors in quantification results.

This study demonstrates that the “Comparator technique” has major advantages for the determination of water over the concentration range from 40 wt ppm up to 40 wt%. The non-destructive nature, minimal sample preparation, simplicity, high precision as well as high lateral resolution makes confocal microRaman spectroscopy in combination with the “Comparator Technique” a useful tool for quantitative analysis of water concentrations in natural and synthetic glasses. In prior studies the detection limit has been estimated to be ~ 1000 wt ppm H_2O . The main issue causing that relatively high value was the presence of significant background noise producing high quantification errors. In contrast our results show that the actual detection limit is well within the range of tens of wt ppm H_2O , that can be seen in the sufficiently low background/noise ratio recorded for synthetic quartz glasses and garnets, whereby 40 wt ppm H_2O are demonstrated. However, for Fe-bearing and thus light absorbing material, e.g., Fe-rich basaltic glasses or Fe-bearing garnets, the quantification of water contents < 40 wt ppm is not possible without an increase of the statistics or a modification of the analysis procedure, as problems occur due to local heating of the sample by the high laser power. With respect to this problem, Thomas et al. (2008) show that the heating effect is cumulative and decreases after excitation. Hence, a precise determination of the water content in such glasses indeed is possible using the “Comparator Technique” and an extrapolation of the measured integral intensity to the “zero-state”. Eventually, confocal

micro Raman spectroscopy is a very convenient supplement to enhance in-house IR spectroscopic water quantification that is lacking in mineral-specific IR molar absorption coefficients. Moreover, the very high spatial resolution ($\sim 1 \mu\text{m}$) compared to IR spectroscopy ($\sim 30 \times 30 \mu\text{m}$) makes it a powerful tool for analyzing generally small sample sizes of OH-bearing nominally anhydrous high-pressure syntheses products (cf. Thomas et al. submitted).

Acknowledgements

We are grateful for constructive reviews of the editor E. Libowitzky, A. Di Muro and G. Rossman that improved the manuscript. We thank A. Hösch for providing the garnet crystals.

References

- Arredondo, E.H. and Rossman, G.R. (2002) Feasibility of determining the quantitative OH content of garnets with Raman spectroscopy. *American Mineralogist*, 87, 307-311.
- Behrens, H. (1995) Determination of water solubilities in high-viscosity melts: An experimental study on $\text{NaAlSi}_3\text{O}_8$ and KAlSi_3O_8 melts. *European Journal of Mineralogy*, 7, 905-920.
- Behrens, H., Roux, J., Neuville, D.R., and Siemann, M. (2006) Quantification of dissolved H_2O in silicate glasses using confocal microRaman spectroscopy. *Chemical Geology*, 229, 96-112.
- Bell, D.R., Ihinger, P.D., and Rossman, G.R. (1995) Quantitative analysis of trace OH in garnet and pyroxene. *American Mineralogist*, 80, 465-474.
- Chabiron, A., Pironon, J., and Massare, D. (2004) Characterization of water in synthetic rhyolitic glasses and natural melt inclusions by Raman spectroscopy. *Contributions to Mineralogy and Petrology*, 146, 485-492.
- Di Muro, A., Villemant, B., Montagnac, G., Scaillet, B., and Reynard, B. (2006) Quantification of water content and speciation in natural silicic glasses (phonolites, dacites, rhyolites) by confocal microRaman spectrometry. *Geochimica et Cosmochimica Acta*, 70, 2868-2884.
- Kolesov, B.A. and Geiger, C.A. (1997) Raman scattering in silicate garnets: an investigation of their resonance intensities. *Journal of Raman spectroscopy*, 28, 659-662.
- Libowitzky, E. and Rossman, G.R. (1997) An IR absorption calibration for water in minerals. *American Mineralogist*, 82, 1111 – 1115.

Maldener, J., Hösch, A., Langer, K., and Rauch, F. (2003) Hydrogen in some natural garnets studied by nuclear reaction analysis and vibrational spectroscopy. *Physics and Chemistry of Minerals*, 30, 337-344.

Paterson, M. S. (1982) The determination of hydroxyl by infrared absorption in quartz, silicate glasses and similar materials. *Bulletin de Minéralogie*, 105, 20-29.

Reichart, P., Bergmaier, A., and Dollinger, G. (2006) Hydrogen Analysis of Minerals from the Earth Mantle. MLL Annual Report 2006, 62, available online: www.bl.physik.uni-muenchen.de/mlr-jb.html.

Reichart, P., Datzmann, G., Hauptner, A., Hertenberger, R., Wild, C., and Dollinger, G. (2004) Three-Dimensional Hydrogen Microscopy in Diamond. *Science*, 306, 1537-1540.

Rhede, D. and Wiedenbeck, M. (2006) SIMS quantification of very low hydrogen contents. *Applied Surface Science*, 252, 7152-7154.

Rossmann, G.R. (2006) Analytical methods for measuring water in nominally anhydrous minerals. In H. Keppler and J.R. Smyth, Eds., *Water in nominally anhydrous minerals*, 1-28, Mineralogical Society of America, Chantilly.

Rossmann, G.R. and Aines, R.D. (1991) The hydrous component in garnets: grossular-hydrogrossular. *American Mineralogist*, 76, 1153-1164.

Thomas, R. (2000) Determination of water contents of granite melt inclusions by confocal laser Raman microprobe spectroscopy. *American Mineralogist*, 85, 868 – 872.

Thomas, R. and Davidson, P. (2006) Progress in the determination of water in glasses and melt inclusions with Raman spectroscopy: A short review. *Z. geol. Wiss., Berlin*, 34, 159-163.

Thomas, R. and Davidson, P. (2007) Progress in the determination of water in glasses and melt inclusions with Raman spectroscopy: A short review. *Acta Petrologica Sinica*, 22, no. 12, 15-20.

Thomas, R., Kamenetsky, V.S., and Davidson P. (2006) Laser Raman spectroscopic measurements of water in unexposed glass inclusions. *American Mineralogist*, 91, 467-470.

Thomas, R., Metrich, N., Scaillet, B., Kamenetsky, V.S., and Davidson, P. (2008) Determination of water in Fe-rich basalt glasses with confocal micro-Raman spectroscopy. *Zeitschrift für geologische Wissenschaften*, 36, in print.

Zajacz, Z., Halter, W., Malfait, W.J., Bachmann, O., Bodnar, R.J., Hirschmann, M.M., Mandeville, C.W., Morizet, Y., Muntener, O., Ulmer, P., and Webster, J.D. (2005) A composition-independent quantitative determination of the water content in silicate glasses and silicate melt inclusions by confocal Raman spectroscopy. *Contributions to Mineralogy and Petrology*, 150, 631-642.

Kapitel 3

**“IR calibrations for water determination in
olivine and SiO₂ polymorphs”**

IR calibrations for water determination in olivine and SiO₂ polymorphs

Sylvia-Monique Thomas¹, Monika Koch-Müller¹, Patrick Reichart², Dieter Rhede¹, Rainer
Thomas¹, and Richard Wirth¹

¹ GeoForschungsZentrum Potsdam (GFZ), Telegrafenberg, 14473 Potsdam, Germany. Section 4.1

E-mail: smthomas@gfz-potsdam.de

² Universität der Bundeswehr München, LRT 2, 85577 Neubiberg, Germany.

Abstract

Most frequently applied infrared (IR) calibrations (Paterson 1982; Libowitzky and Rossman 1997) for quantitative water analyses in solids are based on a negative correlation between the IR molar absorption coefficient (ϵ) for water and the mean wavenumber of the corresponding OH pattern. The calibrations have been primarily acquired on hydrous minerals and glasses with several wt% water. However, e.g., Rossman (2006) stated, that they cannot be adopted to nominally anhydrous minerals (NAMs) but mineral-specific calibrations are needed.

In the present work we provide ϵ -values for synthetic and natural olivine and SiO₂ polymorphs. We were able to synthesize these minerals with specific isolated OH point defects, e.g., quartz with either B³⁺+H⁺=Si⁴⁺ or Al³⁺+H⁺=Si⁴⁺ substitutions. The IR spectra of, e.g., Al- or B-doped quartz display separated OH bands at different wavenumbers and hence allow to study the frequency dependence of ϵ . Water contents of both natural samples and our run products were determined using independent techniques as proton-proton (pp)-scattering (Reichart et al. 2004), confocal microRaman spectroscopy (Thomas et al. 2006) and secondary ion mass spectrometry (SIMS). Obtained data provided the basis to calculate new mineral-specific IR absorption constants. Moreover, we present a routine to detect OH traces in isotropic and anisotropic minerals using Raman spectroscopy combined with the "Comparator Technique".

For olivine with the mean wavenumber of 3517 cm⁻¹ an ϵ -value of 38000 ± 4000 l mol⁻¹_{H2O} cm⁻² was determined.

For another olivine (mean wavenumber of 3548 cm⁻¹) we obtained an ϵ -value of 47000 ± 5000 l mol⁻¹_{H2O} cm⁻².

Taking into account previous studies (Bell et al. 2003; Koch-Müller et al. 2006) we will discuss here the frequency dependence of ϵ for olivine. In case of the SiO₂ system it turns out that the magnitude of ϵ for one structure is independent of the type of OH point defect and therewith the peak position, but varies as a function of structure.

One single mean ϵ of 67000 ± 8000 l mol⁻¹_{H2O} cm⁻² was determined for a suite of quartz crystals with different OH point defects. For the high-pressure polymorph coesite a higher ϵ of 214000 ± 14000 l mol⁻¹_{H2O} cm⁻² was calculated,

that is in good agreement with earlier established data (Koch-Müller et al. 2001). For stishovite an even larger value of ϵ = 461000 ± 68000 l mol⁻¹_{H2O} cm⁻² was derived, similar to that determined by Pawley et al. (1993).

Evaluation of data from this study confirms that not using mineral-specific IR calibrations for the OH quantification in NAMs leads to inaccurate estimations of OH concentrations, that constitute the basis for modelling the earth's deep water cycle.

Key words: absorption coefficients, IR spectroscopy, Raman spectroscopy, pp-scattering, SIMS, nominally anhydrous minerals, quartz, coesite, stishovite, olivine

Introduction

Major earth's crust and mantle constituents, so-called nominally anhydrous minerals (NAMs), are able to incorporate traces of hydrogen in form of hydroxyl point defects in their structures (further on expressed as wt ppm H₂O or with the general term water). Even such low water amounts may have enormous effects on geodynamical processes, as they can change physical mineral properties, e.g., electrical conductivity and deformation strength (Mackwell et al. 1985; Karato 1990; Huang et al. 2005; Wang et al. 2006; Kohlstedt 2006). To evaluate implications of water contents in NAMs on a potential earth deep water cycle it is necessary to know their absolute water concentrations. For measuring and quantifying even traces of hydrous compounds (H₂O and OH) in geological material IR spectroscopy has been extensively used in the past and is regarded as advantageous technique by means of its high sensitivity and relatively simple performance (Rossman 2006). According to the Beer-Lambert law the absorption intensity (A_i) of a species in the measured sample is directly proportional to the concentration of the species (c) and the thickness (t) of the sample: $A_i = c \times t \times \epsilon_i$, with ϵ_i as the integrated molar absorption coefficient. Since IR spectroscopy is not self calibrating, several calibrations (Paterson 1982; Libowitzky and Rossman 1997) for quantitative water analyses in solids have been established in the past and are commonly used now. They mainly rely on hydrous minerals and glasses holding several % water by weight. These calibrations are based on a negative correlation between the IR molar absorption coefficient (ϵ) for water and the mean wavenumber of the corresponding OH pattern. The correlation reflects the dependence of the OH band position on the O-H...O distances in the structure and thereby also on the magnitude of the dipole moment which is proportional to the band intensity (e.g., Libowitzky 1999). However, it has been observed that these calibrations cannot be applied on NAMs (Rossman 2006) that contain hydrogen in ppm-level amounts incorporated mainly via OH point defects. Independently determined ϵ -values deviate significantly from the general linear wavenumber-dependent calibration

trends, e.g., Bell et al. (1995) determined for olivine with OH absorptions in the high-frequency range from 3650-3450 cm^{-1} an absorption coefficient, that is 2.3 times smaller than the value indicated by the Paterson (1982) calibration line. Moreover, Johnson and Rossman (2003) suggest a uniform ϵ -value for the feldspar group contrary to separate frequency-dependent values predicted by the general calibrations (e.g., Paterson, 1982: 174000 $\text{Imol}_{\text{H}_2\text{O}}^{-1} \text{cm}^{-2}$ for 3200 cm^{-1} ; 84000 $\text{Imol}_{\text{H}_2\text{O}}^{-1} \text{cm}^{-2}$ for 3500 cm^{-1}). Due to the lack of mineral-specific absorption coefficients commonly used calibrations allow only to determine relative water concentrations within one mineral group. To provide absolute data appropriate mineral-specific calibrations for each NAM are required by means of an independent absolute method (Rossman 2006). Such mineral-specific calibrations have been already performed for several mineral groups using independent quantification methods. Hence, integrated absorption coefficients for IR have been proposed, e.g., for olivine (Bell et al. 2003, Koch-Müller et al. 2006), feldspars (Johnson and Rossman 2003), pyroxenes (Bell et al. 1995) and garnets (Maldener et al. 2003; Rossman and Aines 1991; Rossman 1988). Quantitative methods to establish such independent data for NAMs include, e.g., hydrogen manometry (e.g., Bell et al. 1995), nuclear reaction analysis (NRA; Bell et al. 2003, 2004; Hammer et al. 1996; Maldener et al. 2001; Rossman et al. 1988) and nuclear magnetic resonance (NMR; Keppler and Rauch 2000, Cho and Rossman 1993, Johnson and Rossman 2003; Kohn 1996). However, all of them inhibit minor or major problems by means of special demands on sample preparation or minimum sample quantity. Further analytical techniques are SIMS and nuclear methods as elastic recoil detection analysis (ERDA) and pp-scattering. SIMS exhibits a challenge if intended to be used to detect water amounts < 1000 wt ppm in NAMs (e.g. Rhede and Wiedenbeck 2006) due to intractable factors as, e.g., the influence of matrix composition (e.g., Hervig 1987; Koga et al. 2003, Aubaud et al. 2007), high vacuum quality to reduce background hydrogen signals, problems due to too small crystal dimensions, a time consuming preparation and sample destruction. Nevertheless, SIMS also has basic advantages as insensitivity for sample orientation and a fine scale spatial resolution

(Yurimoto et al. 1989; Deloule et al. 1995; Koga et al. 2003; Kurosawa et al. 1992; Hauri et al. 2002; Aubaud et al. 2007) and was previously used to estimate absorption coefficients, e.g. for coesite (Koch-Müller et al. 2001) and stishovite (Pawley et al. 1993). However, considering the above-mentioned problems the ε -values obtained need an evaluation. SIMS as well as ERDA (e.g., Sweeney et al. 1997) and pp-scattering are under development to be improved for the applicability at low hydrogen detection limits. In particular, pp-scattering, rarely used in geosciences (Wegden et al. 2005; Reichart et al. 2004) so far, holds considerable promise for the hydrogen detection by means of sub-ppm sensitivities as well as sub- μm spatial resolutions. A highly informative review on analytical techniques including advantages, disadvantages and potential future developments can be found in Rossman (2006). Another method, though yet hardly considered for quantification of OH contents in anisotropic minerals, is the confocal microRaman spectroscopy. Raman spectroscopy is generally used to investigate molecular vibrations in a light scattering experiment. As consequence of the interaction of the energy of an incident light beam (in our study an Ar⁺ laser) with the induced vibrational modes in a sample, the incident energy is raised or lowered by inelastic scattering of the photons, with the frequency shift giving characteristic information about the phonons (i.e. the vibrational species) involved. According to Moritz (1999) the following linear relationship exists between the measured intensity of the inelastic

scattered light and the concentration of the activated species: $I_i = \left(\frac{\delta\sigma}{\delta\Omega} \right) \frac{c_i}{M_i} N_A V \Omega_{\text{obs}} F^{-1} C I_0$,

where $\frac{\delta\sigma}{\delta\Omega}$ is the differential scattering cross section, c_i is the concentration of the species i ,

M is the molar mass of the species i , N_A is the Avogadro constant, V is the excited volume, Ω_{obs} is the angle of observation, F is the projection screen of the detector entrance on the observed volume, C is the detector efficiency constant and I_0 is the intensity of the laser excitation. Peak intensities are affected by various factors as laser power density and effective sampling volume. Laser power density in turn depends on the laser power itself, on

the beam diameter and on the angle of incidence onto the sample. Effective sampling volume is a function of laser focusing, sample dimension, sample transparency, reflections, refractions and roughness of sample surface. The Raman peak intensity moreover depends on the polarizability of the molecule vibration, the intensity of the source, and the concentration of the activated species (Skoog and Leary 1992). Given no significant light absorption by the sample occurs, intensity increases with the fourth power of the frequency of the source and is usually directly proportional to the concentration of the activated species (Kohlrausch 1943; Skoog and Leary 1992; Thomas 2000; Schabel 2005). By using a reference and given constant experimental factors and excited sampling volume the second part of the equation after Moritz (1999) is canceled and permits to obtain quantitative data by the simple and direct comparison of the reference with an unknown sample. However, remaining factors that should be considered are differences in refraction, molar mass and density.

Two different water quantification procedures using Raman spectroscopy have previously been suggested, the internal calibration and the external calibration (Chabiron et al. 2004; Behrens et al. 2006; Di Muro et al. 2006a, b; Thomas 2000, 2002; Thomas et al. 2000, 2003, and 2006; Zajacz et al. 2005; Severs et al. 2007). The internal calibration utilizes the normalization of the total water band ($\text{H}_2\text{O}_\text{T}$) to either the T-O-T (T: tetrahedrally coordinated cations) bending band at $\sim 500 \text{ cm}^{-1}$, or the T-O stretching band near 1000 cm^{-1} . However, the feasibility of this technique to low concentrations $< 0.1 \text{ wt}\%$ has been controversially discussed in the past, because of potential high errors due to, e.g., the strong influence of variable matrix compositions on the relative band intensities and positions. Moreover, differences in detector efficiencies between the low- and the high-frequency range might also affect recorded intensities. As previous Raman spectroscopic studies primarily focused on the water determination in glasses and melt-inclusions, its application to trace and quantify low concentrations of OH in minerals has been scarcely considered to date. Subsequent to endeavors to adapt Raman spectroscopy for the water determination in cubic garnets

Arredondo and Rossman (2002) suggested that the latter technique is not generally suitable to determine trace OH concentrations in those minerals, as they could not observe a consistent correlation of OH/Si ratio with sample water concentrations. However, they utilized the internal calibration using the ratio of the integrated area of depolarized Raman bands in the $\sim 3600\text{ cm}^{-1}$ stretching region to Si-O stretching bands in the $800\text{-}900\text{ cm}^{-1}$ region. A technical progress results from the introduction of the “Comparator Technique” (Thomas and Davidson 2006, 2007; Thomas et al. submitted). Recently, the latter technique has proven advantageous in particular for tracing water in natural and synthetic glasses, even down to very low H_2O concentrations (e.g. Thomas and Davidson 2006; Thomas et al. submitted), with the use of one single well-characterized reference material being sufficient and making a calibration curve unnecessary. The latter work (Thomas et al. submitted) also reports the applicability of the “Comparator Technique” for gem-quality garnets holding ppm-level water contents. The approach of the present project is to test if Raman spectroscopy could also be applied for the quantification of OH contents in anisotropic single-crystals such as quartz, coesite, stishovite and olivine. Further aims of this paper are to provide mineral-specific absorption coefficients to enable routine OH quantification with IR spectroscopy and to study their frequency dependence using IR-spectroscopy combined with independent methods as Raman spectroscopy, pp-scattering and SIMS.

Experimental and Analytical techniques

Syntheses and Samples

To study the potential dependence of ϵ on the OH band position in IR spectra we synthesized olivine and SiO_2 polymorphs with specific isolated hydroxyl point defects, e.g. quartz, coesite and stishovite with $\text{B}^{3+} + \text{H}^+ = \text{Si}^{4+}$ and/or $\text{Al}^{3+} + \text{H}^+ = \text{Si}^{4+}$ substitutions. The starting materials for the synthesis experiments were pure oxide mixtures to that H_2O was added as either $\text{Al}(\text{OH})_3$, H_3BO_3 or as pure bidistilled H_2O . Starting compositions and experimental conditions are listed in Table 1. The starting powders were loaded either in gold capsules (10 mm long

gold capsules with an outer diameter of 6 mm and a wall thickness of 0.5 mm) for piston cylinder experiments or in Pt capsules for multi-anvil runs that were sealed by cold welding to avoid water loss during the run. Experiments were carried out with water in excess in an end-loaded piston-cylinder apparatus (Boyd and England 1960) and in a multi-anvil press. After quenching, the recovered capsule was opened and checked for the presence of excess water, which could be observed in all cases. Recovered single crystals were used for analysis. To provide a series of reference material with varying water concentrations we selected in addition to synthetic products various crack free, homogeneous natural samples: natural quartz (HQV), olivines (Ud29 and San Carlos olivine: SCO) and dry synthetic quartz from Japan (SQT).

Table 1. Starting compositions and experimental conditions.

| Run no. | Assembly ^{§§} | Starting composition (wt%) | | | P(GPa) | T (°C) | Time (h) | Run products |
|----------------------------------|------------------------|---|------------------|-------------------|--------|--------|----------|--------------|
| | | MgO | SiO ₂ | H ₂ O | | | | |
| Piston cylinder apparatus | | | | | | | | |
| SMT503 | - | - | 99.0 | 1.0* | 3.0 | 950 | 132 | quartz |
| SMT504 | - | - | 99.0 | 1.0 [†] | 3.0 | 950 | 60 | quartz |
| SMT508 | - | - | 99.0 | 1.0* | 3.0 | 950 | 72 | quartz |
| Multi-anvil apparatus | | | | | | | | |
| WIM04 [#] | 18/11 | - | 97.0 | 3 | 7.5 | 1100 | 2 | coesite |
| MA009 | 18/11 | - | 99.0 | 1.0* | 7.5 | 930 | 3 | coesite |
| MA061 | 14/08 | - | 98.0 | 2.0 ^{††} | 8.0 | 1000 | 20-24 | coesite |
| MA117 | 14/08 | - | 98.0 | 2.0* | 5.9 | 1400 | 1.5 | coesite |
| MA020 | 18/11 | 47.6 | 35.4 | 17 | 5.9 | 1100§ | 3 | forsterite |
| MA118 | 14/08 | - | 96.0 | 4.0 [†] | 12.3 | 1240 | 6.1 | stishovite |
| MA034 | 18/11 | - | 99.0 | 1.0 | 8.0 | 800 | 24 | stishovite |
| <i>Notes:</i> | | | | | | | | |
| * | | – H ₂ O as H ₃ BO ₃ . | | | | | | |
| † | | – H ₂ O as Al(OH) ₃ . | | | | | | |
| †† | | – 1 wt% H ₂ O as Al(OH) ₃ and 1 wt% B. | | | | | | |
| # | | – synthesized at ETH Zurich by W. van Westrenen. | | | | | | |
| § | | – temperature estimated using power due to break of thermocouple. | | | | | | |
| | | Uncertainty of given value is within ±100° C. | | | | | | |
| §§ | | – octahedron edge length/truncation edge length (mm). | | | | | | |

Transmission electron microscopy (TEM)

To characterize microstructures, sample homogeneities and compositions of the quartz

samples SMT503 and SMT504 by TEM, specific foils were prepared from single crystals mounted in crystal-bond using the focused-ion-beam technique (Wirth 2004) and a FEI FIB200 focused ion beam device with a Ga-ion source operated with an acceleration voltage of 30 kV. Final foils of $15 \times 10 \times 0.2 \mu\text{m}$ in size were removed from the sample using an optical microscope and placed onto a perforated TEM carbon grid. No further carbon coating is required. TEM analyses were performed in a Philips CM200 electron microscope operating at 200 kV with a LaB_6 electron source, a Gatan imaging filter for the acquisition of energy-filtered images and high-resolution electron micrographs and an energy-dispersive X-ray spectroscopy system for analytical electron microscopy.

IR spectroscopy

For IR spectroscopy single-crystals were ground and doubly polished using diamond spray with $0.25 \mu\text{m}$ in the last step. Moreover, parallelepipeds were prepared for olivine Ud29 and natural quartz HQV. For analysis the crystals were placed on a KBr plate or over steel pinhole apertures (in case of large natural samples). Koch-Müller et al. (2001) conclude that, in the special case of coesite, quantitative measurements of single-crystals may be obtained on randomly oriented sections using an unpolarized spectrum and calculating the total absorption by multiplying obtained absorbance values by three. Therefore, unpolarized IR spectra of synthetic coesite were recorded from 3000 to 4000 cm^{-1} at ambient conditions with a Bruker IFS 66v FTIR spectrometer equipped with a Hyperion microscope, an InSb detector, a KBr beamsplitter and a globar. The spot size used in the measurements ranged from $30 \times 30 \mu\text{m}$ to $100 \times 100 \mu\text{m}$, according to varying sample dimensions, and up to 1024 scans were taken with a resolution of 2 cm^{-1} . The sample thickness was determined either using a micrometer (large natural samples) or using the eyepiece reticule and stage micrometer scale of an optical microscope. The final thickness ranged from $50 \mu\text{m}$ for synthetic samples to 3 mm for SCO. For single-crystals of synthetic and natural quartz, stishovite and olivine, polarized IR spectra were recorded. The absorbance of the oriented single-crystals was

measured in extinction position with the electric vector (E) parallel to the optical indicatrix axes. Orientations were either estimated from morphology, from lattice vibrations (by comparison with oriented reference samples) or oriented sections were prepared using single-crystal X-ray diffraction (natural quartz HQV). The integrated absorbances and area-weighted average (Libowitzky and Rossman 1997) of the peak positions were determined using the PeakFit software by Jandel Scientific. Total absorbances were calculated either by $A_{\text{itot}} = 2 \times A_i \perp c + 1 \times A_i \parallel c$ in the case of quartz and stishovite or by $A_{\text{itot}} = A_{\text{ix}} + A_{\text{iy}} + A_{\text{iz}}$ in the case of olivine. To study the OH distribution in our samples synchrotron IR measurements were performed at the Infrared beamline at BESSY II using a Nicolet 870 FTIR spectrometer equipped with a Continuum microscope. Line scans and area maps of the spectral region $2700\text{--}3800\text{ cm}^{-1}$ were recorded for quartz and coesite with a local resolution of $10 \times 10\text{ }\mu\text{m}$ or $15 \times 15\text{ }\mu\text{m}$.

Raman spectroscopy

Single-crystals used in previous IR studies were characterized with confocal microRaman spectroscopy. No additional sample preparation was required. Great care was taken to record Raman spectra on crystal faces identical to that used for IR measurements. All analyses were performed in backscattering geometry using a LabRam HR800 UV-VIS spectrometer (grating: 1800 grooves/mm) equipped with a motorized XY-stage, an Olympus optical microscope and a long working distance 100x objective (LWD VIS, NA = 0.80, WD = 3.4 mm). Spectra were collected with a Peltier-cooled CCD detector. The 488-nm line of a Coherent Ar⁺ Laser Model Innova 70-3 at 300 mW or 450 mW was used for sample excitation. For all measurements a confocal pinhole of 100 μm was used, corresponding to a spectral resolution of about 1 cm^{-1} . For sample characterization spectra were acquired in the low-frequency region 200 to 1200 cm^{-1} . To probe the OH region spectra were taken in the high-frequency range from 2800 to 3980 cm^{-1} corresponding to 3 spectral windows. Raman intensities may be affected by the quality of the sample surface. Therefore, to avoid

measurement errors due to sample surface heterogeneities, the laser beam was focused on the top of the sample surface using the 100x objective and then lowered by 4 μm before starting the measurement. To maintain consistency, this procedure was repeated for each Raman measurement throughout this study. Dimensions of the focusing tube were calculated using the formulas according to Overall (2000) to be about (0.7 x 3.1) μm during our measurements. However, the latter value should be taken as an approximation, since factors like light refraction can have an influence on these dimensions depending on excited material.

Before and after each sample measurement a reference spectrum, in this case of the rhyolitic SD-6.53% glass (Table 1) with 6.53 % water by weight was recorded. The integrated intensity obtained in the frequency range 3100 to 3750 cm^{-1} served as intensity reference, and to monitor the device stability. All subsequent spectra taken under the same conditions were normalized using this standard. Measuring conditions are listed in Tables 2 and 3. To provide adequate signal to noise ratios spectra acquisition times varied from generally 100 seconds for synthetic quartz or coesite to 600 s for samples containing very low water concentrations (HQV, Ud29, MA118, MA034). For further calculations integrated intensity data were standardized to counts per second (cps).

Unoriented statistical measurements. We performed statistical measurements (Table 2) on randomly oriented grains of our syntheses products. We conducted up to 17 single analyses on each polished crystal plate by rotating the plate by several degrees with respect to the microscope axis before subsequent spectrum acquisition.³ This was done to take into account the anisotropic behavior of our samples. Mean values of the integrated intensities obtained were used for further calculations (Table 2).

Polarized measurements. To check for a difference to statistical measurements and to avoid high errors due to the high anisotropy of the OH signature we additionally recorded

³ Parallelepipeds of olivine were additionally turned by 90 ° and thereafter analyzed as per the defined procedure.

polarized Raman spectra from Ud29, stishovite and B-doped quartz. A polarizator was placed in the optical path of our instrument behind the spectrometer entrance and a polarization foil behind the notch filter in front of the detector entrance. To test the quality of the polarization, we analyzed one staurolite crystal of Pizzo Forno. Raman spectra of the OH region (Fig. 1) were in excellent agreement with polarized IR spectra reported by Koch-Müller and Langer (1998). Hence, the accuracy of our polarization assembly could be confirmed. Polarized Raman spectra of quartz, stishovite and olivine were obtained as described for IR spectroscopy.

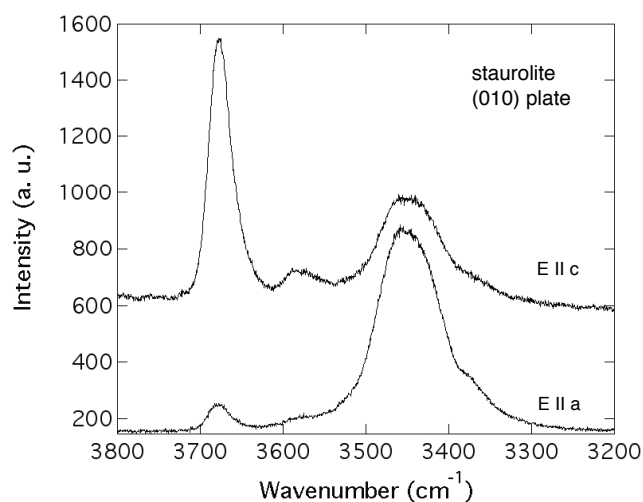


Figure 1. Polarized Raman spectra of a (010) plate of natural staurolite with E II c and E II a. The OH band pattern displays the strong pleochroism of the respective dipoles and moreover, compares well with IR data of Koch-Müller and Langer (1998).

Spectra treatment and quantification procedure

When possible we adopted to all our spectra a constant linear baseline correction in the integration limits between 3100 and 3750 cm^{-1} . For Ud29 and Al-doped quartz polynomial fits of higher order were required to define the spectral background. Spectra were fitted using the LabSpec software. Total integrated intensities were calculated analogue to the method of Libowitzky and Rossman (1996) with $I_{\text{tot}} = 2 \times I_{\perp c} + 1 \times I_{\parallel c}$ in the case of uniaxial stishovite and quartz and by $I_{\text{tot}} = I_x + I_y + I_z$ in the case of orthorhombic olivine adopting the measurement of integrated intensities along the three orthogonal crystallographic axes (Table 3).

For glasses resembling a narrow compositional range with densities $\sim 2.2 \text{ g/cm}^3$, such as analyzed throughout this study, this method has proven to be matrix-independent (Thomas and Davidson, 2006; Thomas et al. in prep.). Therefore, a density correction of measured Raman intensities is unnecessary for the glasses. However, since we excite in the denser silicates a different mass in a constant volume, we corrected in a first step our integrated intensity fitted from Raman spectra for density variations between reference material ($\rho = 2.26 \text{ g/cm}^3$) and sample ($\rho_{\text{quartz}} = 2.65 \text{ g/cm}^3$, $\rho_{\text{coesite}} = 2.93 \text{ g/cm}^3$, $\rho_{\text{stishovite}} = 4.3 \text{ g/cm}^3$, $\rho_{\text{olivine}} = 3.27 \text{ g/cm}^3$) with $I_{i,\text{sample,corr}} = I_{i,\text{sample,meas}} \times \rho_{\text{ref}} / \rho_{\text{sample}} (\text{g/cm}^3)$. As Raman spectroscopy measures the molar concentration of the activated species, the water concentration in mol/l was then calculated using following equation: $c_{\text{H}_2\text{O}} (\text{mol/l}) = I_{i,\text{sample,corr}} \times c_{\text{H}_2\text{Oref}} (\text{mol/l}) / I_{i,\text{ref}}$, where I_i are the integrated density-corrected intensities of sample and reference (second step). According to Snell's law and the Fresnel equations measured intensities are underestimated and have to be corrected for following reflectance/refraction errors (third step): quartz 1%, coesite 2%, stishovite 8%, olivine 4%. These errors are provoked by light refraction discrepancies due to differences of refractive indices between reference material ($n_{\text{ref}} = 1.50$) and sample ($n_{\text{quartz}} = 1.55$; $n_{\text{coesite}} = 1.6$; $n_{\text{stishovite}} = 1.8$; $n_{\text{olivine}} = 1.66$). We used mean refraction values given in Tröger (1956). In the fourth step the water concentration in wt% can be recalculated using the equation $c_{\text{H}_2\text{O}} (\text{wt}\%) = c_{\text{H}_2\text{O}} (\text{mol/l}) \times 1.8 / \rho_{\text{sample}} (\text{g/cm}^3)$. Finally, a calculation of specific integrated molar absorption coefficients according to the equation $\varepsilon_i = (1.8 \times A_{i,\text{tot}}) / (c_{\text{H}_2\text{Owt}\%} \times t \times \rho)$ is possible, using $A_{i,\text{tot}}$ fitted from IR spectra, the thickness (t) and the density of the sample (ρ).

Proton-Proton-scattering

For hydrogen analysis using pp-scattering (3×4) mm sized samples were ground and doubly polished until they had a final thickness $< 200 \mu\text{m}$ (SQT $102 \mu\text{m}$, HQV $127 \mu\text{m}$, SCO $111 \mu\text{m}$, Ud29 $122 \mu\text{m}$). Pp-scattering analysis was performed at the Munich tandem

accelerator lab using a 13 MeV and a 25 MeV proton beam. Basic information about this technique is given in Reichart et al. (2004) and in Thomas et al. (submitted). The measured hydrogen content within a certain thickness given in absolute units (H atoms/cm²) is converted in H atoms per total atoms using the thickness and atomic density of the samples. Due to unavailability of the SNAKE microbeam setup at that time, we used a millimeter focused beam and a spare detector setup with two 40 mm × 60 mm large semiconductor silicon strip detector pads (7 strips each) at scattering angles of 40°-50°, which filters for coincidence events in opposite sectors within a timing window of about 2-3 ns. The beam was averaged on an area of about 1 mm² diameter.

Secondary ion mass spectrometry

SIMS measurements of H in selected samples (WIM04_C1, MA009_a, SMT503_Z7, SMT504_a, MA061, MA034_8, HQV and SQT) were performed on the Cameca IMS 6f ion microprobe. We used an epoxy-free sample mounting technique similar to that reported by Koga et al. (2003) and Aubaud et al. (2007). Samples and standards were mounted in one Al-disk, prior filled with 2-8 mm indium spheres (Merck no. 12196), that were molten by placing the metal disk on a hot plate at > 160 °C. The crystals, prior doubly polished (see above IR spectroscopy section), were pushed by hand into the air-cooled indium metal using a glass slide. The whole assembly was pressed carefully with 4.9 t in a hydraulic press (Carl Zeiss Jena) to obtain a flat surface as well as to avoid distracting cavities between indium and crystals. A polish with alumina suspension, as described in Aubaud et al. (2007), was not adopted to prevent a possible placement of aluminum impurities into the crystals that would lead to errors in the measurement of that trace element. Finished sample mounts were stored for 12 hours at 70° C under low vacuum, coated with a ~ 30 nm gold layer and were put into the airlock chamber at pressure < 2.5 E-07 Pa (Wiedenbeck et al. 2004) to outgas for at least 72 hours before starting the measurement. Our analytical setup employed a 10 kV, 2 nA Cs⁺ beam. The total vacuum pressure in the sample chamber during the measurement

was $< 5\text{E-}08$ Pa. In addition the LN_2 trap was used to freeze remnants of water in the assembly. The primary ion beam was rastered over a $(25 \times 25) \mu\text{m}$ area. Only ions originating from the central area (approx. $10 \mu\text{m}$) were counted, by utilizing a $100 \mu\text{m}$ field aperture. Measurements employed an elevated mass resolving power of $M/\Delta M \approx 3000$, the energy window was set to 50 eV and no offset voltage was applied to the sample high voltage. A number of single-crystals of one sample suite were analyzed; up to 2 measurements were performed on each crystal. One analysis consisted of 150 cycles with counting times per peak stepping sequence of 10 s for ^1H and 2 s for ^{30}Si . Negatively charged secondary ions were extracted from the sample using -7.5 kV potential with charge compensation provided by normal incidence electron flooding. The $^1\text{H}/^{30}\text{Si}$ ratios used to establish the working curve were calculated by averaging the final 8 cycles from each analysis. Finally the curves were standardized using our natural quartz samples HQV and SQT, prior well characterized by pp-scattering.

For semi-quantitative SIMS measurements of boron traces two B-doped quartz- and 8 coesite single-crystals were embedded in epoxy resin in a glass mount and polished. The sample mount was then cleaned with high purity ethanol and stored at 70°C under low vacuum before coating with ~ 30 nm gold. Our analytical setup employed a primary 12.5 kV, 5 nA $^{16}\text{O}^-$ beam focused to a $\sim 20 \mu\text{m}$ diameter spot. The sample surface was cleaned prior to each spot analysis by pre-sputtering for 3 minutes. Measurements employed a low mass resolution of $M/\Delta M \approx 300$, the energy window was set to 50 eV and a -75 V offset voltage was applied to the sample high voltage of 10 kV. Two sample spots were analyzed on each single-crystal. The single measurement consisted of 50 cycles of the peak stepping sequence with counting times of 10 s for ^{11}B and 2 s for ^{30}Si . Secondary ion count rates were restricted by a $750 \mu\text{m}$ field aperture combined to a $50 \mu\text{m}$ contrast aperture. Measured $^{11}\text{B}/^{30}\text{Si}$ ratios were calibrated using the NIST SRM glasses 610 and 612 as reference material.

Results

Run products of the high-pressure experiments were identified and characterized using Raman spectroscopy and TEM. Our syntheses resulted in clear single-crystals of B-doped quartz, Al-doped quartz, B-doped and B-free coesite, Al-doped and Al-free stishovite and forsterite (cf. Table 1). To choose a set of homogeneous samples for our study we omitted specimens with large-scale heterogeneities of the hydrogen content from our sample list, e.g., quartz QKM (Fig. 2) that contains a high quantity of fluid inclusions. TEM of B-doped quartz samples SMT503 and SMT504, IR line scans (globar light source), IR area maps (synchrotron light source) as well as randomly chosen spots for Raman measurements of natural and synthetic samples used in this study did not reveal significant heterogeneities of the OH distribution. No molecular water or nanometer-sized inclusions of additional phases were detected in the samples.

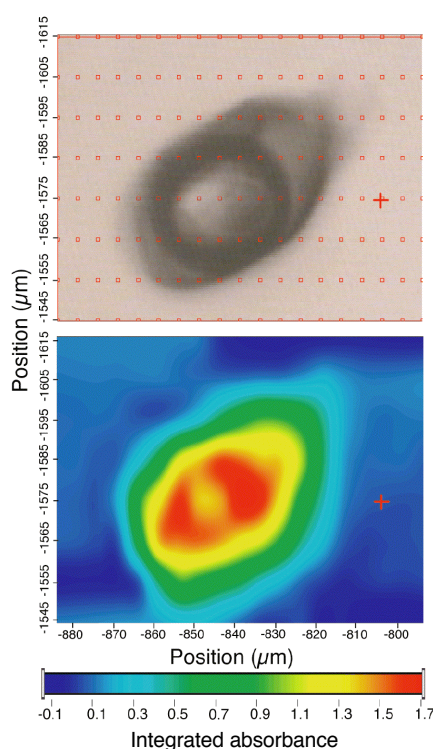


Figure 2. Measuring points (upper section) and corresponding area map (lower section) of the OH distribution in the natural quartz sample QKM (measured sample area: $50 \times 90 \mu\text{m}$), recorded with a local resolution of $15 \times 15 \mu\text{m}$. The map resembles the integrated spectral intensity of the measured spectral region from 3700 to 3000 cm^{-1} for each sample point. The final area map (step size $5 \times 10 \mu\text{m}$) reveals an inclusion and therewith the heterogeneity of the sample OH distribution. As we require homogeneous material for our present study, such substances were omitted from our sample list.

Infrared spectroscopy

Quartz

Synthetic quartz crystals are typically up to 150 μm in size. Single-crystal IR spectra demonstrate that we successfully managed to separate generally complex OH band patterns as, e.g., observed in our natural quartz HQV (Fig. 3) by incorporating specific OH defects. IR spectra of natural but also synthetic quartz are characterized by numerous OH bands that arise due to the incorporation of H^+ associated with the coupled substitution of a variety of trace impurities as Li^+ , Al^{3+} , Fe^{3+} , Na^+ , K^+ , Cu^+ , Ag^+ (e.g., Kats 1962, Kats et al. 1962, Johnson 2006; Kronenberg 1994; Rovetta et al. 1989). Here studied natural quartz (HQV) reveals bands at 3200, 3313 (Al^{3+}), 3378 (Al^{3+}), 3430 (Al^{3+}), 3470 (H^+)⁴, 3486 (H^+)⁴, 3511 (Li^+) and a shoulder at 3400 cm^{-1} (Fig. 3); band assignments were done according to above cited literature. The OH features at 3200 and 3400 cm^{-1} have been reported in prior studies, but could not be assigned to distinct point defects (Kronenberg 1994) so far. The spectrum of synthetic B-doped quartz (Fig. 3) consists of a sharp OH band at 3595 cm^{-1} with a FWHM of $\sim 7\text{cm}^{-1}$. B-doped quartz SMT508 reveals in contrast to B-doped quartz SMT503 additionally two weak shoulders at 3585 and 3610 cm^{-1} that are reported to be possibly due to impurities of Al^{3+} (Kats1962). The B-coupled OH defect shows a strong anisotropy with the highest absorption intensity observed parallel to the c-axis. The OH band at 3595 cm^{-1} has been observed for the first time at 77 K, only in the spectra of synthetic quartz (Staats and Kopp 1974). The authors proposed its origin coupled to boron impurities. However, they could not confirm its prominence in natural quartz. More recently, the full width at half maximum (FWHM) of the associated 3595 cm^{-1} band was used to distinguish, e.g., natural from synthetic amethyst (Karampelas et al. 2005). B-contents derived from SIMS are in the range of 60 ± 6 ppm B for SMT508 ($333 \text{ B}/10^6 \text{ Si atoms}$) and of 400 ± 40 ppm B ($2220 \text{ B}/10^6 \text{ Si atoms}$) for crystals of sample SMT503. A comparison of the boron concentrations with the

⁴ Hydrogen interstitials; unambiguous defect association is uncertain to date (cf. Kronenberg et al. 1994).

OH band intensity shows that these bands must be associated with the boron incorporation to OH defects in the sample structures.

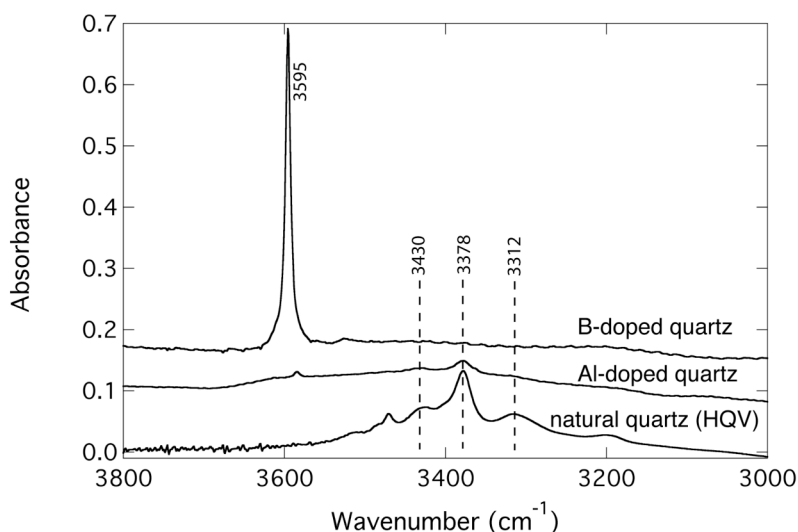


Figure 3. Comparison of the unpolarized IR spectra of natural quartz (HQV, lowermost spectrum) with spectra of Al-doped (middle) and B-doped quartz (upper). Natural quartz display a very complex OH band pattern, whereas our synthetic samples show separated OH bands due to isolated OH point defects.

Al-doped quartz (SMT504) has a more complex OH signature with the area-weighted average of the peak positions of 3400 cm^{-1} . From the IR spectrum following OH bands are distinguishable: $3312\text{ (Al}^{3+}\text{)}$, $3378\text{ (Al}^{3+}\text{)}$, $3430\text{ (Al}^{3+}\text{)}$ and 3584 cm^{-1} . The prominence of the band at 3584 cm^{-1} confirms the assumption to be caused by Al^{3+} in B-doped quartz. The Al-doped quartz shows a very weak pleochroism. In contrast to natural quartz specimens (e.g., Kronenberg 1994) all bands but 3430 cm^{-1} display the highest absorption intensity parallel to the c-axis, whereas the OH band at 3430 cm^{-1} seems to be nearly isotrope.

Coesite

Dimensions of coesites are typically $(200 \times 200 \times 50)\text{ }\mu\text{m}$. IR spectra of coesite crystals used in this study are shown in Figure 4. Samples WIM04, MA061 and MA009 reveal a similar OH band pattern with features at $3576, 3520, 3459\text{ cm}^{-1}$ (ν_1, ν_2, ν_3) and two very weak bands at 3300 and 3210 cm^{-1} (ν_4 and ν_5). All the bands have been observed previously in coesite (Li et al. 1997; Mosenfelder 2000; Koch-Müller et al. 2001, 2003) and have been assigned by

Koch-Müller et al. (2001) to be due to the hydrogarnet substitution type 1 and Al-based defects, respectively. Coesite single-crystals of samples WIM04 and MA117 show minor proportions of OH bands at 3460 (v7), 3422 (v8), 3407 (v9), 3379 (v10) that were prior reported for coesites synthesized at 8.5 GPa and 1200 °C and are assigned to the hydrogarnet substitution type 2 (Koch-Müller et al. 2003). We studied besides coesites incorporating OH via the hydrogarnet substitution (Fig. 4), also coesite crystals (MA117) that incorporate hydrogen primarily via the B-based defect (Fig. 4: lowermost spectrum). The FTIR spectra of such coesites is characterized by sharp OH signals at 3535 and 3500 cm^{-1} , which were earlier assigned by Koch-Müller et al. (2001) to B-based point defects (v6a and v6b). Details on B-coesite can be found in Deon et al. (submitted). The latter assignment to boron defects can additionally be confirmed due to the fact that the two bands are also prominent in the samples MA061 and MA009, whereas they are only present as shoulders in WIM04. This is consistent with the addition of boron acid to the starting materials of MA009, MA061 and MA117 (see Table 1). In addition the trace element analyses of boron result in 10 ± 1 wt ppm B ($56 \text{ B}/10^6 \text{ Si atoms}$) for WIM04 and in 40 ± 4 wt ppm B ($222 \text{ B}/10^6 \text{ Si atoms}$) for MA061, $49 \text{ wt} \pm 5 \text{ ppm B}$ ($272 \text{ B}/10^6 \text{ Si atoms}$) for MA009 and $290 \pm 30 \text{ wt ppm B}$ ($1600 \text{ B}/10^6 \text{ Si atoms}$) for MA117 (see also Deon et al. submitted).

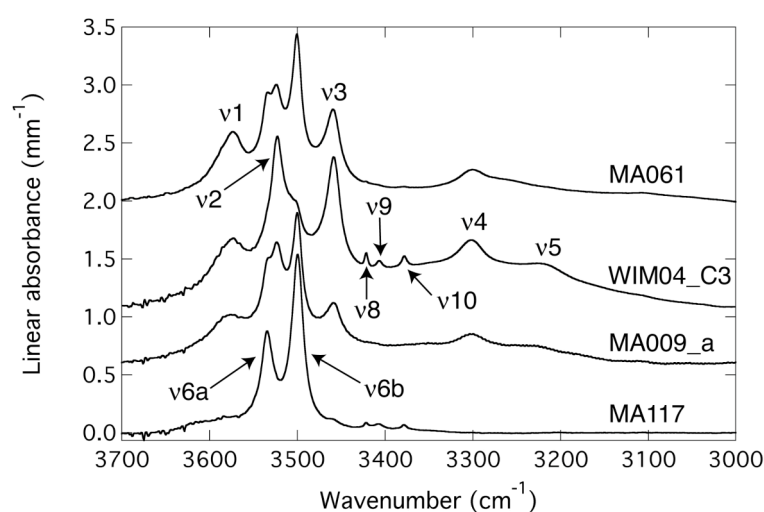


Figure 4. Comparison of unpolarized spectra of the OH region in coesite crystals studied herein. Band assignments were done according to Koch-Müller et al. (2001 and 2003).

Stishovite

Stishovite samples consist of very fine-grained crystals with a maximum size of (50 x 50 x 100) μm . Al-bearing stishovite reveals a broad OH band at 3122 cm^{-1} . This feature is consistent with previous data and was assigned to be associated with the coupled substitution of Al^{3+} and H^+ on the octahedral Si^{4+} site (Pawley et al. 1993; Smyth et al. 1995; Panero et al. 2003; Gibbs et al. 2004; Bromiley et al. 2006; Litasov et al. 2007). According to Bromiley et al. (2006) the broad asymmetric OH feature clearly comprises two OH bands, the main band at $3111\text{--}3134\text{ cm}^{-1}$ and a weaker shoulder at $3158\text{--}3167\text{ cm}^{-1}$, where the latter component increases as function of the Al concentration. The latter description compares well with our IR spectra that display a small shoulder on the main OH band at 3122 cm^{-1} .

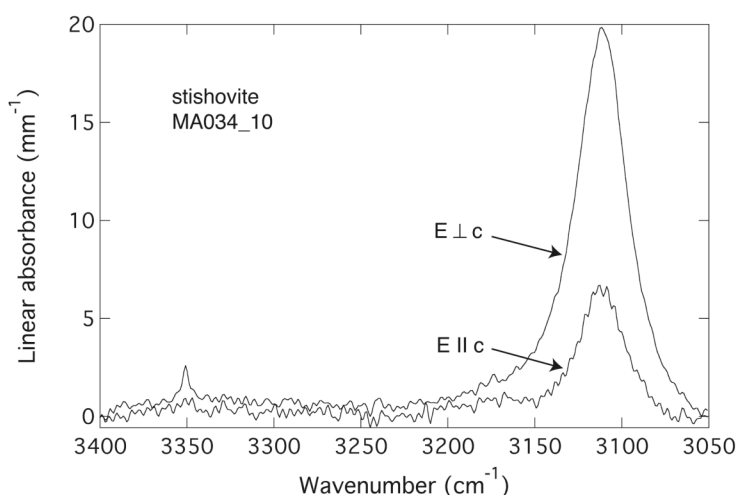


Figure 5. Polarized IR spectra of Al-free stishovite revealing a broad anisotropic OH band at 3125 cm^{-1} . A weak shoulder is indicated in the region $3200\text{--}3150\text{ cm}^{-1}$ as well as a very weak OH feature at 3350 cm^{-1} .

Polarized IR spectra of Al-free stishovite are presented in Figure 5. Al-free stishovite MA034 displays a similar spectrum compared to Al-bearing stishovite, though no Al was added to the starting powder. It consists of a broad OH band centered at 3125 cm^{-1} and a very weak OH feature at 3350 cm^{-1} . Al-free stishovite normally displays three separate OH bands at 3311 , 3238 and 3111 cm^{-1} that are suggested to be caused by H incorporated at different structural sites (Bromiley et al. 2006). However, it has been reported that the band at $3111\text{--}3134\text{ cm}^{-1}$ is prominent in IR spectra of both Al-free and Al-bearing stishovite (Bromiley et al. 2006;

Litasov et al. 2007). Polarized spectra of our stishovite crystals are consistent with prior studies, i.e., they reveal a strong pleochroism with the OH feature having the highest intensity perpendicular to the crystallographic c-axis.

Olivine

Olivine crystals of this study (Fig. 6) are characterized by very complex OH band patterns in the IR spectra. Figure 6 shows IR spectra of MA020 (unpolarized) and SCO [polarized with E parallel to (100)].

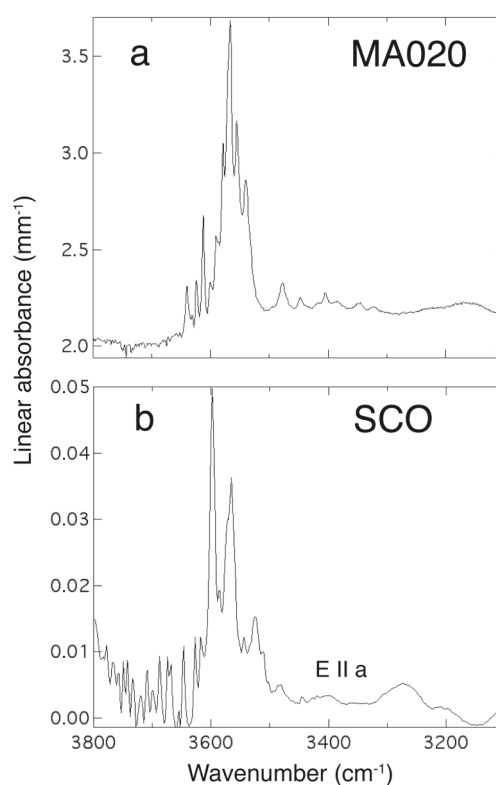


Figure 6. Comparison of the a) unpolarized IR spectrum of synthetic forsterite MA020 with the b) polarized IR spectrum of SCO recorded parallel to the a-axis. Both spectra consist of a complex OH band pattern, in which group I bands are dominating (e.g., Bai and Kohlstedt 1993; Beran and Libowitzky 2006).

The IR spectra for kimberlitic olivine Ud29 used in this study can be found in Koch-Müller et al. (2006). Two groups of OH bands are distinguishable in all IR spectra: group I from 3650 to 3450 cm^{-1} in the high-energy and group II from 3450 to 3200 cm^{-1} in the low-energy region (groups according to Bai and Kohlstedt 1993). Group one is dominant with respect to the band intensity. With respect to the polarization behavior the strongest absorption is

prominent with E parallel to (100). This is in good agreement to what is known from prior vibrational studies for olivine (e.g., Beran and Libowitzky 2006; Koch-Müller et al. 2006).

Raman spectroscopy

All sample spectra show useful Raman signals in the OH stretching region. Raman data for the OH region are summarized in Tables 2 and 3. The high-energy Raman spectrum of the reference glass SD-6.53% can be found in Thomas et al. (submitted). OH signatures observed in unpolarized as well as in polarized Raman spectra of the samples are consistent with the OH features from the IR measurements (cf. Figs. 7 and 8).

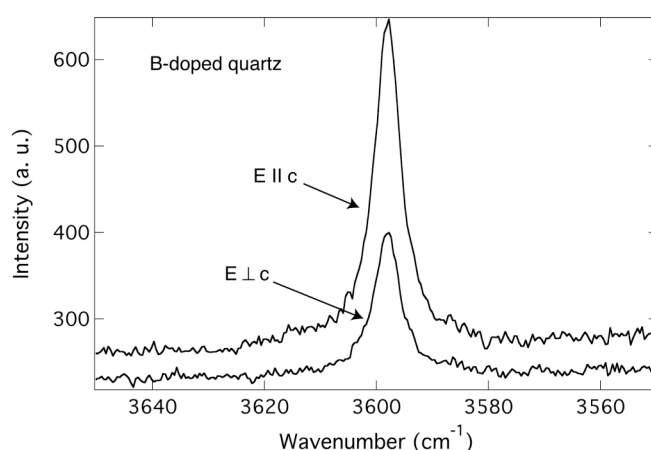


Figure 7. Polarized Raman spectra of the OH region in B-doped quartz. The strong pleochroic OH band displays the highest intensity parallel to the c-axis.

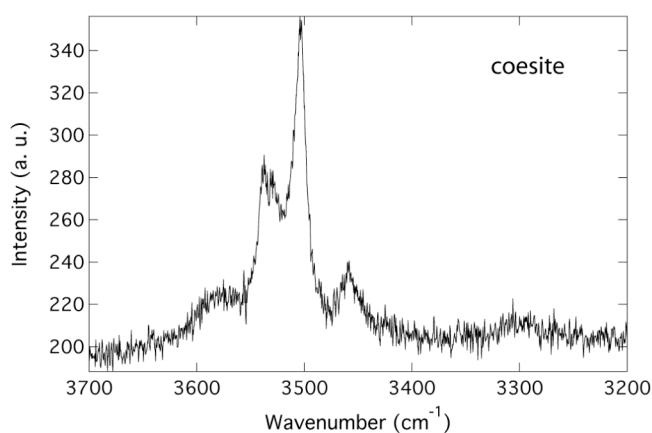


Figure 8. Unpolarized Raman spectrum of coesite (MA 009_a) that demonstrates the sufficient spectral resolution to use integral intensities for quantitative OH analyses. Moreover, all OH bands prior observed in IR spectra are present also in the Raman spectrum.

Water contents

The water contents of both natural samples and our run products were determined by applying either pp-scattering and/or confocal microRaman spectroscopy and/or SIMS (Tables 2 and 3). Depth profiles for HQV, SQT, SCO and Ud29 obtained using pp-scattering are shown in Figures 9 to 12. They confirm the feasibility of pp-scattering to separate surface hydrogen from inside hydrogen of a sample. For HQV with a hydrogen detection limit corresponding to 0.6 wt ppm H_2O , the detected inside hydrogen is corresponding to a value of 32 ± 8 wt ppm H_2O assuming all detected hydrogen bound in water and hydroxyl groups (error includes statistic and systematic uncertainties). For SQT a mean value of 2 analyses runs at 13 and 25 GeV was used. The calculated water content is 1.2 ± 0.8 ppm H_2O by weight. SCO holds < 0.8 wt ppm H_2O and for Ud29 a value of 98 ± 40 wt ppm H_2O was determined. A comparison of resulting water contents from the different quantification techniques is given in the Tables 2 and 3 and Figure 13.

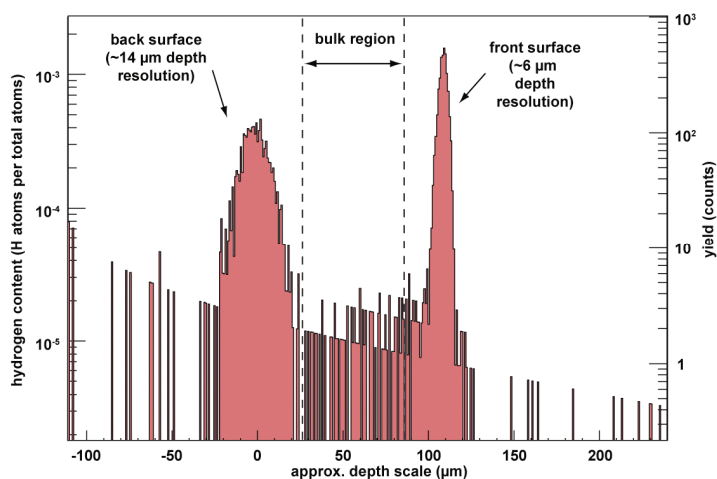


Figure 9. Depth profile of the hydrogen concentration (measured as H atoms per total atoms) in synthetic quartz SQT derived from pp-scattering. The depth scale is approximately calculated from the energy loss of the coincident proton pairs. Note the log on the y-scale and that the background is not constant due to depth-dependent efficiency correction and background tail. The depth resolution varies with depth as noted. Therefore the narrow surface hydrogen distribution is broadened and appears as two peaks in the front and back of the sample respectively (20% uncertainty). The spectrum demonstrates that it is possible to convincingly separate surface water from internal bulk hydrogen, and gives a background-corrected value of (2.7 ± 1.8) at ppm H corresponding to (1.2 ± 0.8) wt ppm H_2O .

Table 2. Raman and IR spectroscopic data for unpolarized H₂O analyses and comparison with independently determined H₂O concentrations (acquisition time 100 s / 5 accumulations).

| Sample | I _i (cps) | 1σ (cps) | I _{corr} (cps) | n | A _{itot} (IR) | Mean wavenumber (cm ⁻¹) ^{††} | H ₂ O (wt ppm) [†] | Absorption coefficient (l mol ⁻¹ _{H₂O} cm ⁻²) [§] | Independently determined H ₂ O (wt ppm) | |
|---------------------------|--|----------|-------------------------|----|------------------------|--|--|--|--|------------------------|
| | | | | | | | | | pp-scattering | SIMS [‡] |
| quartz: | | | | | | | | | | |
| SQT | n. d. | - | - | - | - | - | - | - | 1.2 (0.8) | - |
| HQV* | 10.80 | | 9.32 | 6 | 36 | 3375 | 38 | 64,000 | 32 (8) | - |
| SMT503_e | 56.56 | 22.75 | 48.79 | 12 | 202 | 3595 | 199 (79) | 69,000 | | |
| SMT503_d | 55.20 | 24.73 | 47.62 | 7 | 150 | 3595 | 194 (88) | 53,000 | | |
| SMT503_Z7 | 69.72 | 17.75 | 60.14 | 10 | 223 | 3595 | 246 (62) | 62,000 | | 429 (129) |
| SMT508_a | 16.84 | 3.53 | 14.53 | 11 | 61 | 3595 | 59 (12) | 70,000 | | |
| SMT508_b | 20.20 | 2.96 | 17.42 | 11 | 85 | 3595 | 71 (11) | 81,000 | | |
| SMT504_a | 25.10 | 7.84 | 21.65 | 11 | 123 | 3400 | 88 (27) | 62,000 | | 57 (17) |
| coesite: | | | | | | | | | | |
| WIM04_C1 | 42.52 | 7.64 | 33.51 | 10 | 422 | 3487 | 124 (22) | 209,000 | | 182 (55) |
| WIM04_C3 | 39.93 | 4.53 | 31.46 | 10 | 400 | 3439 | 116 (13) | 234,000 | | |
| MA009_a | 46.36 | 19.81 | 36.54 | 10 | 441 | 3463 | 135 (56) | 201,000 | | 207 (62) |
| MA061 | 53.63 | 7.65 | 42.27 | 12 | 520 | 3466 | 156 (04) | 205,000 | | 147 (44) |
| MA117 | 46.02 | 18.48 | 36.27 | 17 | 483 | 3512 | 134 (53) | 221,000 | | |
| olivine: | | | | | | | | | | |
| SCO | n.d. | - | - | - | 7.4(2) | - | - | - | < 0.8 | 1.2 – 1.6 [#] |
| Ud29* | 38.53 | 10.39 | 27.78 | 8 | 85 | 3548 | 92 (24) | 51,000 | 98 (40) ^{##} | 162(16) ^{§§} |
| MA020 | 187.95 | 123.99 | 135.49 | 10 | 309 | 3517 | 448 (283) | 38,000 | | |
| Notes: | | | | | | | | | | |
| I _i (cps) | – integrated intensity in the 3100-3750 cm ⁻¹ frequency range. | | | | | | | | | |
| 1σ (cps) | – 1 σ standard deviation of measured intensities. | | | | | | | | | |
| I _{corr} (cps) | – density (quartz : 2.65 g /cm ³ ; coesite 2.93 g /cm ³ , stishovite 4.30 g/cm ³ , olivine 3.27 g/cm ³) and reflectance corrected integrated intensity. | | | | | | | | | |
| n | – number of measurements. | | | | | | | | | |
| H ₂ O (wt ppm) | – water content calculated using the SD-6-53% glass (8,21 mol/l H ₂ O; I _{SD} = 13652.60 cps). | | | | | | | | | |
| * | – acquisition time 600 s and 25 accumulations (HQV) or 22 accumulations (Ud29). | | | | | | | | | |
| † | – error gives 1 sigma standard deviation. | | | | | | | | | |
| †† | – mean wavenumber gives are area-weighted average, calculated using the procedure according to Libowitzky & Rossman (1997). | | | | | | | | | |
| ‡ | – error estimated as 30 %. | | | | | | | | | |
| § | – absorption coefficient deduced from Raman and IR spectroscopy (rounded values). | | | | | | | | | |
| §§ | – data from SIMS according to Koch-Müller et al. (2006). | | | | | | | | | |
| # | – water concentration derived from IR spectroscopy using the calibration of Bell et al. (2003). | | | | | | | | | |
| n.d. | – not determined. | | | | | | | | | |
| ## | – corresponding ε-value = 46,000 l mol ⁻¹ _{H₂O} cm ⁻² . | | | | | | | | | |

Table 3. Raman and IR spectroscopic data for polarized H₂O analyses in quartz, stishovite and olivine.

| Sample | I _{tot} (cps) | I _{corr} (cps) | I _{SD} (cps) | n | Time (s) | Accumulations | A _{itot} (IR) | Mean wavenumber (cm ⁻¹) ^{††} | H ₂ O (wt ppm) | Absorption coefficient (Imol ⁻¹ _{H2O} cm ⁻²) [#] |
|---------------------------|--|-------------------------|-----------------------|---|----------|---------------|------------------------|---|---------------------------|---|
| quartz: | | | | | | | | | | |
| SMT503_e | 81.53 | 68.28 | 19381.59 | 4 | 100 | 5 | 202 | 3595 | 200 | 69,000 |
| stishovite: | | | | | | | | | | |
| MA118_c | 68.49 | 39.18 | 20253.99 | 4 | 300 | 5 | 676 | 3122 | 61 | 425,000 |
| MA034_10 | 212.61 | 121.62 | 19508.25 | 4 | 300 | 5 | 2200 | 3125 | 187 | 415,000 |
| MA034_8 | - | - | - | - | - | - | 773 | 3125 | 60 ^{##} | 539,000 ^{##} |
| olivine: | | | | | | | | | | |
| Ud29 | 61.38 | 44.25 | 19714.61 | 3 | 600 | 25 | 85 | 3548 | 97 | 48,000 [*] |
| <i>Notes:</i> | | | | | | | | | | |
| I _{tot} (cps) | – total integrated intensity in the 3100-3750 cm ⁻¹ frequency range. | | | | | | | | | |
| I _{corr} (cps) | – density (quartz: 2.65 g/cm ³ ; stishovite 4.3 g/cm ³ ; olivine 3.27 g/cm ³) and reflectance corrected integrated intensity. | | | | | | | | | |
| I _{SD} (cps) | – integrated intensity of the standard glass SD-6-53%. | | | | | | | | | |
| n | – number of measurements. | | | | | | | | | |
| Time (s) | – measuring time for one spectral window of 3 in the 2800 to 3980 cm ⁻¹ frequency range. | | | | | | | | | |
| Accumulations | – number of accumulations of each spectral window. | | | | | | | | | |
| H ₂ O (wt ppm) | – water content estimated using the SD-6-53% glass (8,21 mol/l H ₂ O). | | | | | | | | | |
| [#] | – absorption coefficient deduced from Raman and IR spectroscopy (rounded values). | | | | | | | | | |
| ^{##} | – deduced from SIMS data. | | | | | | | | | |
| ^{††} | – mean wavenumber gives area-weighted average, calculated using the procedure according to Libowitzky & Rossman (1997). | | | | | | | | | |
| [*] | – this value and ε-value derived from pp-scattering (46,000 Imol ⁻¹ _{H2O} cm ⁻²) lead to mean value of 47,000 Imol ⁻¹ _{H2O} cm ⁻² used for the discussion of our results. | | | | | | | | | |

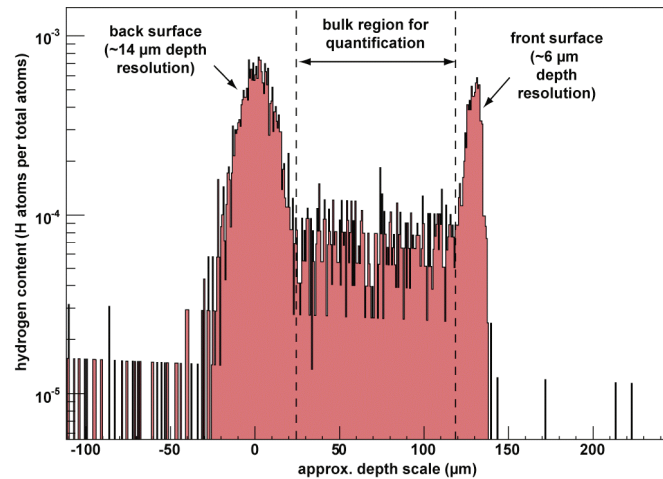


Figure 10. Depth profile of the hydrogen concentration in natural quartz HQV derived from pp-scattering. The bulk hydrogen content was derived from the marked region in order to avoid contribution from the surface, and gives a background-corrected value of (70 ± 17) at ppm H that corresponds to (32 ± 8) wt ppm H_2O .

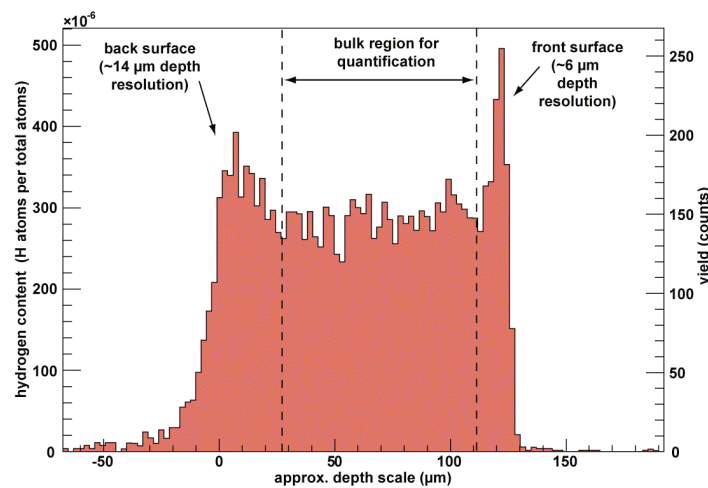


Figure 11. Depth profile of the hydrogen concentration in kimberlitic olivine Ud29 derived from pp-scattering. The bulk hydrogen content was derived from the marked region in order to avoid contribution from the surface, and gives a background-corrected value of (225 ± 92) at ppm H that corresponds to (98 ± 40) wt ppm H_2O .

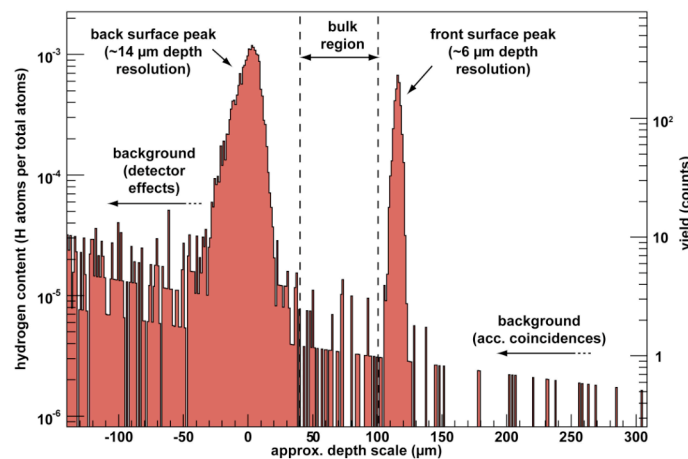


Figure 12. Depth profile of the hydrogen concentration in natural olivine SCO derived from pp-scattering. The bulk hydrogen content was derived from the marked region in order to avoid contribution from the surface, and gives a background-corrected value of < 2 at ppm H that corresponds < 0.8 wt ppm H_2O .

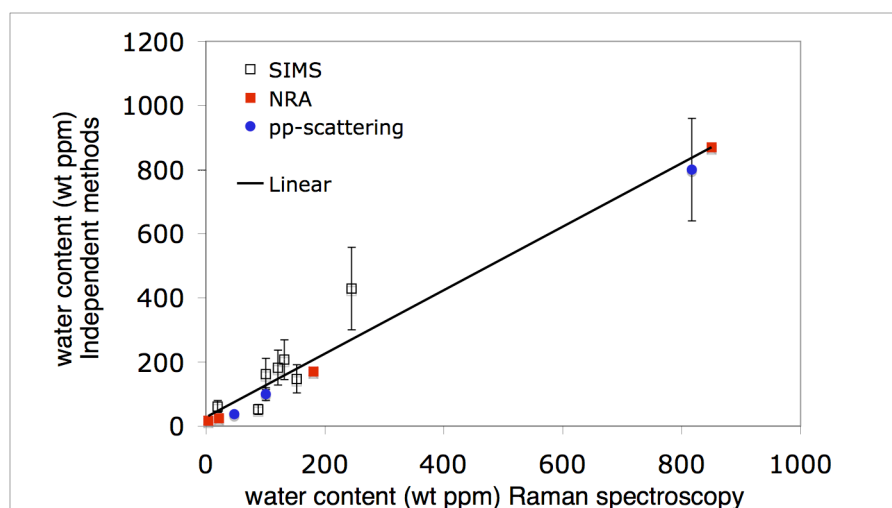


Figure 13. Comparison of all quantitative data from this study and in addition of garnets and quartz glass (taken from Thomas et al. submitted) deduced from Raman spectroscopy and 3 independent methods (cf. Tables 2 and 3; NRA data according to Maldener et al. 2003). The good linear correlation demonstrates the feasibility of Raman spectroscopy for the detection and quantification of trace water amounts in NAMs.

Absorption coefficients

Resulting water concentrations were used to calculate new mineral specific absorption coefficients. For olivine MA020 with the mean wavenumber of 3517 cm^{-1} we determined an ϵ -value of $38000 \pm 5000\text{ Imol}_{\text{H}_2\text{O}}^{-1}\text{ cm}^{-2}$ (Fig. 14 inset; Table 2). Quantification of olivine Ud29 with the mean wavenumber of 3548 cm^{-1} in contrast resulted in a ϵ -value of $47000 \pm 1000\text{ Imol}_{\text{H}_2\text{O}}^{-1}\text{ cm}^{-2}$, which is the mean ϵ -value deduced by averaging the data from pp-scattering and polarized Raman measurements (cf. Table 3). Data of SCO was not used to calculate an absorption coefficient, due to the potential high errors by quantification of IR spectra near to the detection limit with a low signal to noise ratio (cf. Fig. 6, Table 2). In case of the SiO_2 system it turns out that the magnitude of ϵ within one structure type is independent of the liable OH point defect and therewith the wavenumber of the observed band position. Consequently, one universal mean ϵ of $67000 \pm 8000\text{ Imol}_{\text{H}_2\text{O}}^{-1}\text{ cm}^{-2}$ could be determined for a suite of quartz samples with varying OH point defects (Fig. 14). In contrast, the absorption coefficient ϵ varies with the structure itself. For polymorphic coesite we calculated a different

ε -value of $214000 \pm 14000 \text{ l mol}^{-1}_{\text{H}_2\text{O}} \text{ cm}^{-2}$ (Fig. 14). Quantification data of stishovite resulted in an even higher mean value of $\varepsilon = 461000 \pm 68000 \text{ l mol}^{-1}_{\text{H}_2\text{O}} \text{ cm}^{-2}$ (Fig. 14).

The relative error of absorption coefficients is mainly determined by the error of the water concentration from all analyses performed in this study. The error of the water concentration in turn is influenced by multiple factors, as errors in thickness determination (IR analyses), small number of analyses (SIMS) or in general by errors of the crystal orientation, surface quality of the sample, vibrational spectra treatment (baseline, fits), statistical deviations within a certain sample suite or technical errors due to the quality of used polarizing and analyzing material for the spectroscopic methods used.

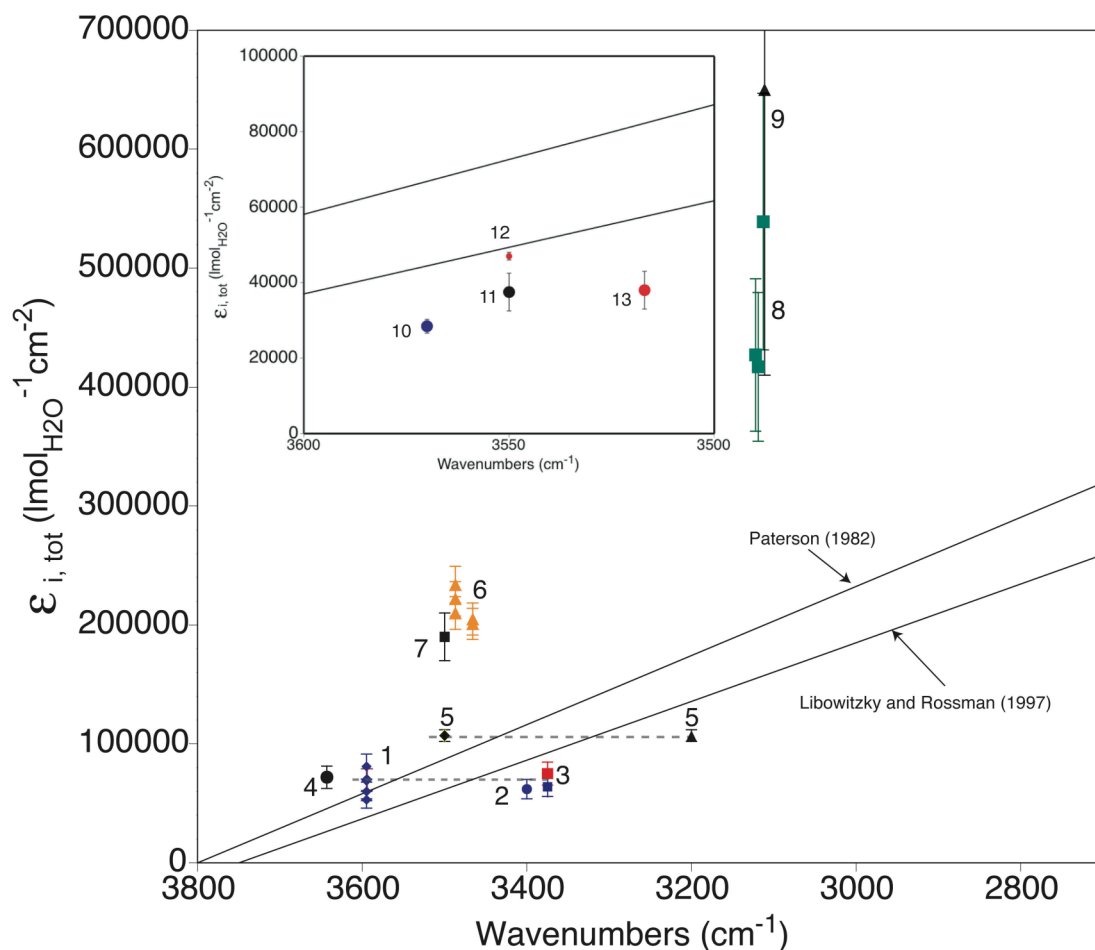


Figure 14. Comparison of mineral-specific absorption coefficients calculated in the context of the present study with those given in literature. 1) B-doped quartz, 2) Al-doped quartz, 3) natural quartz HQV, 4) synthetic quartz glass KG (Thomas et al. submitted), 5) feldspar data according to Johnson and Rossman (2003), 6) synthetic coesites (this study), 7) coesite (Koch-Müller et al. 2001), 8) synthetic stishovite (this study), 9) stishovite (Pawley et al. 1993). The inset gives a magnified section of the region 3600 to 3500 cm^{-1} with: 10) olivine (Bell et al. 1995), 11) olivine (Koch-Müller et al. 2006), 12) Ud29 (this study), 13) MA020 (this study). Differences in errors given are due to different analytical techniques and/or low statistics (e.g., 12 or 8; cf. text).

Discussion

Water contents

Water contents determined with three independent methods are in good agreement (cf. Fig. 13, Tables 2 and 3) and thus verify the usage of Raman spectroscopy with the “Comparator Technique” also for anisotropic single-crystals as well as for ppm-level water ranges. In general, SIMS values are slightly higher than values derived from pp-scattering and Raman analyses. Reasons for that may be errors (estimated as 30 %) due to the small number of analyses points, limitations by tiny crystal sizes or due to surface hydrogen that is brought into the sampling volume. However, major errors due to matrix differences can be excluded in our study as we used quartz crystals as standards.

Water contents determined for our natural **quartz** are consistent with prior reported values, typically ranging from 0 up to some tens of wt ppm H₂O in natural specimens to even 8000 wt ppm H₂O as fluid inclusions (Johnson 2006). In contrast, water contents in synthetic quartz, mainly charge-balanced by various trace elements, are in the order of some hundreds of ppm H₂O by weight and may indicate that water solubility increases with pressure. This may imply that also natural quartz, when transported to high-pressure regions, e.g., subduction zones, might incorporate a higher quantity of water. Water contents in synthetic **coesite** studied here are in excellent agreement to prior data (Koch-Müller et al. 2001). First evidence for water in natural coesite gave a study by Koch-Müller et al. (2003). The latter authors reported ~ 135 ppm H₂O by weight in coesite inclusions in a diamond. The amount of water in stishovite is predominantly related to the Al-content. The water concentration in synthetic **stishovite** to date has been reported to range between 3 ppm by weight for Al-free stishovite (Bolfan-Casanova et al. 2000; Bromiley et al. 2006; Litasov et al. 2007) to about 3000 wt ppm H₂O in Al-stishovite (Litasov et al. 2007). As the latter data is primarily based on the calibration of Paterson (1982) it is not comparable with our results. Bromiley et al. (2006) noted that the concentration of Al in their samples is 4 to 8 times higher than the H concentration, which could be explained by the presence of oxygen vacancies to provide

charge-balance. Kimberlitic *olivine* contains according to literature the highest water contents of about 400 wt ppm, whereas olivine from basaltic flows such as SCO is very dry (Miller et al. 1987; Bai and Kohlstedt 1993; Beran and Libowitzky 2006). All that is in good agreement with our data. Kimberlitic olivine Ud29 holds higher amounts of water than SCO. However, the calculated absolute concentration for Ud29 is slightly smaller than previously determined by SIMS analyses (Koch-Müller et al. 2006). This fact may be due to systematical errors in SIMS analyses, e.g., due to matrix differences between olivine and garnets that were used as standards for the latter study. The value for olivine SCO determined from IR measurements in combination with the calibration of Bell et al. (2003) results in very low contents of 1.2 to 1.6 wt ppm H₂O and thus is in good agreement with the data obtained by pp-scattering (< 0.8 wt ppm H₂O). Slightly higher values for SCO from IR spectra may be explained by potential high errors by low background to noise ratios considering very low water concentrations (near the detection limit) and possible surface water contaminations. However, our data are also consistent with data for SCO of 0.2 – 0.7 wt ppm H₂O (Miller et al. 1987) and 0.2 wt ppm H₂O (Mackwell et al. 1985), when we consider that both studies used the calibration of Paterson (1982) which is known to give a 4 times lower concentration compared to our results.

Absorption coefficients

The approach of this work is to investigate isolated OH defects within one mineral group to study the frequency dependence of the absorption coefficient. Results on a series of quartz demonstrate that ϵ is independent of or rather less susceptible to the responsible OH point defect within one structure. Johnson and Rossman (2003) reported similar results for a suite of natural plagioclase (mean OH band frequency 3200 cm⁻¹) and feldspar samples (mean OH band frequency 3500 cm⁻¹). Based on IR studies and ¹H MAS NMR the latter authors derived a unique absorption coefficient of $107000 \pm 5000 \text{ Imol}_{\text{H}_2\text{O}}^{-1} \text{ cm}^{-2}$. Brunner and co-authors (1961) predicted the first ϵ -value for natural quartz (see below), followed by Kats (1962), who

reported a value for synthetic quartz with OH bands at 3315, 3370 and 3436 cm^{-1} . However, according to Paterson (1982) the early quartz calibrations are based on unpolarized spectra and lack in accurate spectral fitting. Therefore, high errors may be expected, as Libowitzky and Rossman (1997) state, that in case of anisotropic crystals it is necessary to use polarized measurements taken parallel to each crystallographic axis to determine correct total absorbance values as basis for water quantification. Paterson (1982) reviewed the calibrations of Brunner et al. (1961) and Kats (1962) and predicts $90000 \text{ l mol}_{\text{H}_2\text{O}}^{-1} \text{ cm}^{-2}$ and $84000 \text{ l mol}_{\text{H}_2\text{O}}^{-1} \text{ cm}^{-2}$ as respective ϵ -values, which are higher than our ϵ -value ($67000 \text{ l mol}_{\text{H}_2\text{O}}^{-1} \text{ cm}^{-2}$). Since we determined our absorption coefficient with independent methods as pp-scattering and Raman spectroscopy and considered the anisotropic orientation of the absorbers (OH), we suggest the new absorption coefficient to be more precise for future quantitative IR studies of quartz. The structural water content in synthetic and natural quartz can now be determined with polarized IR measurements using $\epsilon = 67000 \pm 8000 \text{ l mol}_{\text{H}_2\text{O}}^{-1} \text{ cm}^{-2}$ without the need for independent quantification methods.

Compared to quartz the absorption coefficients for the denser polymorphs coesite and stishovite are much higher. The ϵ -value derived for coesite studied here ($214000 \text{ l mol}_{\text{H}_2\text{O}}^{-1} \text{ cm}^{-2}$) is in excellent agreement with an earlier predicted absorption coefficient of $190000 \pm 30000 \text{ l mol}_{\text{H}_2\text{O}}^{-1} \text{ cm}^{-2}$ (Koch-Müller et al. 2001). Pawley et al. (1993) estimated for stishovite an absorption coefficient of $652000 \pm 240000 \text{ l mol}_{\text{H}_2\text{O}}^{-1} \text{ cm}^{-2}$ (the value of the authors was multiplied by two to give the latter unit), which is 4 times higher than the value predicted by the general calibrations trend of Paterson (1982). The ϵ -value given in Pawley et al. (1993) is slightly higher but still rather similar to our value ($461000 \text{ l mol}_{\text{H}_2\text{O}}^{-1} \text{ cm}^{-2} \pm 68000 \text{ l mol}_{\text{H}_2\text{O}}^{-1} \text{ cm}^{-2}$). Yet, the latter authors used unpolarized IR spectra and an orientation factor of 2 as suggested by Paterson (1982). Moreover, their absorption coefficient for H-stishovite is based on SIMS analyses conducted on a D-stishovite, which is debatable, as, e.g., Koch-Müller et al. (2003) obtain for D-coesite ($154000 \pm 20000 \text{ l mol}_{\text{H}_2\text{O}}^{-1} \text{ cm}^{-2}$) a smaller absorption

coefficient than for H coesite. Therefore, we consider our new value ($461000 \pm 68000 \text{ l mol}^{-1}_{\text{H}_2\text{O}} \text{ cm}^{-2}$) more reliable, as it is based exclusively on polarized measurements and is moreover cross-referenced by our SIMS data of OH in stishovite.

Bell et al. (2003) determined for olivine with the mean wavenumber of 3570 cm^{-1} an ϵ -value of $28450 \pm 1830 \text{ l mol}^{-1}_{\text{H}_2\text{O}} \text{ cm}^{-2}$. A slightly higher value of $37500 \pm 5000 \text{ l mol}^{-1}_{\text{H}_2\text{O}} \text{ cm}^{-2}$ has been suggested for olivine with the mean wavenumber of 3548 cm^{-1} by Koch-Müller et al. (2006). Both absorption coefficients derived from our study for two different mean OH band frequencies (3517 cm^{-1} : $38000 \pm 5000 \text{ l mol}^{-1}_{\text{H}_2\text{O}} \text{ cm}^{-2}$ and 3548 cm^{-1} : $47000 \pm 1000 \text{ l mol}^{-1}_{\text{H}_2\text{O}} \text{ cm}^{-2}$) are higher than the predicted value of Bell et al. (2003) but similar to the absorption coefficient given in Koch-Müller et al. (2006).

In conclusion, we present examples for NAMs where the negative correlation between absorption coefficient and OH band position does not hold. Deviations off the linear calibration trends proposed by Paterson (1982) and Libowitzky and Rossman (1997) were also noted by, e.g., Bell et al. (1995), Hösch (1999) and Libowitzky and Rossman (1997) for garnets and by Maldener et al. (2001) for rutile and cassiterite. Our results for the SiO_2 polymorphs are consistent with prior studies of Koch-Müller et al. (2003) and Pawley et al. (1993). They clearly imply that the structure might have a major influence on the absorption coefficient and therewith on the intensity of the IR absorption. Libowitzky and Rossman (1997) supposed that spectroscopic properties of OH defects in NAMs might differ from those of stoichiometric components in hydrous minerals. However, the exact reason for the discrepancies is still unknown. It is difficult to explain the observed differences as the magnitude of ϵ is strongly dependent on the strength of the dipole moment and the hydrogen bond. But both are not known for NAMs as the exact geometry of the responsible defects remains unknown. In general, substitution or vacancy would lead to deformation (e.g., expansion or compression) of the involved polyhedron, whether tetrahedron or octahedron (e.g., Smyth et al. 1995; Lager et al. 1989). As a consequence, the O...O distances would

increase too. Hence, we do not know the exact O...O distances, neither for stishovite nor coesite or quartz. Promising methods to trace such hydrogen sites are, e.g., neutron-diffraction or computational modeling.

For a successive discussion of our results, it is necessary to recall the basis of the common IR calibrations for hydrous compounds, which is a negative correlation between the molar absorption coefficient (ε) and the mean wavenumber of the corresponding OH band pattern.

The **OH band position** depends on the magnitude of the corresponding O1-H...O2 distances and herewith on the hydrogen bond (H...O2) which is primarily defined by the attractive force of the acceptor oxygen atom (O2) on the proton, which somewhat pulls it away from the donor (O1) (Libowitzky and Beran, 2004). The OH stretching wavenumbers are observed at 3700-3200 cm^{-1} for weak H bonds, at 3200-1600 cm^{-1} for strong H bonds, and at 1600 to 700 cm^{-1} for very strong H bonds (Libowitzky 1999). However, according to Kubicki et al. (1993) the dominant factor affecting OH band position is the dipole (O1-H), which in turn is controlled by H-bonding if the H...O2 distance is smaller than 2 Å ($< 3750 \text{ cm}^{-1}$). He also pointed out that multiple factors may influence the OH band position. Given the next nearest structure environment around a vibrating OH group, A-M-O1-H...O2, not only O...O distances but also O...O angles, multiple hydrogen bonds and ionic substitutions at the metal cation (M) or anion positions (A) can have an effect. The **band intensity** in the IR spectrum is directly proportional to the concentration of the excited species in the sample and further depends on the magnitude and change of the dipole moment during the vibration (e.g., Wilson et al. 1955; Libowitzky 1999). The magnitude of the dipole moment depends on the distances and charge differences of the two ions (e.g., O^{2-} , H^+) involved. It increases with rising distances of the ions. As a result, band intensity and therewith also the absorption coefficient ε depend on changing atomic distances and charges during the vibration. In general, at a constant OH concentration, band intensity increases (ε increases) with decreasing band frequency. Given the observed OH features obtained in this study O1-H and H...O2 distances should influence our band positions and intensities. If intending to

understand our results, we have to separately look at the structures and at the literature available on hydration mechanisms suggested for them.

Quartz, coesite and stishovite

In the α -**quartz** structure SiO_4 tetrahedra form trigonal helices. The SiO_4 tetrahedra are not regular. The structure has neither mirror planes nor centers of symmetry. The point symmetry 2 of Si leads to two different Si-O bond distances, 1.6104 Å and 1.6074 Å with the four oxygens coordinating Si being pairwise equivalent. The O-O bond distances are 2.6148, 2.6307, 2.6422 Å (2x) (Le Page and Donnay 1976).

Hydrogen incorporation in quartz has been studied since the middle of the 20th century. The sharp absorption bands in the OH region around 3400 cm^{-1} in the IR spectra of quartz have been assigned to hydrogen incorporation associated with the coupled substitution of trivalent Al by tetravalent Si, which is believed to be the dominating intrinsic hydration mechanism (e.g., Kats 1962). Pankrath (1991) showed that H may be bound to O(1), O(2), O(4) or O(5), where the first two oxygens are related to the shorter Si-O distance and the latter two oxygens to the longer ones (see above). The author further demonstrated, that the OH bands at 3380, 3365 and 3305 cm^{-1} are directly correlated with a non-uniform substitution of tetravalent Si by trivalent Al on the three symmetrically equivalent Si sites in the quartz structure. However, a definite assignation to distinct defects has not been possible so far.

We expect the same incorporation mechanisms dominating in our natural and Al-doped quartz samples, where charge-balancing protons form different OH groups and cause therewith several OH vibrations, giving rise to a number of OH bands covering a broad frequency range. However, for B-doped quartz there exists no incorporation model yet. We observe for our Al-doped quartz the OH band pattern at a smaller mean wavenumber (3400 cm^{-1}) than for B-doped quartz (3600 cm^{-1}). Boron has a higher electronegativity (2.04) than Al (1.61), and taking into account electronegativity/band position correlations (e.g., Strens 1974) the dipole should be weaker than that of Al (cf. Libowitzky and Beran 2004; Koch-Müller et al.

1997). However, this is not the case and might be explained by the smaller mass and ionic radius of B (0.23 Å) compared to Al (0.57 Å), that leads to the smaller attraction of boron as donor coupled with a small effect on the dipole strength, compared to Al as donor atom, which weakens the dipole to a higher degree. From the OH band position according to Libowitzky (1999) one expects a stronger OH dipole in B-doped quartz compared to Al-doped quartz. However, both defects show the same ε -value, i.e., the change of the dipole moment during the vibration should be more or less the same. That is surprising, as the absorption intensity depends on the magnitude of the dipole moment change (see above). Possibly, O-H...O angles have a stronger influence in these special cases. Optionally, bifurcated H bonds might play a role in case of the Al-based defect, where the attractive influence of the H bond acceptor is attenuated if the H...O distance in a bent H bond is longer (as a consequence of the bent geometry) than in a straight H bond (Kubicki et al. 1993; Libowitzky and Beran 2004). However, the observation of similar properties of B-doped and Al-doped quartz may further be an implication that H incorporation mechanism coupled to the B-based defect is analogue to that of the Al-based defect.

The **coesite** structure is monoclinic with five distinct oxygen sites in the structure. It contains rings of SiO₄ tetrahedra that form chains in the b-direction and a second set of chains in the c-direction. There are two distinct Si atoms. The Si(1)-O bond distance is 1.6014 Å and the Si(2)-O distance is 1.6124 Å. The oxygen atoms are bonded to two Si atoms. O-O distances associated with Si(1) are 2.6133 Å, 2.6327 Å and 2.6342 Å. O-O distances associated with Si(2) are 2.6226 Å and 2.6287 Å and 2.6369 Å (values according to Gibbs et al. 1977).

Koch-Müller et al. (2001, 2003) report the hydrogarnet substitution associated with the Si(1) to be the dominant protonation mechanism in coesite besides minor contributions of B or Al substitutions. From their data Koch-Müller et al. (2001, 2003) predict incorporation models where the oxygens O2, O3, O4 and O5 are involved in the hydrogarnet defect, associated with a vacant Si (1) tetrahedron. Deon et al. (submitted) report that, as pressure and

temperature increase, the coesite structure prefers to incorporate H via the B based defect, which might be energetically favorable, as the latter defect requires a smaller volume than the hydrogarnet substitution (see below). The authors propose a model for the hydrogen incorporation via the B-based defect and suggest O1, O4, and O5 as possible proton donor sites.

In our study we obtain for coesite more or less the same ϵ -value for both, the hydrogarnet- and the boron based defect. However, as mean band positions caused by both incorporation mechanisms are quite similar, we cannot deduce from our results if there exists a unique ϵ -value over a broader frequency range for coesite, as observed for quartz. Quite surprising is, that such different kinds of defects lead to a nearly equivalent ϵ -value. Consequently, subsequent studies of coesite should include the study of isolated hydrogarnet type 2 defects and its effects on ϵ -value to evaluate the frequency dependency of ϵ for a broader frequency range.

The increase of ϵ from quartz ($67000 \text{ l mol}^{-1}_{\text{H}_2\text{O}} \text{ cm}^{-2}$) to coesite ($214000 \text{ l mol}^{-1}_{\text{H}_2\text{O}} \text{ cm}^{-2}$) might be explained with the increasing density of the structure that leads to smaller mean O-O distances comparing quartz (2.6325 Å) with coesite (O...O distances associated with Si(1) involved in hydration: 2.6267 Å), therewith simultaneously to an strengthening of the H bond associated with weakening of the OH dipole bonding and eventually to an increase of the absorption coefficient ϵ . However, O...O distances differences are rather small in the pure structures of the both minerals. Hence, for a demonstration of the latter argument exact H positions and O...O distances for the defect structures are required.

The **stishovite** structure is tetragonal with all Si cations in octahedral coordination by oxygens. Each oxygen atom is threefoldly coordinated by Si atoms. The structure consists of bands of edge-sharing octahedra in the c-direction. All oxygens in the structure are equivalent. The Si-O bond distances in pure stishovite are 1.7572 Å (equatorial) and 1.8087

Å (axial). The O-O distances are 2.5217 Å, 2.6655 Å and 2.2903 Å, with the latter bond distance belonging to the edge-sharing octahedra and being unusual short (Hill et al. 1983). The amount of hydrogen in stishovite is generally related to the Al content, with H dominantly incorporated via the substitution of Si^{4+} by Al^{3+} . Gibbs et al. (2004) showed that the substitution of Si by Al is consistent with increasing the cell volume about $\sim 10\%$ and distortion of the octahedra. This is exactly what is known for H-bearing aluminous stishovite (Smyth et al. 1995). According to models for stishovite (Smyth et al. 1995; Gibbs et al. 2004) H is located close to one of the shared O-O edges of the SiO_6 octahedra. With respect to the strong pleochroism observed in the IR spectra it should be located perpendicular to the crystallographic c-axis. Smyth et al. (1995) suggest H at the (0.42, 0.5, 0) position what implies protonation close to the unusual short O-O distance in the structure. In contrast, Gibbs et al. (2004) predict from computational modeling (0.44, 0.12, 0) as H site. Again, the exact protonation mechanism and thus the H positions are uncertain.

According to studies of Bromiley et al. (2006) and Litasov et al. (2007) the reason for the occurrence of the band at 3111-3134 cm^{-1} in both, Al-free and Al-stishovite might be related to H associated with an octahedral vacancy without charge balancing by Al^{3+} , namely an isolated proton. Another explanation would be that very low concentrations of water in stishovite (typical for Al-free stishovite) are charge-balanced even by impurities of Al^{3+} in the starting reagents, as reported by Bromiley et al. (2006) based on the purity of their SiO_2 starting oxide that contained 8.2 wt ppm Al.

We observe similar OH bands in both our Al-free and Al-bearing stishovite, which is in good agreement with prior studies (see above). The OH band positions are consistent with moderate to strong H bonding (Libowitzky 1999). According to our results Al-free and Al-doped stishovite have similar ϵ -values. That might indicate an uniform H incorporation mechanism. Nevertheless, to make a more general conclusion with respect to the ϵ -value for the stishovite structure, potential effects due to the substitution of other trivalent ions on the absorption coefficient should be considered in subsequent studies. Moreover, the ϵ -value for

stishovite studied here is larger by a factor of 2.15 compared to that obtained for coesite and by a factor of 6.9 compared to quartz. The cause of this may be linked to the structure. The structure of stishovite is much denser compared to coesite, accompanied by a change from fourfold to sixfold coordination of the Si atom. The mean O-O distance in stishovite inhibits the smallest value of the three polymorphs (2.4925 Å) studied. The here observed structure dependence of the absorption coefficient might be explained by the change from tetrahedral to octahedral Si-coordination. Mean O...O distances significantly decrease from coesite (2.6267 Å) to stishovite (2.4925 Å) which, as H bonding increases, might explain the decrease of the wavenumber of the OH bands. Moreover, as the intensity is proportional to the dipole moment change (distances and charges) the shorter O...O distances should strengthen the hydrogen bond, weaken the dipole and thus should lead to an increase of the band intensity. Furthermore, the presence of a stronger H bond affects the dipole moment of the OH group in a different way, as H atom electron density can be distributed between the two involved oxygen atoms and charges of both oxygens and hydrogen change (see Kubicki et al. 1993). This may be an explanation for the increase of the magnitude of the absorption coefficient of coesite compared to stishovite.

Generally, for NAMs further factors as O-H...O angles should be taken into account in subsequent discussions. Moreover, effects of chemical composition on the OH frequencies cannot be ruled out, as compositional changes are not completely isolated from structural effects (e.g., Kubicki et al. 1993). For example we obtained for GeO₂ (in prep.) crystallizing in the rutile structure (r-GeO₂) with the mean OH band position at 3208 cm⁻¹ a mean ϵ -value of $141000 \pm 25000 \text{ l mol}^{-1}_{\text{H}_2\text{O}} \text{ cm}^{-2}$, plotting in between both prior suggested calibration lines (Libowitzky and Rossman 1997; Paterson 1982). Though holding the same tetragonal structure the O...O bond distances (2.862, 2.670 Å, Ge-O 1.905 and 1.870 Å) are larger than those known for stishovite (see above), which can be explained by the larger ionic radius of Ge as metal cation compared with the smaller Si. Based on the correlation between O...O distances and OH band frequency this should lead to a slightly higher mean wavenumber,

and this is exactly what we observe comparing the mean band position of stishovite (3124 cm^{-1}) and GeO_2 (3208 cm^{-1}). A smaller ε -value for $r\text{-GeO}_2$ compared to stishovite commensurates with a smaller magnitude of the dipole moment and its change during the OH vibration, which correlates with the large O...O distances in $r\text{-GeO}_2$ compared to stishovite.

Olivine

For orthorhombic olivine, band assignments to given OH point defects, whether Si- and/or M1, M2 vacancies, are still under debate (cf. Beran and Libowitzky 2006). Koch-Müller et al. (2006) suggest that their absorption bands due to group I bands are associated with vacant Si and M1 sites. They propose two possible incorporation mechanisms that involve either H1 bound to O1 and bifurcated hydrogen bonding to the O2 or O3 oxygen or H2 bound to O2 with bifurcated hydrogen bonding to O1 and O3. B- or Al-substitutions are not discussed in the majority of the literature, as they seem to play only a minor role in olivines (Sykes et al. 1994). Besides the latter defects, it is known that olivine may contain inclusions of hydrous minerals that lead to OH bands in the OH region (Beran and Libowitzky 2006).

All olivines studied here show similar OH band patterns (group I), hence, similar defects should be involved as causes for the OH vibrations (M1 and Si vacancies). We obtain quite similar ε -values for both olivines studied ($38000\text{ l mol}_{\text{H}_2\text{O}}^{-1}\text{ cm}^{-2}$ and $47000\text{ l mol}_{\text{H}_2\text{O}}^{-1}\text{ cm}^{-2}$), although both display a different mean OH band position. Taking into account previous studies (Bell et al. 1995; Koch-Müller et al. 2006) it seems unlikely to suggest a linear wavenumber dependent correlation for olivine, where ε increases with decreasing wavenumber. Within given errors a unique absorption coefficient for olivine is indicated analogue to our observations for quartz (cf. Fig. 14). However, from our results and considering potential errors due to low statistics no clear trend can be evaluated. As we used for our study only the mean wavenumber covering a very broad region, we cannot unambiguously tell if there is a frequency dependence of ε or not. Subsequent studies of

olivine, preferentially displaying OH bands at lower frequencies around 3200 cm^{-1} , could help to address this issue and are in preparation.

Our results confirm suggestions, that using a mineral-specific calibration prevents the misinterpretation of water concentrations and absorption coefficients, especially in the case of dense high-pressure silicates, what in turn becomes important to model the earth's deep water cycle. Increase of ε from quartz to coesite to stishovite might be explained by the decreasing O...O distances. Moreover, we present a routine to quantify water contents in anisotropic minerals with Raman spectroscopy. This technique has major advantages in terms of non-destructive analysis of small-sized synthesis products or also thin- or thick sections of minerals.

Acknowledgements

The authors wish to thank B. Wunder, G. Berger, M. Kreplin, R. Schulz, H. Steigert, U. Schade and M. Schmidt for help with the experiments, sample preparation, X-ray diffraction and synchrotron IR measurements. C. Schmidt and W. Heinrich are thanked for helpful comments and discussions. We are grateful to W. van Westrenen who kindly provided sample WIM04.

References

- Arredondo, E.H. and Rossman, G.R. (2002) Feasibility of determining the quantitative OH content of garnets with Raman spectroscopy. *American Mineralogist*, 87, 307-311.
- Aubaud, C., Withers, A.C., Hirschmann, M.M., Guan, Y., Leshin, L.A., Mackwell, S.J., and Bell, D.R. (2007) Intercalibration of FTIR and SIMS for hydrogen measurements in glasses and nominally anhydrous minerals. *American Mineralogist*, 92, 811-828.
- Bai, Q. and Kohlstedt, D.L. (1993) Effects of chemical environment on the solubility and incorporation mechanism for hydrogen in olivine. *Physics and Chemistry of Minerals*, 19, 460-471.
- Behrens, H., Roux, J., Neuville, D.R., and Siemann, M. (2006) Quantification of dissolved H₂O in silicate glasses using confocal microRaman spectroscopy. *Chemical Geology*, 229, 96-112.

- Bell, D.R., Ihinger, P.D., and Rossman, G.R. (1995) Quantitative analysis of trace OH in garnet and pyroxene. *American Mineralogist*, 80, 465-474.
- Bell, D.R., Rossman, G.R., Maldener, J., Endisch, D., and Rauch, F. (2003) Hydroxide in olivine: a quantitative determination of the absolute amount and calibration of the IR spectrum. *Journal of Geophysical Research*, 108(B2), 2105-2113.
- Bell, D.R., Rossman, G.R., and Moore, R.O. (2004) Abundance and partitioning of OH in a high-pressure magmatic system: Megacrysts from the Monastery kimberlite, South Africa. *Journal of Petrology*, 45(8), 1539-1564.
- Beran, A. and Libowitzky, E. (2006) Water in natural mantle minerals II: olivine, garnet and accessory minerals. In H. Keppler and J.R. Smyth, Eds., *Water in nominally anhydrous minerals*, 478 p. Mineralogical Society of America, Chantilly.
- Bolfan-Casanova, N., Keppler, H., and Rubie, D.C. (2000) Water partitioning between nominally anhydrous minerals in the MgO-SiO₂-H₂O system up to 24 GPa: implications for the distribution of water in the earth's mantle. *Earth and Planetary Science Letters*, 182, 209-221.
- Boyd, F.R. and England, J.L. (1960) Apparatus for phase-equilibrium measurements at pressures up to 50 kbar and temperatures up to 1740 °C. *Journal of Geophysical Research*, 65, 741-748.
- Bromiley, G.D., Bromiley, F.A., and Bromiley, D.W. (2006) On the mechanisms for H and Al incorporation in stishovite. *Physics and Chemistry of Minerals*, 33, 613-621.
- Brunner, G.O., Wondratschek, H., and Laves, F. (1961) Ultrarotuntersuchung über den Einbau von H in natürlichem Quarz. *Zeitschrift für Elektrochemie*, 65, 735-750.
- Chabiron, A., Pironon, J., and Massare, D. (2004) Characterization of water in synthetic rhyolitic glasses and natural melt inclusions by Raman spectroscopy. *Contributions to Mineralogy and Petrology*, 146, 485-492.
- Chakraborty, D. and Lehmann, G. (1976) On the structures and orientations of hydrogen defects in natural and synthetic quartz crystals. *Physica status solidi, A*, 34, 467-474.
- Cho, H. and Rossman, G.R. (1993) Single-crystal NMR studies of low-concentration hydrous species in minerals: grossular garnet. *American Mineralogist*, 78, 1149-1164.
- Deloule, E., Paillat, O., Pichavant, M., and Scaillet, B. (1995) Ion microprobe determination of water in silicate glasses: methods and applications. *Chemical geology*, 125, 19-28.
- Di Muro, A., Giordano, D., Villemant, B., Montagnac, G., and Romano, C. (2006a) Influence of composition and thermal history of volcanic glasses on water content determination by microRaman spectrometry. *Applied Geochemistry*, 21, 802-812.
- Di Muro, A., Villemant, B., Montagnac, G., Scaillet, B., and Reynard, B. (2006b) Quantification of water content and speciation in natural silicic glasses (phonolites, dacites, rhyolites) by confocal microRaman spectrometry. *Geochimica et Cosmochimica Acta*, 70, 2868-2884.

- Everall, N.J. (2000) Modeling and measuring the effect of refraction on the depth resolution of confocal raman microscopy. *Applied Spectroscopy*, 54, 773-782.
- Gibbs, G., Cox, D., and Ross, N. (2004) A modeling of the structure and favourable H-docking sites and defects for the high-pressure silica polymorph stishovite. *Physics and Chemistry of Minerals*, 31, 232-239.
- Hammer, V.M.F., Beran, A., Endisch, D., and Rauch, F. (1996) OH concentrations in natural titanites determined by FTIR spectroscopy and nuclear reaction analysis. *European Journal of Mineralogy*, 8, 281-288.
- Hauri, E., Wang, J., Dixon, J.E., King, P.L., Mandeville, C., and Newman, S. (2002) SIMS analysis of volatiles in volcanic glasses, 1, calibration, matrix effects and comparisons with FTIR. *Chemical geology*, 183, 99-114.
- Hervig, R.L., Stanton, T.R., and Williams, P. (1987) Ion probe microanalyses of hydrogen in glasses and minerals. *EOS*, 68, 441.
- Hösch, A. (1999) Schwingungsspektroskopie von OH führenden Defekten in Granat. 168 p. Dissertation.
- Huang, X., Xu, Y., and Karato, S. (2005) Water content in the transition zone from electrical conductivity of wadsleyite and ringwoodite. *Nature*, 434, 746-749.
- Johnson, E.A. and Rossman, G.R. (2003) The concentration and speciation of hydrogen in feldspars using FTIR and ^1H MAS NMR spectroscopy. *American Mineralogist*, 88, 901-911.
- Johnson, E.A. (2006) Water in nominally anhydrous crustal minerals: speciation, concentration, and geologic significance. In H. Keppler and J.R. Smyth, Eds., *Water in nominally anhydrous minerals. Reviews in Mineralogy and Geochemistry*, 62, 117-154, Mineralogical Society of America, Chantilly.
- Karamelas, S., Fritsch, E., Zorba, T., Paraskevopoulos, K.M., and Sklavounos, S. (2005) Distinguishing natural from synthetic amethyst: the presence and shape of the 3595 cm^{-1} peak. *Mineralogy and Petrology*, 85, 45-52.
- Karato, S. (1990) The role of hydrogen in the electrical conductivity of the upper mantle. *Nature*, 347, 272-273.
- Kats, A. (1962) Hydrogen in alpha quartz. Phillips Research Report, 17, 133-279.
- Kats, A., Haven, Y., and Stevels, J.M. (1962) Hydroxyl groups in α -quartz. *Physics and Chemistry of Glasses*, 3, 69-75.
- Keppler, H. and Rauch, F. (2000) Water solubility in nominally anhydrous minerals measured by FTIR and ^1H MAS NMR spectroscopy: the effect of sample preparation. *Physics and Chemistry of Minerals*, 27, 371-376.
- Koch-Müller, M. and Langer, K. (1998) Quantitative IR spectroscopic determination of the component H_2O in staurolite. *European Journal of Mineralogy*, 10, 1267-1273.
- Koch-Müller, M., Matsyuk, S.S., Rhede, D., Wirth, R., and Khisina, N. (2006) Hydroxyl in mantle olivine xenocrysts from the Udachnaya kimberlite pipe. *Physics and Chemistry of Minerals*, 33, 276-287.
- Koch-Müller, M., Fei, Y., Hauri, E., and Liu, Z. (2001) Location and quantitative analysis of OH in coesite. *Physics and Chemistry of Minerals*, 28, 693-705.

- Koch-Müller, M., Dera, P., Fei, Y., Reno, B., Sobolev, N., Hauri, E., and Wysoczanski, R. (2003) OH⁻ in synthetic and natural coesite. *American Mineralogist*, 88, 1436-1445.
- Koga, K., Hauri, E., Hirschmann, M., and Bell, D. (2003) Hydrogen concentration analyses using SIMS and FTIR: comparison and calibration for nominally anhydrous minerals. *Geochemistry Geophysics Geosystems*, 4, 1019-1039.
- Kohlrausch, K.W.F. (1943) *Ramanspektren*. Akademische Verlagsgesellschaft Becher & Erler, Leipzig, 469 p.
- Kohlstedt, D.L. (2006) The role of water in high-temperature rock deformation. In H. Keppler and J.R. Smyth, Eds., *Water in nominally anhydrous minerals. Reviews in Mineralogy and Geochemistry*, 62, 377-396, Mineralogical Society of America, Chantilly.
- Kohn, S.C. (1996) Solubility of H₂O in nominally anhydrous mantle minerals using ¹H MAS NMR. *American Mineralogist*, 81, 1523-1526.
- Kronenberg, A.K. (1994) Hydrogen speciation and chemical weakening of quartz. In P.J. Heaney, C.T. Prewitt and G.V. Gibbs, Eds., *Silica: Physical behavior, geochemistry and materials applications, Reviews in Mineralogy*, 29, 123-176, Mineralogical Society of America, Washington, D.C.
- Kubicki, J.D., Sykes, D., and Rossman, G.R. (1993) Calculated Trends of OH Infrared Stretching Vibrations with Composition and Structure in Aluminosilicate Molecules. *Physics and Chemistry of Minerals*, 20, 425-432.
- Kurosawa, M., Yurimoto, H., Matsumoto, K., and Sueno, S. (1992) Hydrogen analysis of mantle olivine by secondary ion mass spectrometry. In Y. Xyono and M. H. Manghnani, Eds., *High-pressure research: application to earth and planetary sciences*, 283-287, Terra Sci., Tokyo.
- Lager, G.A., Armbruster, T., Rotella, F.J., and Rossman, G.R. (1989) OH substitution in garnets: X-ray and neutron diffraction, infrared, and geometric-modeling studies. *American Mineralogist*, 74, 840-851.
- Le Page, Y. and Donnay, G. (1976) Refinement of the crystal structure of low-quartz. *Acta Crystallographica*, B 32, 2456-2459.
- Li, W., Lu, R., Yang, H., Prewitt, C.T., and Fei, Y. (1997) Hydrogen in synthetic coesite crystals. *EOS*, 78, 736.
- Libowitzky, E. (1999) Correlation of O-H stretching frequencies and O-H...O hydrogen bond lengths in minerals. *Monatshefte für Chemie*, 130, 1047-1059.
- Libowitzky, E. and Rossman, G.R. (1997) An IR absorption calibration for water in minerals. *American Mineralogist*, 82, 1111-1115.
- Libowitzky, E. and Beran, A. (2004) IR spectroscopic characterisation of hydrous species in minerals. In A. Beran and E. Libowitzky, Eds., *Spectroscopic methods in mineralogy. EMU Notes in Mineralogy*, 6, 227-279, Eötvös University Press, Budapest, Hungary.
- Litasov, K.D., Kagi, H., Shatskiy, A., Ohtani, E., Lakshtanov, D.L., Bass, J.D., and Ito, E. (2007) High hydrogen solubility in Al-rich stishovite and water transport in the lower mantle. *Earth and Planetary Science Letters*, 262, 620-634.

- Mackwell, S.J., Kohlstedt, D.L., and Paterson, M.S. (1985) The role of water in the deformation of olivine single crystals. *Journal of Geophysical Research*, 90, 11319-11333.
- Maldener, J., Rauch, F., Gavranic, M., and Beran, A. (2001) OH absorption coefficients of rutile and cassiterite deduced from nuclear reaction analysis and FTIR spectroscopy. *Mineralogy and Petrology*, 71, 21-29.
- Maldener, J., Hösch, A., Langer, K., and Rauch, F. (2003) Hydrogen in some natural garnets studied by nuclear reaction analysis and vibrational spectroscopy. *Physics and Chemistry of Minerals*, 30, 337-344.
- Miller, G.H., Rossman, G.R., and Harlow, G.E. (1987) The natural occurrence of hydroxide in olivine. *Physics and Chemistry of Minerals*, 14, 461-472.
- Moritz, H. (1999) Messung des Konzentrationsfeldes verdunstender binärer Mikropartikel mittels linearer Raman-Spektroskopie. *Fortschrittsberichte*, 3, VDI-Verlag, Düsseldorf.
- Mosenfelder, J.L. (2000) Pressure dependence of hydroxyl solubility in coesite. *Physics and Chemistry of Minerals*, 27, 610-617.
- Panero, W., Benedetti, L., and Jeanloz, R. (2003) Transport of water into the lower mantle : role of stishovite. *Journal of Geophysical Research*, 108, 2039-2048.
- Paterson, M. S. (1982) The determination of hydroxyl by infrared absorption in quartz, silicate glasses and similar materials. *Bulletin de Minéralogie*, 105, 20-29.
- Pawley, A.R., McMillan, P.F., and Holloway, J.R. (1993) Hydrogen in Stishovite, with Implications for Mantle Water Content, *Science*, 261, 1024-1026.
- Reichart, P., Datzmann, G., Hauptner, A., Hertenberger, R., Wild, C., and Dollinger, G. (2004) Three-Dimensional Hydrogen Microscopy in Diamond. *Science*, 306, 1537-1540.
- Rhede, D. and Wiedenbeck, M. (2006) SIMS quantification of very low hydrogen contents. *Applied Surface Science*, 252, 7152-7154.
- Rossman, G.R. (1988) Vibrational spectroscopy of hydrous components. In F.C. Hawthorne, Ed., *Spectroscopic methods in mineralogy and geology*. *Reviews in Mineralogy*, 18, 193-206, Mineralogical Society of America, Washington, D.C.
- Rossman, G.R. (2006) Analytical methods for measuring water in nominally anhydrous minerals. In H. Keppler and J.R. Smyth, Eds., *Water in nominally anhydrous minerals*, 1-28, Mineralogical Society of America, Chantilly.
- Rossman, G.R. and Aines, R.D. (1991) The hydrous component in garnets: grossular-hydrogrossular. *American Mineralogist*, 76, 1153-1164.
- Rovetta, M.R., Blacic, J.D., Hervig, R.L., and Holloway, J.D. (1989) An experimental study of hydroxyl in quartz using infrared spectroscopy and ion microprobe techniques. *Journal of Geophysical Research*, 94, 5840-5850.
- Schabel, W. (2005) Inverse Mikro-Raman-Spektroskopie- Eine neue Messmethode zur Untersuchung lokaler Stofftransportvorgänge in dünnen Filmen, Folien und Membranen. *Chemie ingenieur Technik*, 77, 1915-1926.

- Severs, M.J., Azbej, T., Thomas, J.B., Mandeville, C.W., and Bodnar, R.J. (2007) Experimental determination of H₂O loss from melt inclusions during laboratory heating: evidence from raman spectroscopy. *Chemical Geology*, 358-371.
- Skoog, D. A. and Leary, J. J. (1992) *Principles of instrumental analysis*. Saunders college Publishing, 864 p.
- Smyth, J.R., Swope, R.J., and Pawley, A.R. (1995) H in rutile-type compounds: II. Crystal chemistry of Al substitution in H-bearing stishovite. *American Mineralogist*, 80, 454-456.
- Staats, P.A. and Kopp, O.C. (1974) Studies on the origin of the 3400 cm⁻¹ region infrared bands of synthetic and natural α -quartz. *Journal of Physics and Chemistry of Solids*, 35, 1029-1033.
- Sweeney, R.J., Prozesky, V.M., and Springhorn, K.A. (1997) Use of elastic recoil detection analysis (ERDA) microbeam technique for the quantitative determination of hydrogen in materials and hydrogen partitioning between olivine and melt at high pressures. *Geochimica and Cosmochimica Acta*, 61, 101-113.
- Thomas, R. (2000) Determination of water contents of granite melt inclusions by confocal laser Raman microprobe spectroscopy. *American Mineralogist*, 85, 868 – 872.
- Thomas, R. (2002) Determination of water contents in melt inclusions by laser Raman spectroscopy. Workshop-Short course on volcanic systems, geochemical and geophysical monitoring. In B. De Vivo and R.J. Bodnar, Eds., *Melt inclusions: Methods, Applications and Problems: Proceedings*, 211-216, Napoli, Italy.
- Thomas, R., Webster, J.D., and Heinrich, W. (2000) Melt inclusions in pegmatite quartz: complete miscibility between silicate melts and hydrous fluids at low pressure. *Contributions to Mineralogy and Petrology*, 139, 394-401.
- Thomas, R., Förster, H.-J., and Heinrich, W. (2003) The behaviour of boron in a peraluminous granite-pegmatite system and associated hydrothermal solutions: a melt and fluid inclusion study. *Contributions to Mineralogy and Petrology*, 144, 457-472.
- Thomas, R. and Davidson, P. (2006) Progress in the determination of water in glasses and melt inclusions with Raman spectroscopy: A short review. *Zeitschrift für geologische Wissenschaften*, Berlin, 34, 159-163.
- Thomas, R. and Davidson, P. (2007) Progress in the determination of water in glasses and melt inclusions with Raman spectroscopy: A short review. *Acta Petrologica Sinica*, 22, no. 12, 15-20.
- Thomas, R., Kamenetsky, V.S., and Davidson P. (2006) Laser Raman spectroscopic measurements of water in unexposed glass inclusions. *American Mineralogist*, 91, 467-470.
- Tröger, W.E. (1956) *Tabellen zur optischen Bestimmung der gesteinsbildenden Minerale*, Stuttgart, Schweizerbart'sche Verlagsbuchhandlung (Nägele u. Obermiller) Stuttgart... 147p.
- Wang, D., Mookherjee, M., Xu, Y., and Karato, S. (2006) The effect of hydrogen on the electrical conductivity in olivine. *Nature*, 443, 977-980.

Wegdén, M., Kristiansson, P., Skogby, H., Auzelyte, V., Elfman, M., Malmqvist, K.G., Nilsson, C., Pallon, J., and Shariff, A. (2005) Hydrogen depth profiling by p-p scattering in nominally anhydrous minerals. *Nuclear Instruments and Methods in Physics Research, Section B*, 231, 524-529.

Wiedenbeck, M., Rhede, D., Lieckefett, R., Witzki, H. (2004) Cryogenic SIMS and its applications in the earth sciences. *Applied Surface Science*, 231-232, 888-892.

Wirth, R. (2004) Focused Ion Beam (FIB): A novel technology for advanced application of micro- and nanoanalysis in geosciences and applied mineralogy. *European Journal of Mineralogy*, 16, 863-876.

Yurimoto, H., Kurosawa, M., and Sueno, S. (1989) Hydrogen analysis in quartz crystals and quartz glasses by secondary ion mass spectrometry. *Geochimica and cosmochimica Acta*, 53, 751-755.

Zajacz, Z., Halter, W., Malfait, W.J., Bachmann, O., Bodnar, R.J., Hirschmann, M.M., Mandeville, C.W., Morizet, Y., Muntener, O., Ulmer, P., and Webster, J.D. (2005) A composition-independent quantitative determination of the water content in silicate glasses and silicate melt inclusions by confocal Raman spectroscopy. *Contributions to Mineralogy and Petrology*, 150, 631-642.

Eidesstattliche Erklärung

Hiermit versichere ich, Sylvia-Monique Thomas, die vorliegende Arbeit ohne unzulässige Hilfe Dritter und ohne Benutzung anderer, als der angegebenen Hilfsmittel, angefertigt zu haben. Die aus fremden Quellen direkt oder indirekt übernommenen Gedanken sind als solche kenntlich gemacht.

.....

Ort, Datum

Unterschrift

Danksagung

Die Fertigstellung dieser Arbeit wäre ohne die Beteiligung vieler Personen undenkbar gewesen, denen ich im Folgenden meinen Dank entgegenbringen möchte.

An erster Stelle möchte ich mich ganz herzlich bei Monika Koch-Müller für ihre exzellente Betreuung, das stetige Interesse am Fortgang der vorliegenden Arbeit, für ihre Motivation und ihre grosse Geduld bedanken.

Für wertvolle Diskussionen und die immerwährende Unterstützung von Tagungs- und Fortbildungsvorhaben meinerseits bin ich Wilhelm Heinrich zu grossem Dank verpflichtet.

Meinem Vater danke ich für sein Vertrauen, mich allein an die "Maschine" zu lassen und für vielerlei Hilfe und Ratschläge.

Andreas Hösch und Wim van Westrenen stellten freundlicherweise Probematerial zur Verfügung.

Michael Wiedenbeck und vor allem Dieter Rhede sei für die Einführung in die Ionenstrahlmikroanalyse gedankt. Letzterem sowie Oona Appelt und Ilona Schäpan danke ich für die Durchführung von Mikrosonden- und Ionensondenmessungen.

Patrick Reichart, Günther Dollinger sowie dem gesamten Team in München danke ich für Einblicke in ihre Arbeit im Münchener Beschleunigerlabor und für die Messungen unserer Proben.

Richard Wirth danke ich für die Durchführung von TEM-Analysen und Karin Paech für manch Kristallpräparationshilfe. Matthias Gottschalk gebührt Dank für seine Unterstützung bei Röntgenverfeinerungen und die Lösung vielerlei computertechnischer Probleme. Christian Schmidt danke ich für hilfreiche Ratschläge, Matthias Kreplin für die Probenpräparation, Beate Hein für ihre immerwährende Unterstützung, und Paul Davidson für interessante Einblicke in die englische Fachsprache und hilfreiche Korrekturvorschläge. Für die experimentelle Unterstützung bin ich Bernd Wunder und Reiner Schulz zu grossem Dank verpflichtet. Gerhard Berger bin ich besonders dankbar, da er jederzeit für ausgefallene Probenpräparationswünsche meinerseits zur Verfügung stand und diese so schnell wie möglich umzusetzen versuchte.

Heike Steigert danke ich für ihre Freundschaft und das Durchführen von Röntgenanalysen. Volker Kahlenberg sei für Einkristallröntgenverfeinerungen, Michael Fechtelkord für NMR-Messungen und Ulrich Schade und Martin Schmidt für Hilfe während der Messzeiten am BESSY gedankt.

Grosser Dank gebührt der gesamten Sektion 4.1 und vor allem meinen wechselnden Zimmergenossen, die sich die Klinke in die Hand gegeben und mir den Alltag meist freudig gestaltet haben, angefangen von Michael Taran, Fabio Ferri, Kristin Gratz, Thorsten Herzog, Viktor Kvasnytyza, Stanislav Matsyuk, Natasha Khisina, Fabien Deschamps und Magali Rossi.

Mein besonderer Dank gilt meiner Familie und meinen Freunden, die mich fortwährend unterstützen.

Die Arbeit wurde finanziell, unter anderem durch eine grosszügige Reisekostenbeihilfe der Deutschen Mineralogischen Gesellschaft, unterstützt. Die Manuskripte konnten durch die Mitwirkung aller Koautoren und durch hilfreiche Gutachten der Editoren und Rezensenten des „American Mineralogist's“ verbessert werden.